Models of Wet Two Dimensional Foams

Friedrich Fionn Dunne

School of Physics

Trinity College Dublin

A thesis submitted for the degree of

Doctor of Philosophy

May 23, 2019

Declaration

I declare that this thesis has not been submitted as an exercise for a degree at this or any other university and it is entirely my own work. I agree to deposit this thesis in the University's open access institutional repository or allow the Library to do so on my behalf, subject to Irish Copyright Legislation and Trinity College Library conditions of use and acknowledgement.

Friedrich Dunne .....

Summary

In this thesis I used models and computer simulations to investigate the properties of two dimensional polydisperse foams from the dry limit of zero liquid fraction to the wet limit of 0.16 liquid fraction.

Initially I used the Plat software, which implements the standard model of two dimensional foams, to explore the full range of liquid fractions. As the software becomes increasingly less reliable towards the wet limit, we use over 500,000 simulations in order to obtain results in this regime. We found the variation of energy and coordination number with liquid fraction, and the internal distribution of contacts in the foams.

We then focus on the variation of the coordination number with liquid fraction close to the wet limit. In particular, we compare the results of the Plat simulation with those of the Soft Disk model, which is widely used in the study of foams. The Soft Disk model is widely used due to its simplicity, but it is approximate, and neglects deformations.

A stark difference between the two models is noted, with the Plat simulation exhibiting a linear variation of the coordination number with liquid fraction, and the Soft Disk model exhibiting a square root variation.

We investigate the link between the radial density function (and its analog, the distribution of separations), and the variation of the coordination number with liquid fraction in the wet limit. We find a marked difference

between the distributions of separations of the two models. This explains the difference in the variation of the coordination number. It appears to be due to the fact that the bubbles in the Plat simulation are deformable, while those in the Soft Disk model are not.

In order to explore the wet limit of two dimensional foams further, we develop a new model based on the theory of Morse and Witten. This model is defined for the wet limit, with deformable bubbles. It accurately predicts the response of a bubble of droplet to small deformations. We develop a framework and an algorithm for applying this theory to the case of modeling two dimensional foams.

The new simulation based on this model is tested against the Plat simulation. It produces comparable foams, with similar variations of the energy with liquid fraction. It also produces comparable contact changes with changes in liquid fraction. We propose an extension of this model to the case of three dimensional foams.

Finally, we demonstrate an additional application of the theory of Morse and Witten in three dimensions to the calculation of the surface tension of bubbles and drops. We derive a simple formula, taking two length measurements, without any free parameters, which predicts the surface tension of bubbles and drops to a reasonable degree of accuracy (within 2%).

Acknowledgements

The most frequent reader of the start of a thesis is a new PhD student, so I want to begin mine with few words of encouragement to those setting off on their journey of discovery. I always knew that I wanted to study science, and to me, Physics gave the most fundamental explanations of how stuff works. However, I never intended on doing a PhD, in school I always thought that that was solely for the best of the best. However, when I heard that Professor Stefan Hutzler had funding available for a PhD, I took a chance and went for it – and here I am. If you have an idea, or see an opportunity, go for it! You never know what might happen.

I'd like to thank Stefan for taking a chance on me, and allowing me to turn his experimental PhD position into a computational one. None of this would have been possible without his enthusiasm, his tireless support, his hard work and dedication, and his passion for the field of foams. I'd like to thank Professor Emeritus Denis Weaire for the clarity of his insight (both mathematical and physical), his font of research tangents that keep a project moving, and his constant demands for clearer explanations. I'd like to thank Professor Matthias Möbius for discussions of scaling laws, and the knowledge of when it's appropriate to use a log scale.

For making this the wonderful experience that it was I'd like to thank the office for providing a truly unique working environment: Ben, Jens, Steve,

Rob, Gav, and Dave, you all know the roles you played in that! Ben in particular, the office will be much quieter without you here. Jens, thank you for putting up with me getting you to double check my work all of the time. Both of you, thanks for making lunch so much more fun.

To my parents, thank you for encouraging me, supporting me, and simply for being proud of me. I love you both.

Becky, thank you for being patient with me through this. Without your kind and loving dedication this would not have turned out half as well as it did. (In particular, this thesis would be a lot poorer in commas!) Your encouragement and your belief in me mean the world to me. Simply put, I love you.

Finally, the aforementioned funding that supported this work is a research grant from Science Foundation Ireland (SFI) under grant number 13/IA/1926.

List of Publications

1. F. F. Dunne et al. "Statistics and topological changes in 2D foam from the dry to the wet limit". In: *Philosophical Magazine* 97.21 (2017), pp. 1768–1781

2. J. Winkelmann et al. "2D foams above the jamming transition: Deformation matters". In: *Colloids and Surfaces A: Physicochemical and Engineering Aspects* 534 (2017). A Collection of Papers Presented at the 11th Eufoam Conference, Dublin, Ireland, 3-6 July, 2016, pp. 52–57. ISSN: 0927-7757

3. Stefan Hutzler et al. "A simple formula for the estimation of surface tension from two length measurements for a sessile or pendant drop". In: *Philosophical Magazine Letters* 98.1 (2018), pp. 9–16

4. B Haffner et al. "Ageing of fibre-laden aqueous foams". In: *Cellulose* 24.1 (2017), pp. 231–239

5. F. Dunne et al. "Implementation of Morse–Witten theory for a polydisperse wet 2D foam simulation". In: *Submitted to Philosophical Magazine* (2018)

Contents

List of Tables

List of Figures

Chapter 1

What is a Foam?

Most generally, a foam is considered to be a two-phase system of gas bubbles dispersed within a liquid. Foams are a part of everyday life, sometimes beneficial, other times a nuisance, but mostly we don't give foam a second thought. Whether it's a squirt of shaving foam (which doesn't flow off skin under gravity) in the morning, the white head creating the creamy texture of a pint, or a pot of pasta boiling over, foam is everywhere. Industrial processes which make use of foams include foam fractionation for water treatment and froth flotation for mineral separation in mining [6]. Also studied in conjunction with foams are other two-phase systems such as *emulsions*, which consist of one immiscible liquid dispersed within another. Foams and emulsions have very similar physical properties. In this thesis reference will only be made to foams, without loss of generality the simulations and results can also be applied to emulsions.

The simplest way to make bubbles is to trap gas (often air) in a liquid (often water). Turbulence and flow instabilities can entrain gas bubbles in poured or flowing liquids; for example when you fill a water bottle from a fast flowing tap. Usually these bubbles are unstable and the water quickly

(a) Shaving foam **(b)** A creamy pint

Figure 1.1: Everyday examples of foam

drains out of the films, causing the bubbles to burst. Bubbles collect and build up into a foam when there are additives, such as soap or proteins, in the liquid that can stabilise the films and prolong the lifetime of the bubbles. *Surfactants* are a class of molecules to which soaps belong. These are undecided molecules which have parts that energetically favour being in water and parts that do not. Due to this, they place themselves at interfaces, where both their parts can be satisfied. There they lower the surface tension and, thanks to gradients in their concentration, they can stabilise the thin films that separate the air pockets, preventing rupture. How surfactants act and how their properties influence those of the foam is a subject of ongoing research [7, 8], but outside the scope of this thesis.

1.1 What are Two Dimensional Foams?

Up to this point in this thesis, *Models of Wet Two Dimensional Foams*, I have referred to three dimensional foams. A two dimensional foam is a single flat layer of bubbles that, in an idealised case, has zero height. In practice it can be realised in quasi-two dimensional experiments as a single layer of

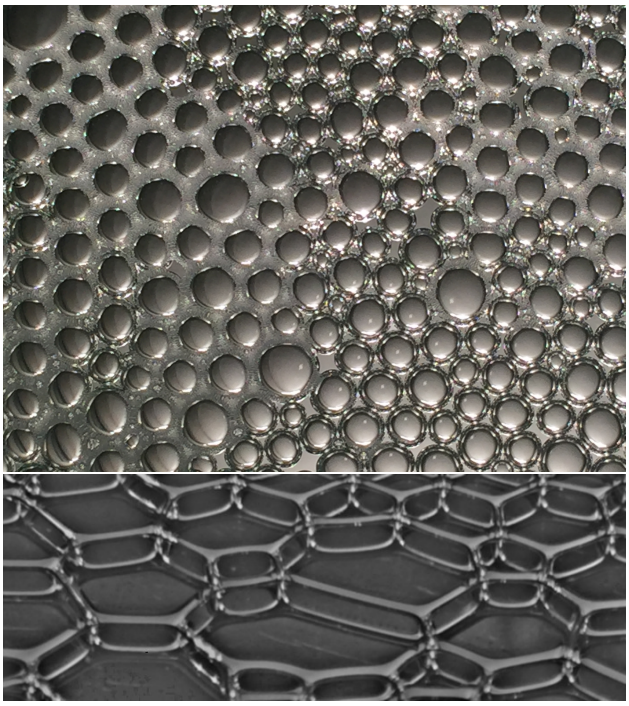

Figure 1.2: Top: A close up of a single layer of bubbles (diameter $\simeq 0.5\,\mathrm{mm}$) floating on a liquid pool (an example of a Bragg raft). Image credit: Steven Burke, TCD Foams group. Bottom: A close up of a single layer of bubbles (diameter $\simeq 1\,\mathrm{cm}$) sandwiched between two glass plates separated by $3\,\mathrm{mm}$ (an example of a Hele-Shaw cell). Image credit: Benjamin Haffner, TCD Foams group

regular three dimensional bubbles in one of three configurations: between two parallel (transparent) plates (also called a Hele−Shaw cell [9]), floating on top of a liquid reservoir (also called a Bragg raft [10]), or floating on a liquid reservoir with a covering transparent plate pressed down on top. They are called *quasi-two dimensional* because there is a three dimensional liquid network surrounding the bubbles in the monolayers [11].

These experimental systems are often used in the lab to probe the behaviour of three dimensional foams because it is possible to observe every

bubble in two dimensions. For example, a two dimensional foam may be sheared to measure its flow behaviour while being imaged to track the motion of individual bubbles [12]. This is very difficult to do in three dimensions, where simple imaging techniques fail due to the scattering of light as the light passes through multiple interfaces. Therefore, in three dimensions, expensive and cumbersome x-ray equipment is needed in order to see into the centre of a foam.

Another area that is much more accessible in two dimensions is simulation. A simulation in two dimensions is computationally quicker than in three dimensions because there are fewer interactions to calculate. This can be understood from the fact that, in a simple three dimensional cubic lattice there are 26 ($3^{D=3} - 1$) next nearest neighbours, compared to only eight ($3^{D=2}-1$) in two dimensions. This is compounded by the fact that, for a three dimensional simulation to be comparable with a two dimensional simulation in terms of nearest neighbours, it has to be at least three times larger. For instance, if a three dimensional simulation consists of N bubbles, it can be considered to be $N/26$ nearest neighbours 'across'. A two dimensional simulation that is the same number of nearest neighbours across consists of $N(8/26)$ bubbles. The speed of modern computers and access to high performance computing resources reduces the significance of these differences when running simulations. However, development of the simulation framework is much easier in two dimensions as it reduces the length of the feedback cycle, a significant motivating factor behind the choice in this work to create a two dimensional Morse−Witten simulation in Chapter 3, rather than a three dimensional one.

1.2 Properties of Foams

1.2.1 Liquid Fraction

A simple property of a foam that can be considered is its global *liquid fraction*, ϕ [13]. This is the ratio of the total liquid volume to the total foam volume. Foams with a liquid fraction below ~ 0.10 are considered *dry* foams, with polyhedrally shaped bubbles (see Figure 1.3 (top)). Foams with higher liquid fractions are considered *wet* foams, with roughly spherically shaped bubbles (see Figure 1.3(bottom)). The distinction between wet and dry foams is they have both different geometries and they both exhibit different behaviours due to the different overall bubble shapes (see Section 1.2.5 for examples to do with flow behaviour).

The Dry Limit

Very dry foams (with a liquid fraction below 0.01) can be described as a collection of thin films of negligible thickness around a cellular structure of gas bubbles in (roughly) polyhedral shapes, though the interfaces are in general curved, as described by the Young–Laplace law (see Section 1.3.2.

The Wet Limit

There is a particular value of liquid fraction, ϕ_c, know as the *critical liquid fraction*. Beyond this point a foam behaves like a liquid with bubbles in it as the bubbles are no longer in contact with one another. It is also called the wet limit because it is the wettest a foam can be while still retaining foam like properties. At the wet limit the bubbles, which are all perfect spheres, are just in contact with each other without being deformed. Also known as the *jamming transition*, this point has been of great interest in recent years

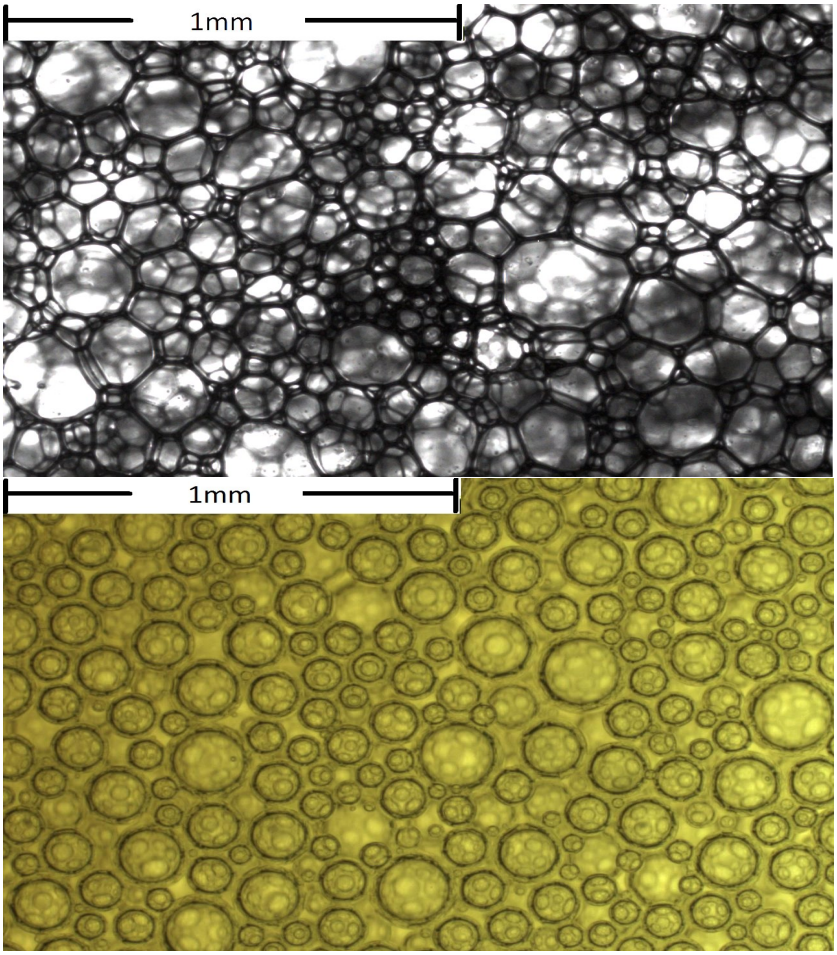

Figure 1.3: Close-up examples of a dry foam ($\phi < 1 \sim 2\%$) (top), and a wet foam ($\phi \simeq 20 \sim 25\%$) (bottom). Bubbles in the dry foam are mostly polyhedral, while in the wet foam they look near spherical. Image credit: Gavin Ryan, TCD Foams group

since, close to this value of ϕ, other properties of foams exhibit interesting scaling laws [14]. Some of these will be discussed in Sections 1.2.3 and 1.2.4.

At ϕ_c in three dimensions, a foam closely resembles a granular packing of hard spheres, while in two dimensions, it is quite similar to a packing of hard disks. ϕ_c for a polydisperse foam (with a range of bubble sizes, see Section 1.2.2) in three dimensions is 0.36, while in two dimensions it is 0.16. This is due to the fact that disks fill a two dimensional plane more efficiently than spheres fill a three dimensional space.

1.2.2 Bubble Sizes

When studying foams under gravity, a natural length scale arises from considering the competition between gravity pulling the liquid out of the films and surface tension pulling the liquid back into the films. This is called the *capillary length*

$$\lambda_c = \sqrt{\frac{\gamma}{\rho g}}, \tag{1.1}$$

where γ is the surface tension, ρ is the liquid density, and g the acceleration due to gravity. This length tells how far water will be drawn up into the foam by capillary action. Typical water and soap solutions have a density of $1000\,\mathrm{kg\,m^{-3}}$ and a surface tension of $25\,\mathrm{mN\,m^{-1}}$ giving $\lambda_c = 1.6\,\mathrm{mm}$. This can be compared to the typical bubble sizes in a foam.

One possible measure of the *size* of a bubble is given by its equivalent sphere radius R. That is, the radius of a sphere with the same volume as the bubble. These vary widely depending on the foam and can range from less than a millimetre up to a metre [15], so can be smaller or larger than the capillary length. Film thicknesses may be in the range of 5 nm to 10 µm, much smaller than the capillary length.

If all the bubbles in a foam have the same size it is called *monodisperse*.

This generally does not occur in nature where random processes are usually at play, but the simplicity it affords makes it useful in the lab. Additionally, using monodisperse liquid foams as a precursor to solid foam materials gives a way to finely control the structural properties of these materials [16]. The bubbles in a monodisperse foam can tend to form an ordered, crystalline structure. When the bubbles come in a range of sizes the foam is termed *polydisperse*. The polydispersity is measured as the standard deviation of the distribution of radii divided by the average bubble radius, defined in terms of the mean ($\langle R \rangle$) and squared mean ($\langle R^2 \rangle$) of the distribution of R as

$$\sigma_R = \sqrt{\frac{\langle R^2 \rangle}{\langle R \rangle^2} - 1}. \tag{1.2}$$

For a perfectly monodisperse foam $\sigma_R = 0$, but for practical purposes a foam is considered to be monodisperse if $\sigma_R < 0.05$. In contrast to monodisperse foams, a polydisperse foam forms disorded, random structures. Polydisperse two dimensional foams are found to crystallise, at least partially, for $\sigma_R < 0.1$, and form truly random systems when $\sigma_R > 0.1$ [17]. In the intermediate range of $0.05 < \sigma_R < 0.1$, foams tend to form partially crystalline systems, with localised regions or order and disorder. Another way to create disordered, random structures is to mix two monodisperse foams with different bubble sizes. The result is called a *bidisperse* foam. In bidisperse foams the critical size ratio of large bubbles radius to small bubble radius need to form disordered structures is 1.14 [18]. The order and disorder, i.e. the respective presence or absence of long range correlations in the bubble positions, in a foam can greatly influence its properties. For example, in two dimensions an ordered monodisperse foam has a $\phi_c = 1 - \pi/(2\sqrt{3}) \simeq 0.09$, compared with the 0.16 of a random polydisperse foam.

1.2.3 Energy

In the standard quasi-static models of foams (see Section 1.4.1 for two dimensional examples), the gas in the bubbles is treated as incompressible; therefore, the surface energy is the only relevant energy for describing the two dimensional foams. The surface energy of a foam is $E = \gamma A$, where A is the total surface area. In the case of two dimensional foams, the equivalent of the surface energy is then a line energy, proportional to the total perimeter of all the bubbles.

A foam will adopt a configuration which minimises this energy. Therefore, the films in a foam fall into a category know as *minimal surfaces*, a local minimum. To globally minimise their energy, the films would collapse into a single disk of liquid. This does not happen if the local minimum is stable enough (i.e. the films don't burst). A corollary of this is that a bubble that is free to move will always form a sphere in three dimensions, or a circular disk in two dimensions. Note that, in the models described here it will always be assumed that the films will not burst.

At all values of liquid fraction below the critical liquid fraction ($\phi < \phi_c$), the bubbles are deformed from spherical, increasing their surface energy. Therefore, a dimensionless *excess energy* can be defined as

$$\varepsilon(\phi) = \frac{E(\phi) - E_c}{E_c} = \frac{E(\phi)}{E_c} - 1, \tag{1.3}$$

where $E_c = E(\phi_c)$, the energy of the foam in the wet limit.

1.2.4 Coordination Number

The structure of a foam can be studied by looking at the average number of contacts per bubble. However, due to the formation of structural "cages" of bubbles supporting one another, some bubbles can "rattle" around in an

otherwise stable configuration. These, therefore, do not contribute to the mechanical stability of the foam, and thus do not contribute to many of the physical properties of the foam. In two dimensions these loose bubbles, known as *rattlers*, can be identified by the fact that they have less than three contacts each (less than four each in three dimensions) and, thus, cannot be mechanically stable. The *coordination number*, Z, of a foam is the average number of contacts per bubble, after these rattlers have been discounted. This does not affect the coordination number significantly as the rattlers make up at most 2% of the bubbles (see Chapter 2, Figure 2.6 for more details). For a polydisperse, disordered foam, this is a function of liquid fraction ϕ. Generally, in two dimensions, the distribution of contact numbers appears to follow a Gaussian distribution with a fixed width, regardless of the model used to simulate the foam (see Section 2.2.4).

The value of Z in the dry limit can be shown to be six via Euler's theorem which relates the number of faces, edges, and vertices of a cellular structure to a topological invariant (see [15] for a detailed explanation).

At the wet limit, ϕ_c, the limiting value of the coordination number, $Z(\phi_c) = Z_c$, can be found by looking at degrees of freedom. For each dimension in a given model or experiment, a bubble has one degree of freedom. In the wet limit there are just enough constraints on the foam that each bubble is held in place. Each contact provides one constraint to two bubbles. This leaves each bubble with, on average, $Z/2$ constraints. Equating degrees of freedom with constraints, we get $3 = Z_c/2$ in three dimensions and $2 = Z_c/2$ in two dimensions. Therefore, on average in an system of infinite size, $Z_c = 6$ in three dimensions, and $Z_c = 4$ in two dimensions [19, 20, 14].

By looking at a finite system we generally lose a small number of degrees of freedom. For example, in a two dimensional system with periodic boundary

conditions and N bubbles, the system does not change if we move every bubble by the same amount (it is invariant under translation). This means that one bubble can be fixed (equivalent to fixing a point of view), leaving $2(N-1)$ degrees of freedom. Equating this to the $NZ_c/2$ constraints we get $Z_c = 4(1-1/N)$. As we increase N we can see that the correction for finite size vanishes.

Various experiments for quasi-two dimensional foams [21] and two dimensional elastic disks [22], and simulations with the more approximate Soft Disk model [23] have been in agreement in finding the limiting form for the average coordination number Z. In particular,

$$Z - Z_c \propto (\phi_c - \phi)^{1/2}, \tag{1.4}$$

where $Z_c = Z(\phi_c)$.

The discovery of the square root scaling for $Z(\phi)$ appears to date back to the work of Durian using the so-called Soft Disk model (see Section 1.4.2 for details). Durian developed this model primarily to investigate the rheological properties of foams, of which it indeed provides a good overall description [24, 25, 26]. Two dimensional bubbles are approximated as disks, subject to repulsive forces when they overlap.

The same square-root scaling for $Z(\phi)$ was also found in computer simulations of packings of three dimensional soft spheres [27], a system which has since been called the Ising model for jamming [14].

We will show in Section 2.4.1 that Relation (1.4) is not always the case. In particular, for simulations built on an exact model for two dimensional foams (see Section 1.4.1), the relationship is linear.

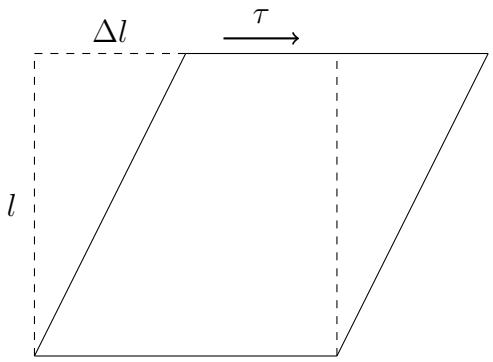

Figure 1.4: Schematic representation of the response of an elastic solid to an applied shear stress, τ. The dashed lines represent the undeformed solid, the solid sloped lines represent the solid's response to the strain τ. Δl measures the deformation of the solid, which has a height l, thus the resulting strain is $\Delta l/l$.

1.2.5 Rheological Properties

When an elastic solid is subjected to a small shear stress, τ, as depicted in Figure 1.4, the relative deformation, or strain, $\Delta l/l$ is linearly related to the applied stress by the *shear modulus*, where Δl is the change in length and l is the width. Foams behave like *elastic solids* when a small stress is applied. When the stress on a foam is increased it will reach a critical point after which the foam will not deform like an elastic solid, but it will flow like a liquid. The amount of stress required to get a foam to start flowing (i.e. in continuous motion with bubbles constantly rearranging) is called the *yield stress*, τ_y.

A liquid deforms continuously under an applied stress. The strain rate, $\dot{\gamma}$, is linearly related to the applied stress by the resistance to flow, *viscosity*. In a flowing foam it is this same viscosity that provides resistance to flow. However, this friction is only experienced in the films between bubbles in contact. Since the film is typically at least 10^4 times smaller than the bubbles

in a foam, the resistance to flow is amplified by this same factor. This means that the effective viscosity of a foam is typically at least 10^4 times greater than that of the liquid in the foam.

Additionally, the relationship between stress and strain rate is no longer linear. Firstly, the strain rate is zero for any stress below the yield stress. Secondly, the relationship between stress and strain rate in a foam is in fact

$$\tau = \tau_y + \kappa\dot{\gamma}^n, \tag{1.5}$$

a power law know as the Herschel−Bulkley [28] law. Here, κ can no longer be called a viscosity as its dimensions must change to compensate for the effect the power n has on the dimensions of $\dot{\gamma}$. Instead it is referred to as the *consistency*, but it plays the role of an effective viscosity. As our models are quasi-static rather than dynamic, the details of rheology, the study of flow, will not form part them. However, we will still be able to predict some properties that can be related to the rheology of foams.

Wet foams, with higher liquid content, flow much more easily than dry foams. This is because as ϕ is increased towards ϕ_c, the area of the films between contacting bubbles decreases. This makes it easier for bubbles to rearrange, and as a result, both the shear modulus and the yield stress of foams decrease as the liquid content of the foam is increased. Beyond ϕ_c, the foam loses rigidity and the yield stress and shear modulus both go to zero.

The shear modulus going to zero was first confirmed experimentally by Princen and Kiss [29]. It was also tentatively identified in the early two dimensional Plat simulation (see Section 2.1.1 for details) of Bolton and Weaire [30, 31, 32, 33], as well as in the two dimensional Soft Disk model of Durian [34]. The yield stress also goes to zero in the wet limit. Again, Princen may be credited with this finding [35]. This trend was reproduced in the early two dimensional Plat simulations of Bolton and Weaire [33], and

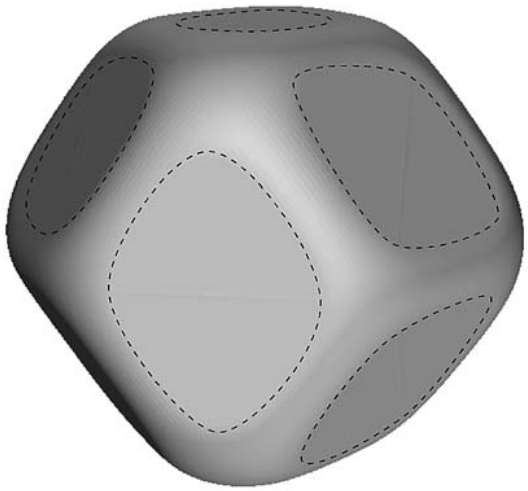

Figure 1.5: An example of a Surface Evolver calculation of a three dimensional bubble with 12 symmetric contacts in an ordered, monodisperse foam by Hutzler *et al.* [38]. The dashed lines on the faces indicate the boundaries of the contact faces when this single bubble is repeated to represent a crystalline foam.

Hutzler *et al.* [36].

1.3 Describing Foams

1.3.1 Minimal Energy Surfaces

We can completely describe a foam if we can fully describe the position and shape of all of its films. Finding the film configuration that minimises the surface energy can, in general, only be done numerically. For this task, a software called Surface Evolver is commonly used [37]. It is a program which, when given an initial surface, will minimise its energy, subject to constraints.

There are many situations where the minimal energy condition is sufficient for calculating the confiduration of a foam, particularly if there is a

high degree of symmetry involved (see for example Figure 1.5). To aid our understanding of foams, additional rules about the shapes and interactions of films in foams can be derived from this condition.

1.3.2 Young–Laplace Law in Three Dimensions

Each gas-liquid interface has a pressure difference, Δp, across it, and so its curvature is given by the Young−Laplace law

$$\Delta p = \frac{2\gamma}{r} \tag{1.6}$$

where γ is the surface tension and r the mean local radius of curvature. This mean local curvature is related to the two principle curvatures of the surface, r_1 and r_2, by

$$\frac{1}{r} = \frac{1}{2}\left(\frac{1}{r_1} + \frac{1}{r_2}\right). \tag{1.7}$$

A single gas bubble in a liquid is a sphere, and so only has one principle curvature everywhere ($r = r_1 = r_2$). A bubble in air, as a child would blow with a bubble wand, has two liquid−gas interfaces. This effectively doubles the surface tension and the radius. This is because a higher surface tension makes deforming the interface more costly in terms of energy.

In an ordered foam, with equal sized bubbles, there are sufficient symmetries to enable one to solve for the curvatures completely [39]. In a disordered foam, however, Equation (1.6) must be applied to the individual faces of contacts between bubbles in turn. This is because, in general, they do not have the same symmetries and Δp is different at each face. Finding a solution for the curvature of each face of a bubble is no easy task. Below are some additional rules that foams obey which aid us in understanding their behaviour. These give additional constraints that we can use to simplify the problem of describing the general structure of films in foams.

1.3.3 Plateau's Laws for Dry Foam in Three Dimensions

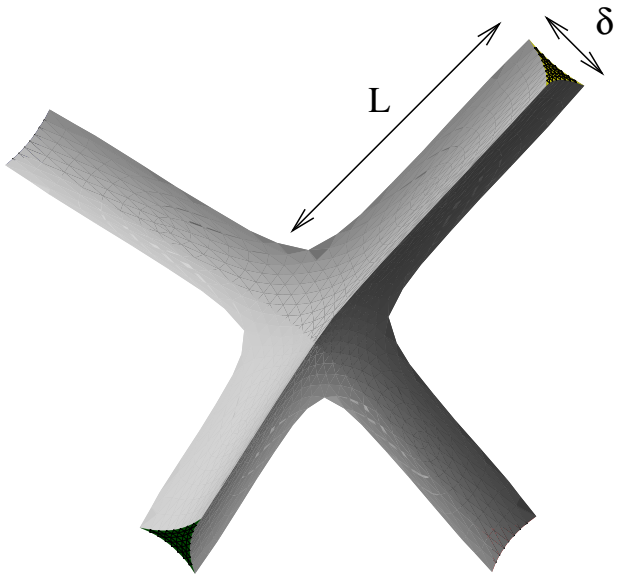

Figure 1.6: Figure reproduced from [40]. A Surface Evolver simulation of a junction between four Plateau borders. This shape is difficult to describe analytically, but the result of numerical calculations such as this one provide a lot of information, such as how the width of the plateau border, δ, changes with proximity to the node, L.

If we consider films with negligible thickness (i.e. in the dry limit) then the meeting of these films is governed by Plateau's laws. The first of these states that the meeting of films occurs in threes and, being symmetric, they meet at 120°. The lines along which the films meet are called *Plateau borders*. When the liquid content of a foam is increased, these thicken into channels. The second rule governs the meeting of these Plateau borders and states that they meet in groups of four, and at equal angles. These meeting points are called *nodes*. When the liquid content of a foam increases, they can take on complex shapes and can be difficult to describe analytically [15]. Figure 1.6

shows a Surface Evolver calculation of the shape of a node. These laws are a consequence of the energy minimisation of the films.

1.3.4 Young–Laplace Law in Two Dimensions

As discussed in Section 1.1, two dimensional foams are often used to study complicated phenomena in real foams in a simplified setting. In this case, the gas-liquid interfaces are lines instead of surfaces. Therefore, there is only one principal radius of curvature, r, per interface, and the Young−Laplace law simplifies to

$$\Delta p = \frac{\gamma}{r}. \tag{1.8}$$

This has the implication that each segment of a bubble's boundary, be it a bubble−bubble or bubble−liquid interface, is described by an arc of a circle of radius given by Equation (1.8). At contacts with neighbouring bubbles there are two liquid−gas interfaces, one for each bubble. To account for this we use twice the surface tension in determining the curvature of these edges, compared with the regular bubble−liquid interfaces.

1.3.5 Plateau's Laws in Two Dimensions

Plateau's first law for dry foam remains, with the substitution of lines for films at the interfaces between bubbles. Films meet symmetrically in threes at angles of 120°. In dry two dimensional foams the Plateau borders where they meet are points rather than the channels that are seen in three dimensions (see Figure 1.7(a)). Therefore, there are no nodes in two dimensions. Additionally, in two dimensions, a small amount of liquid may be added at each dry Plateau border, up to a liquid fraction of ~ 0.05 before this rule breaks down (see Figure 1.7(b)). This is known as *decorating* a dry foam

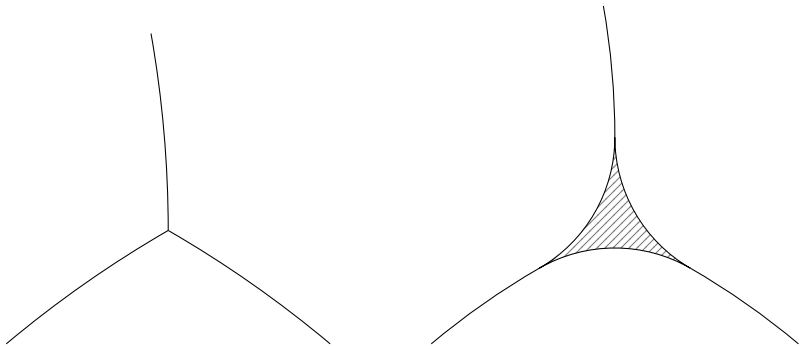

(a) Dry Plateau border **(b)** Wet Plateau border

Figure 1.7: Illustration of the decoration of a dry Plateau border with some liquid in two dimensions. The wet Plateau border (b) is still a threefold meeting of edges and at each corner of the Plateau border the lines meet smoothly.

[30]. When the amount of liquid exceeds 0.05, the condition of meeting in threes is relaxed and Plateau borders begin to meet and join together. This will be shown in more detail in Section 2.2.5.

1.3.6 Topological Changes in Two Dimensions

When two Plateau borders, with three sides each, come into contact they merge into a four-sided Plateau border. For very dry foams, $\phi < 0.05$, a four-sided Plateau border is unstable and will revert back to two three-sided Plateau borders, but with the opposite orientation to the original pair, see Figure 1.8. This is termed a topological transition of the first kind by Bolton and Weaire [31], or a T1 for short. Since the total number of contacts does not change in a T1, the average coordination number cannot change through these events. Only once the four-sided (and larger) Plateau borders become stable can bubbles lose contacts and the coordination number decrease.

As the liquid fraction of the foam is increased above 0.05, we begin to see contact losses without a corresponding contact gain to complete the T1.

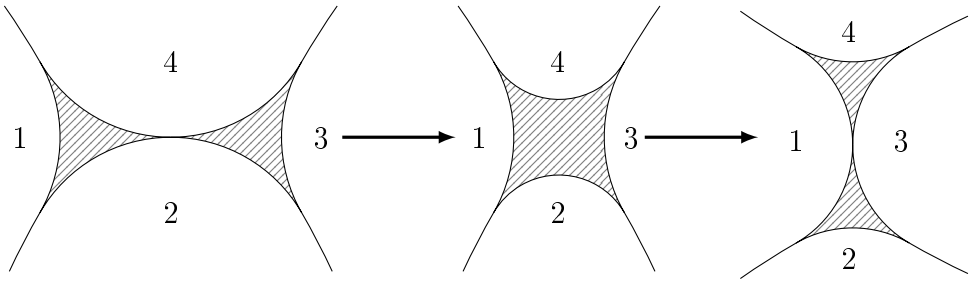

Figure 1.8: Illustration of the components of a T1 event. Two three-sided Plateau borders merge to form an unstable four-sided Plateau border. This in turn decays into two three-sided Plateau borders, but with the orientation perpendicular to the original pair.

Therefore, we study simply the individual contact changes in the foam, rather than T1 events. To study just the contact changes we can make use of an idea from graph theory called the *adjacency matrix*. This is a square $N \times N$ matrix of zeros and ones whose elements ij equal to one if bubble i is in contact with bubble j, and zero otherwise. Simply by subtracting successive matrices, changes in the contact network show up as non zero elements in the difference. I have used this approach to study rearrangements in two dimensional foam simulations in Section 2.3.

1.4 Modelling Two Dimensional Foams

1.4.1 Standard Model of Two Dimensional Foams

Plateau's laws can be combined with the Young−Laplace law to build a model of a two dimensional foam. In this model, the boundary of each bubble is broken down into a collection of interface segments, each of which is a circular arc, see Figure 1.9. The gas in the bubbles is assumed to be incompressible, see Section 1.2.3. Thus, the pressure in each bubble is proportional to the

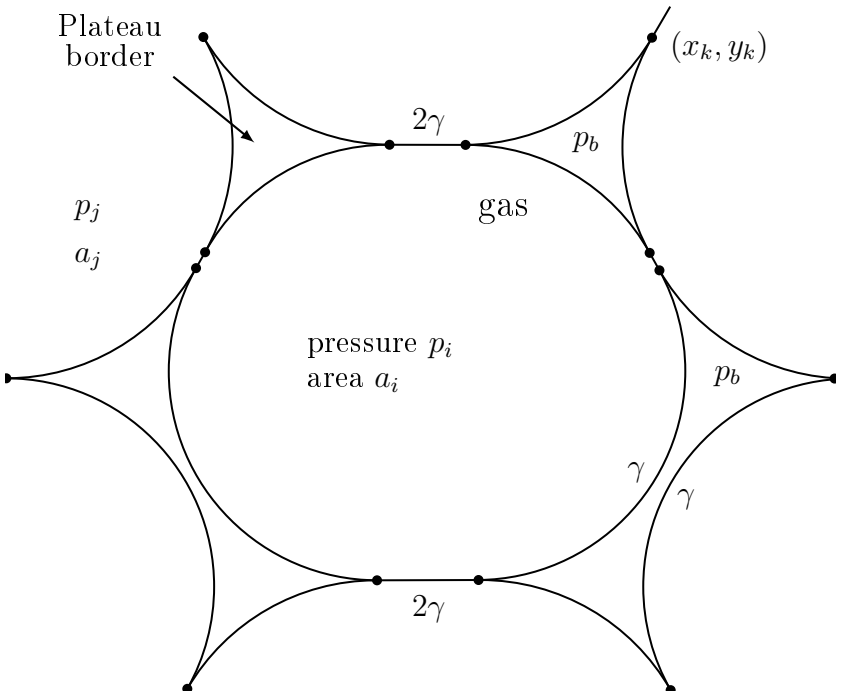

Figure 1.9: Schematic of a single bubble in the standard model of two a dimensional foam. (x_k, y_k) is the position of vertex k, γ the interfacial surface tension, p_b the Plateau border pressure, p_i the gas pressure of bubble i, and a_i the area of bubble i.

area. The films between contacting bubbles are assumed to have negligible thickness. The curvature of each film is determined by Equation (1.8).

When the foam is dry, these films meet in threes at point-like Plateau borders, and their tangents at the meeting point each have an angle of 120° between them. When the liquid fraction is increased, these Plateau borders swell into curved triangles. The pressure inside each Plateau border is equal due to hydrostatics, because, in the physical systems that the model represents such as a Hele−Shaw cell, each Plateau border is connected via liquid in the films. The curvature of the sides of the Plateau borders is also determined by Equation (1.8), except that there is only one liquid−gas

interface so the surface tension used is half that of the films.

The corners of the Plateau borders are called *vertices*. At each vertex, two liquid−gas interfaces meet one film. They must all meet smoothly, i.e. their tangents much be equal at the vertex. This is the extension of Plateau's law into wet two dimensional foams.

These conditions are sufficient to fully describe any two dimensional foam. One implementation of this model is a software program called Plat, introduced in the early 1990s by Bolton and Weaire [30, 31, 32, 33]. It has been used extensively in this thesis and will be covered in further detail in Section 2.1.1. It is a quasi-static model producing two dimensional foam structures which satisfy Plateau's laws. The Plat simulation is very reliable for dry foams and moderately wet foams, but unfortunately less so for very wet foams ($\phi \gtrsim 0.12$), see Section 5.1.2 for detailed statistics. For systems with over 20 bubbles it can fail to find an equilibrium configuration at liquid fractions beyond 0.1, with the probability of failure increasing with both system size and liquid fraction.

The model can also be implemented for dry foams using Surface Evolver in the manner of Cox and Davies *et al.* [41]. This is a quasi-static implementation that they use to study the rheology of objects falling under gravity through dry foam [42, 43], and dry foam flowing through channels with various constrictions [44]. Simulating wet two dimensional foams with Surface Evolver is also possible. However, due to numerical constrains, it requires the use of a finite contact angle at the meeting point of liquid and gas which has significant repercussions [45]. With a finite contact angle, when the liquid fraction of the foams is increased, the liquid does not distribute evenly throughout the foam. In fact, the foam splits into two phases: a liquid pool and a moderately wet foam (depending on the contact angle). While

this is quite similar to real foams, it does not represent the idealised case of zero contact angle which is used to study foams theoretically.

1.4.2 Soft Disk/Sphere Model

In the wet limit of two dimensional foams, the bubbles are all circular. In fact, foams in the wet limit can be described as packings of hard disks, as discussed in Section 1.2.1. This led to the development of the "Soft Disk" model in which bubbles are approximated as circles. Away from the wet limit the disks are allowed to overlap. When the disks overlap they repel via a simple potential, often approximated as harmonic [34]. This has been chosen mainly for computational simplicity. However, Surface Evolver simulations have shown that, while the energy is harmonic in two dimensions, the bubble-bubble interactions are not pairwise-additive [46]. That is, the model of interaction that lies at the heart of the Soft Disk model does not represent realistic bubble-bubble interactions. This will be addressed in Chapter 3.

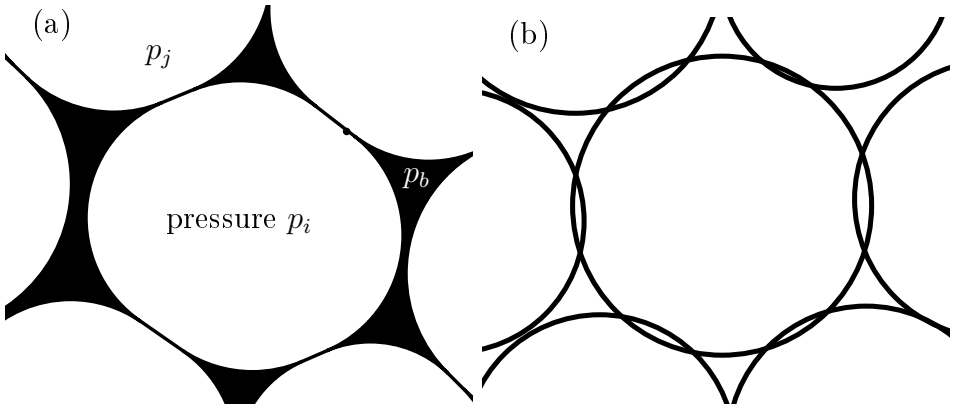

Figure 1.10: Comparison between Plat and the Soft Disk model for $\phi = 0.90$. The bubbles in (a) Plat are deformed even close to the wet limit, as seen in the example. In contrast (b) shows an example of overlaps in a Soft Disk simulation at the same value for ϕ.

Additionally, the Soft Disk model does not conserve gas area, while the Plat implementation of the standard model of two dimensional foam does. This is immediately apparent when considering visual representations of Plat (Figure 1.10(a)) and the Soft Disk model (Figure 1.10(b)).

An associated difficulty is the definition of liquid fraction in the Soft Disk model. The liquid fraction in the standard two dimensional model is readily defined as the fraction of the whole simulation geometry not filled with bubbles. With the overlapping disks in the Soft Disk model it becomes quite difficult to calculate the area of each overlap when more than two spheres partially overlap the same area. Computationally this would also defeat the purpose of the simplicity of the model. Instead, in the spirit of a first order approximation, the double counting of the overlap areas is simply ignored, and the liquid area is calculated as the whole simulation area minus the sum of the disk areas. For more compressed (i.e. dry) cases this can lead to negative liquid fractions, a physical impossibility. Of course, the model is defined in the wet limit and so should not be expected to produce sensible results for dry foams.

In three dimensions an analogous model is used called the "Soft Sphere" model. It treats the bubbles as spheres that are allowed to overlap. When they overlap, they repel with a harmonic potential. In both the two and three dimensional cases, part of the success of the model can be attributed to the fact that the harmonic potential is arbitrary and may be tuned to model one specific experiment.

While this has been successful in reproducing the Herschel–Bulkley type rheological behaviour that is associated with emulsions and foams, it does not reproduce all of the behaviours of foams.

In fact, the interaction of two bubbles that are just in contact (analogous

to being close to the wet limit) is intrinsically anharmonic [47]. This anharmonic nature was identified by Morse and Witten [48] and has resulted in a model which will be outlined in Section 1.4.3.

1.4.3 Morse–Witten Model

One of the main issues with the Soft Disk model is that it does not conserve bubble area as it does not allow bubbles to deform. The Plat implementation of the two dimensional foam model does conserve area and allows bubbles to deform, but it fails in the wet limit. Therefore, we wish to create a two dimensional model for foams which combines some of the simplicity of the Soft Disk model with deformable bubbles away from the wet limit.

To do this we turn to the work of Morse and Witten [48]. The result of that work is a relationship between an applied force on a bubble and the deformation of the bubble in response. Morse and Witten obtained an expression for the deformation of a bubble from spherical, shown in three dimensions in Figure 1.11 (a) and in two dimensions in Figure 1.11(b). Also shown in Figure 1.11(c) is the response of a bubble to several applied forces. A main result of this is that the interaction between three dimensional bubbles is logarithmically soft for small deformations, much softer than a harmonic interaction. This non-linear scaling is weaker than the Hertzian $f^{-1/3}$ seen for contacting elastic solids [49], but it still dominates the energetics of weakly compressed foams.

A visually striking feature of this model in three dimensions is the logarithmic divergence of the bubble profile at the point of contact. This can be seen clearly in Figure 1.11 (a). While initially quite alarming, as no physical bubble does this, the divergent part of the bubble profile may be safely discounted, as detailed in Chapter 3.

The original model derivation will be elaborated on in Chapter 3, as well as the two dimensional analogue. The process of building a model of two dimensional foam from the force-deformation relation will also be detailed. Chapter 4 will show a different type of application of the three dimensional Morse−Witten theory. With it we can estimate the surface tension of a liquid−gas interface using two simple length measurements.

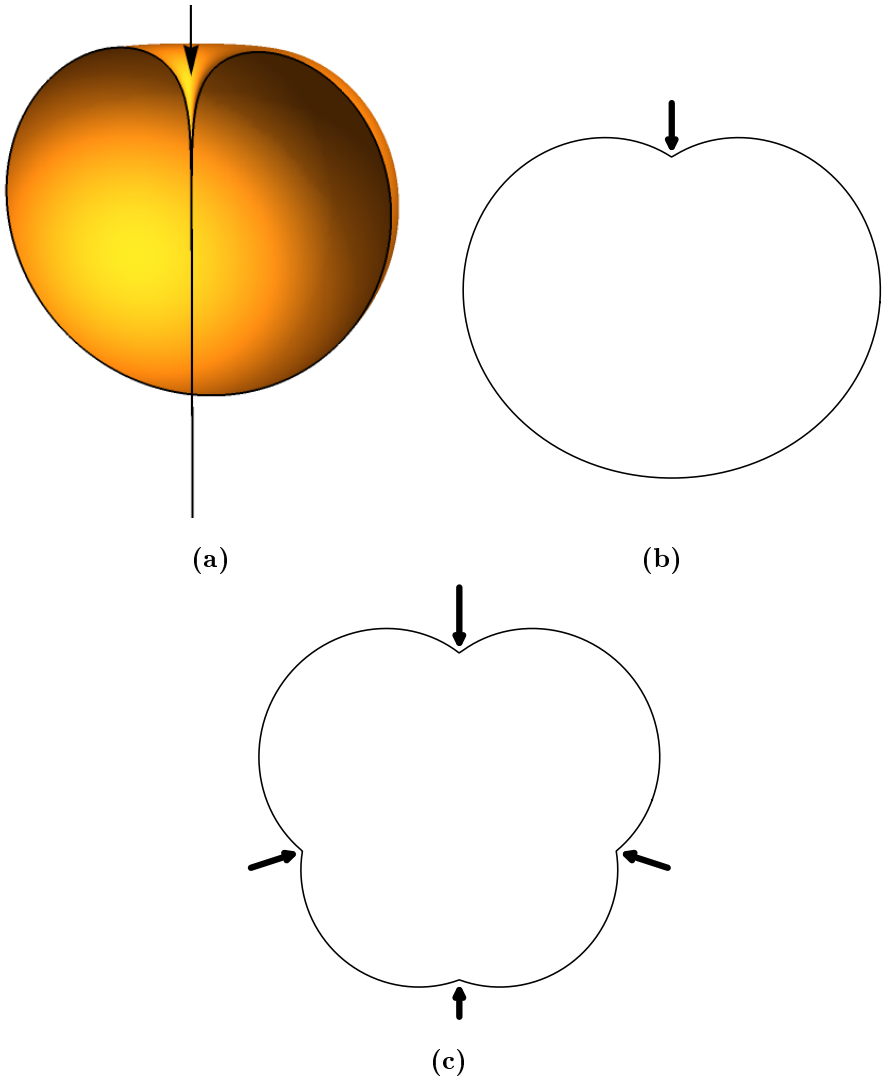

Figure 1.11: Examples of bubbles in the Morse−Witten theory in two and three dimensions. (a) A slice through a three dimensional Morse−Witten bubble under the action of a point force and a compensating body force. The divergence of the profile at the point of contact can be seen clearly. When representing a contact with a flat surface in this model the convex part of the profile outside of the dimple is used and the divergence can be safely ignored. (b) A two dimensional bubble under the action of a single point force and a compensating body force. (c) The response of a two dimensional bubble to multiple point forces.

Chapter 2

Studying Two Dimensional Foams with Plat

This chapter describes results for two dimensional foams, as obtained from exhaustive computer simulations using the software Plat, introduced in Section 1.4.1. Plat was used extensively throughout the 1990s; as much as was possible given the available computing resources at the time. With this preliminary data, Bolton and Weaire suggested that the critical behaviour (that is, the behaviour in the wet limit) of the coordination number is linear with liquid fraction [33], contradicting the square root scaling with liquid fraction described in Section 1.2.4 for Soft Disk simulations. They experienced some difficulty in thoroughly exploring the critical region. The issues with the software that make finding equilibrium structures in the wet limit difficult appear to be inherent in the simulation method. We have explored these somewhat, but not made an attempt at fixing them in this chapter. Indeed, it appears to be somewhat of a hard problem, which will be outlined in Section 5.1.1. Instead, we have taken advantage of over 25 years of improvement in computing technology to revisit the Plat software with a

brute force approach in order to explore the wet limit.

Before detailing the workings of the Plat simulation, I will revisit other critical phenomena that two dimensional foams have been found to exhibit in the wet limit. Following this, I will detail how Plat implements the standard model of two dimensional foams, along with the procedure used in the simulations. The first data analysed will be the variation of energy and of the coordination number with liquid fraction to complement previous work. Subsequently, the occurrence of cascades of bubble rearrangements in the wet limit is analysed. The coordination number variation provided some results that contrast with much of the literature so that will then be revisited and compared in detail with results from the soft disk model. This will show that the deformation of the bubbles due to area conservation plays an important role. This was our main motivation to develop the Morse−Witten model for two dimensional foams, as will be described in Chapter 3.

2.1 The Plat Software

2.1.1 Details of the Implementation

Plat, as mentioned in Section 1.4.1, is a software package for the simulation of a foam in two dimensions. It is based on the direct implementation of Plateau's Laws, rather than an energy minimisation routine.

The simulations are initialised as follows: samples are generated by filling a square box (see Figure 2.1) with a random Delauney tessellation of triangles [50]. A Delauney tessellation is a special way to join up a set of points into triangles where, if a circumcircle is drawn through the three points used as the corners of a triangle, there are no other points within the circle. The Delauney tessellation is constructed by first randomly scattering N points

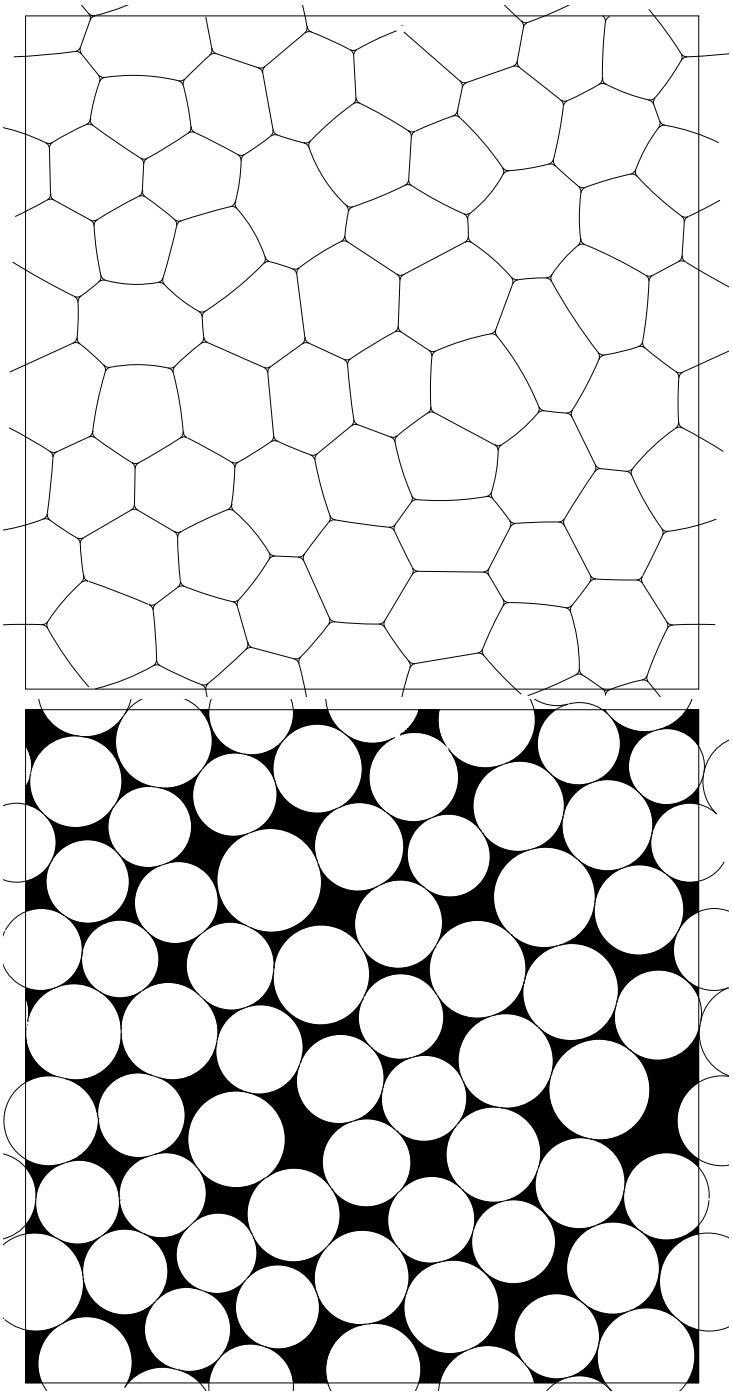

Figure 2.1: Example of initial (dry, $\phi = 0.002$) and final (wet, $\phi = 0.165$) stages of a sequence of Plat simulations for a foam with 60 bubbles. Note the periodic boundary conditions.

in the simulation box. (The randomness of bubble areas is controlled by specifying a minimum separation between points, the so-called *hard disk parameter* as described by Weaire and Kermode [51]. A lower minimum separation results in greater polydispersity.) These points are then connected into a triangular tessellation of the box. The definition of the tessellation is used to connect the random points together.

Next, the Delauney tessellation is inverted to obtain its dual graph, a Voronoi network. In this transformation, the random points used as the corners of the triangles become the centres of the Voronoi cells. It is these cells that represent the bubble in the simulation. The circumcentres of each triangle become the corners of the Voronoi cells. Once the transformation is complete, the resulting Voronoi network is converted to a relatively dry foam ($\phi < 0.002$), not yet equilibrated, by "decorating" its vertices with small three-sided Plateau borders at equal pressures. This initialisation procedure is provided by Plat and is based on the procedure described by Kermode and Weaire [52].

The decorated Voronoi network is equilibrated into a two dimensional foam by adjusting cell pressures and vertex coordinates in order to fulfil the constraints of fixed cell areas and smoothly meeting arcs. The cell pressures are updated by

$$\Delta p_i = -\frac{\gamma_A \Delta A_i}{\frac{\partial A_i}{\partial p_i}}, \tag{2.1}$$

where ΔA_i is the existing discrepancy of the current cell area from the true area, $\frac{\partial A_i}{\partial p_i}$ is the numerically determined area derivative, and γ_A is a damping factor required to stabilise the algorithm. The cell pressures change the cell areas by controlling the boundary curvatures. This step is repeated until the fixed cell areas are correct.

The vertex coordinates are changed such that the boundaries meet smoothly

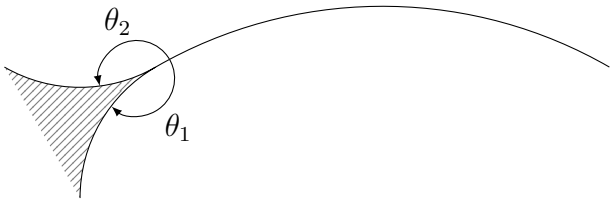

Figure 2.2: The equilibrium condition for smoothly meeting arcs demands that $\theta_1 = \theta_2 = \pi$

at each vertex. In this way, the conditions of the standard two dimensional foam model (Plateau's laws and the Young−Laplace law) are fulfilled (see Section 1.4.1). The increments $(\Delta x_k, \Delta y_k)$ are calculated via

$$\begin{pmatrix} \Delta x_k \\ \Delta y_k \end{pmatrix} = \gamma_\theta \begin{pmatrix} \frac{\partial \theta_1}{\partial x_k} & \frac{\partial \theta_1}{\partial y_k} \\ \frac{\partial \theta_2}{\partial x_k} & \frac{\partial \theta_2}{\partial y_k} \end{pmatrix}^{-1} \begin{pmatrix} \pi - \theta_1 \\ \pi - \theta_2 \end{pmatrix}, \tag{2.2}$$

where the angles θ_1 and θ_2 are as in Figure 2.2, the derivatives are calculated numerically, and γ_θ is a damping factor. This process is repeated until the largest vertex increment falls below a convergence threshold. The threshold is an adjustable fraction of the average Plateau border radius, defaulting to 0.02. See also [31] for a detailed discussion of the Plat representation of a foam and the equilibration process.

There are two types of topological changes implemented during equilibration. These correspond to the two components of a T1 change (Section 1.3.6). Cells lose contact when the vertices at either end of their shared cell−cell boundary come within an adjustable fraction (defaulting to 0.01) of the average radius of a Plateau border of each other. Cells come into contact when their corresponding cell−border arcs overlap across a Plateau border.

If a cell with three neighbours loses a contact, it does not turn into a "rattler", but remains attached to its remaining neighbours. This procedure has been chosen because, in this case, the bubble remains part of the foam

network and can be dealt with easily. Even towards the wet limit, the fraction of bubbles with just one or two contacts combined is less than 4% (see Section 2.2.4).

2.1.2 Simulation Procedure

The simulations presented here progress by increasing the liquid fraction in steps of $\Delta\phi = 0.001$ and equilibrating the foam at each step. Increases in liquid fraction are performed by proportionally reducing bubble areas (rather than increasing the total simulation area). This involves decreasing the cell pressures in order to reduce the curvature of the liquid−gas interfaces, followed by the equilibration of vertex positions. The change in pressure of every cell undergoes one iteration before each vertex position undergoes one iteration, and the two are brought towards equilibrium together. Calculations of foam energy and/or average coordination number are made after each equilibration.

Examples of structures simulated by Plat are shown in Figure 2.1. It is the natural extension to wet foam of the earlier two dimensional "FROTH" simulation method of Weaire and Kermode [53, 51, 52] for dry foam. Doubts were expressed at the time of the inception of FROTH as to whether the method might encounter anomalous equilibrium configurations not representative of a real two dimensional foam. Thankfully, there is no evidence that this is the case in practice. However, Plat exhibits a tendency to no longer succeed in equilibrating the foam structure at high liquid fractions for systems larger than about 20 bubbles, as mentioned in Section 1.4.1. As Plateau borders tend to become semicircular, it is increasingly difficult to fit an arc of the correct curvature between its end points and the system no longer converges. This is indeed the potential difficulty that was anticipated

by Weaire and Kermode [53, 51]. As foams get wetter, large many-sided Plateau borders become much more likely to be susceptible to involve such anomalous arcs. This has not yet been positively identified as the root cause of the convergence issues, nor has an attempt at refining the program been made yet. Some suggestions on how to tackle this issue will be outlined in Section 5.1.1.

To reduce size effects we would prefer to use samples that are as large as possible. Plat can reliably simulate dry foams with up to 500 bubbles, but for systems with more than 20 bubbles it begins to exhibit failure from liquid fractions of 0.1 and higher, with increasing frequency for larger systems. This frequent failure of Plat made it impractical to simulate a full range of liquid fraction for samples exceeding about 100 bubbles. As a compromise between systems size and simulation reliability, we decided that each simulation would consist of only 60 bubbles, and the properties of the simulations would be averaged over multiple simulations. For the purposes of this thesis, all Plat simulation results presented are the averaged results, regardless of the liquid fraction reached. For details of averaging and statistics, see Section 2.2.1.

2.2 Simulation Results for Basic Quantities of Interest

Before proceeding to the analysis of rearrangements, I will present results for various basic quantities of interest, complementing and completing previously published data from Plat [33, 30, 31, 36, 54].

2.2.1 Averaging of Simulations and Statistics

All the results presented in this section are calculated and averaged across almost 600,000 simulations of 60 bubbles each. Not all simulations ran to completion, this can be seen in the decline of the statistics shown in Figure 5.2. These statistics nevertheless appear to be more than adequate for our purposes as we have at least 100 simulations for $\phi < 0.1585$.

Such a large number of simulations would have been entirely unachievable in the 1990s when Plat was originally written. The (successful) calculation of one single 60−cell sample for a range of values of liquid fraction would have taken several hours.

The polydispersity of the simulations was measured to be $\sigma_R = 0.072$. While this is less than the critical value of 0.1 mentioned in Section 1.2.2, visual inspection of the simulations such as Figure 2.1 shows a sufficient lack of positional correlation that we consider them to be disorded.

2.2.2 Variation of Energy with Liquid Fraction

Figure 2.3 shows the variation of the reduced excess energy, $\varepsilon(\phi)$, as a function of liquid fraction (Equation (1.3)). Close to the wet limit a cubic function, (see Equation (2.3)) fits this well. This gives a critical liquid fraction of $\phi_c = 0.166 \pm 0.005$ for the wet limit.

$$\varepsilon(\phi) = 0.31(\phi_c - \phi)^2 + 3.7(\phi_c - \phi)^3 + (2 \times 10^{-4}). \tag{2.3}$$

This value of ϕ_c is consistent with other numerical results of 0.159 and 0.16 for two dimensional foams [33, 2], and experimental values of 0.16 and 0.158 [55, 22] and numerical results of 0.159 and 0.16 [34, 56] results for random packings of disks. However, this is a four parameter fit. A simpler fit involving only two parameters is obtained from considering the variation

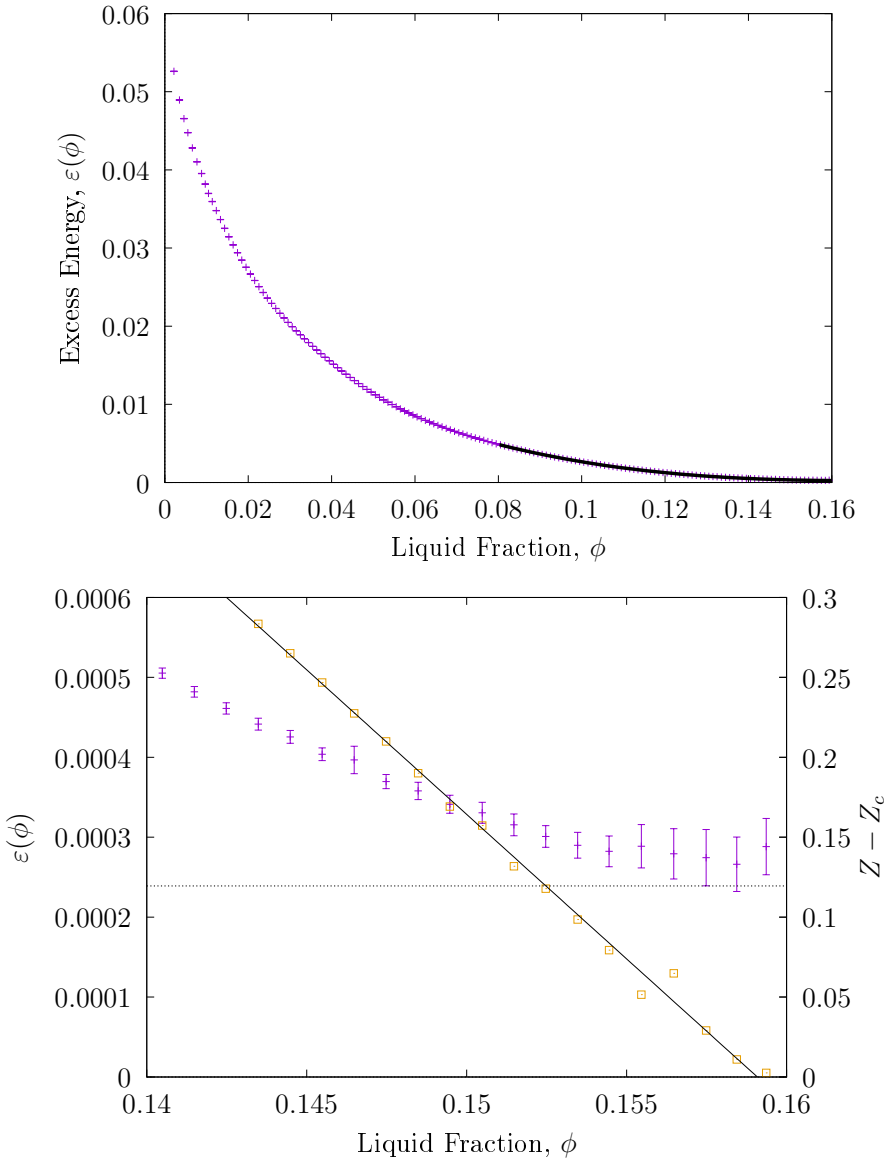

Figure 2.3: Top: Variation of reduced excess energy, $\varepsilon(\phi)$, with liquid fraction, ϕ. The solid line is a fit to Equation (2.3) for $\phi > 0.08$, over which range it shows good agreement. Bottom: The variation of $\varepsilon(\phi)$ in the wet limit ($\phi > 0.14$) − plus signs, left y-axis. Error bars indicate the standard error of the sample mean. Also shown is the linear variation of excess coordination number $(Z - Z_c)$ with liquid fraction − squares, right y-axis. The solid line corresponds to the two parameter fit $Z(\phi) - Z_c = a * (\phi_c - \phi)$, where $a = 17.9$ and $\phi_c = 0.159$ are the fit parameters, and $Z_c = 4(1 - 1/60) = 3.93$ is fixed.

of $Z(\phi)$ (see Figure 2.3 (bottom), and Section 2.2.3 below). This results in $\phi_c = 0.159 \pm 0.001$ [2] and it is this value that we will use when discussing large scale rearrangements in Section 2.3. The very small offset (the last term in Equation (2.3)) is barely visible on the scale of the main plot of Figure 2.3. Further calculations with tighter criteria (halving the fraction of a Plateau border used as a minimum length) for convergence have indicated that this small discrepancy is due to limited convergence. Given the extensive nature of these calculations, as described above, we have not repeated them in full to investigate this further.

2.2.3 Variation of Average Coordination Number with Liquid Fraction

In order to investigate the variation of $Z(\phi)$ close to ϕ_c, and the value of ϕ_c itself, we plotted $\log(Z(\phi) - Z_c)$ vs. $\log(\phi_c - \phi)$. We then varied ϕ_c, to obtain the value which gives the best linear relationship between these quantities (see Figure 2.4, bottom). In this way, the critical liquid fraction was found to be $\phi_c = 0.159 \pm 0.001$, and the slope was 1.000 ± 0.004 in the logarithmic plot.

The conclusion is, therefore, that Z approaches Z_c linearly, i.e. $(Z - Z_c) \sim (\phi_c - \phi)$ as plotted in Figure 2.16. Appropriately, fitting

$$Z = Z_c + k_{\mathrm{f}}(\phi - \phi_c), \tag{2.4}$$

with $Z_c = 4 - 1/15$ gives a slope of $k_{\mathrm{f}} = 17.9 \pm 0.1$ and a critical liquid fraction of $\phi_c = 0.159 \pm 0.001$. Above, in Section 2.2.2, we obtained a critical liquid fraction of $\phi_c = 0.161 \pm 0.001$ for the same system by looking at the excess energy. This is consistent with the results of Section 2.2.2.

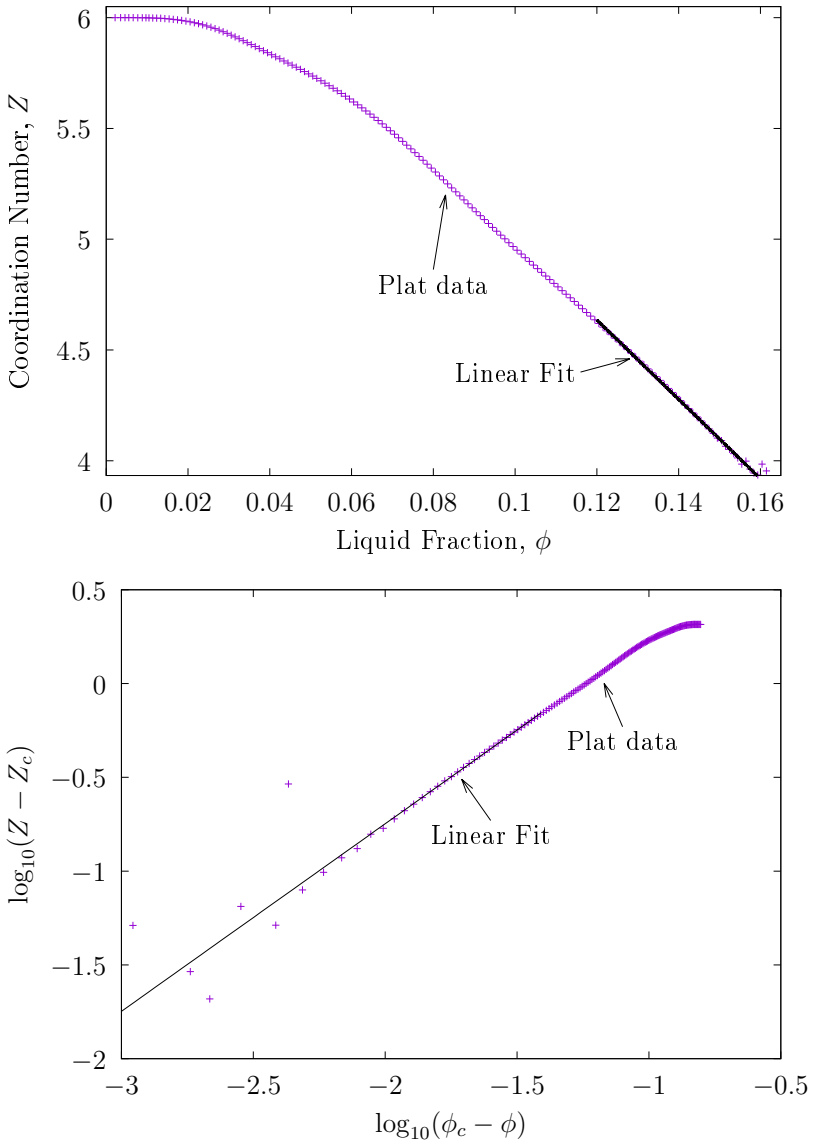

Figure 2.4: Top: Coordination number, Z, versus liquid fraction, ϕ. The linear behaviour is not restricted to the wet limit; it continues over a substantial range of ϕ. Note the slight plateau in the dry limit where Z remains constant at a value of six for $\phi < 0.01$ at least. This happens because the Plateau borders with more than three sides are still unstable so the total number of contacts cannot decrease. Bottom: Logarithm of $(Z - Z_c)$ versus logarithm of $(\phi_c - \phi)$ in order to fit ϕ_c and to examine the behaviour of $Z(\phi)$ close to ϕ_c. The increased scatter is due to the reduced number of simulations close to the wet limit.

2.2.4 Distribution of Coordination Number

I now turn to the distribution of coordination numbers and present an empirical procedure, inspired in part by the analysis of van Hecke [21], reproduced in Figure 2.5 and Equations (2.5)-(2.8). The variance of van Hecke's data, σ^2, was 0.75. Equations (2.5)-(2.8) were applied separately to the left and right parts of Figure 2.5.

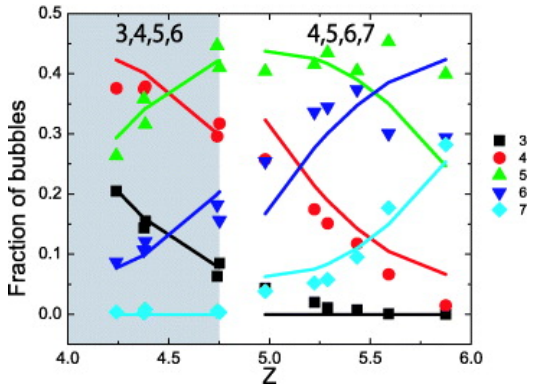

Figure 2.5: Figure reproduced from [21] showing fractions of bubbles in the foam with n contacts as a function of Z. Solid lines: solutions to Equations (2.5)-(2.8) for the species listed at the top of the graph.

$$x_n = \frac{1}{4}\left((Z-(n+2))^2 + \sigma^2 - \frac{1}{2}\right) \tag{2.5}$$

$$x_{n+1} = \frac{1}{4}\left(-(Z-(n+1))^2 - \sigma^2 + \frac{5}{2}\right) \tag{2.6}$$

$$x_{n+2} = \frac{1}{4}\left(-(Z-(n+2))^2 - \sigma^2 + \frac{5}{2}\right) \tag{2.7}$$

$$x_{n+3} = \frac{1}{4}\left((Z-(n+1))^2 + \sigma^2 - \frac{1}{2}\right) \tag{2.8}$$

Figure 2.6 shows distributions for the fraction of bubbles with n neighbours as a function of Z. Here we propose the function $f(n)$ (a normal distribution), involving only a single free parameter σ (the standard deviation

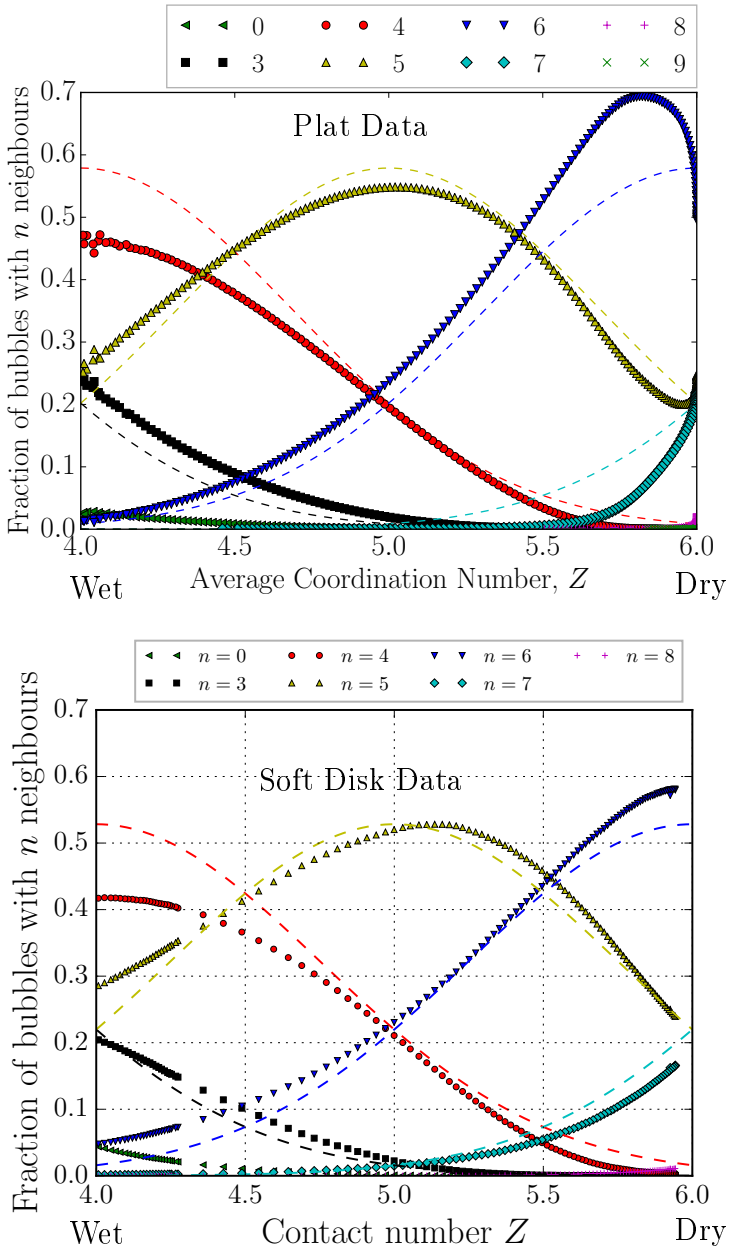

Figure 2.6: The fraction of bubbles with n neighbours as a function of average coordination number, Z (top: Plat, bottom: Soft Disk). Simulation data (symbols) can be approximated by the functional form of Equation (2.9) (dashed lines), with only a single fit parameter $\sigma \simeq 0.684 \pm 0.004$ for all the data. Note that despite the differences in $Z(\phi)$ between the two models, the distribution of contacts for a given Z is very similar.

of the distribution), as an adequate description of the data,

$$f(n) = \frac{1}{\sigma\sqrt{2\pi}} \exp\left(\frac{-(Z-n)^2}{2\sigma^2}\right), \tag{2.9}$$

where Z is the coordination number, as above, and the value of σ used in Figure 2.6 is 0.684, which was found by a least squares fit to the data. This can be considered to be a continuous analogue of Equations (2.5)-(2.8). It appears likely that the width of this distribution is connected with the polydispersity of the sample, but this has not been investigated yet. Note that in this analysis bubbles with 0, 1, and 2 neighbours are grouped together as having 0 contacts as they are all rattlers.

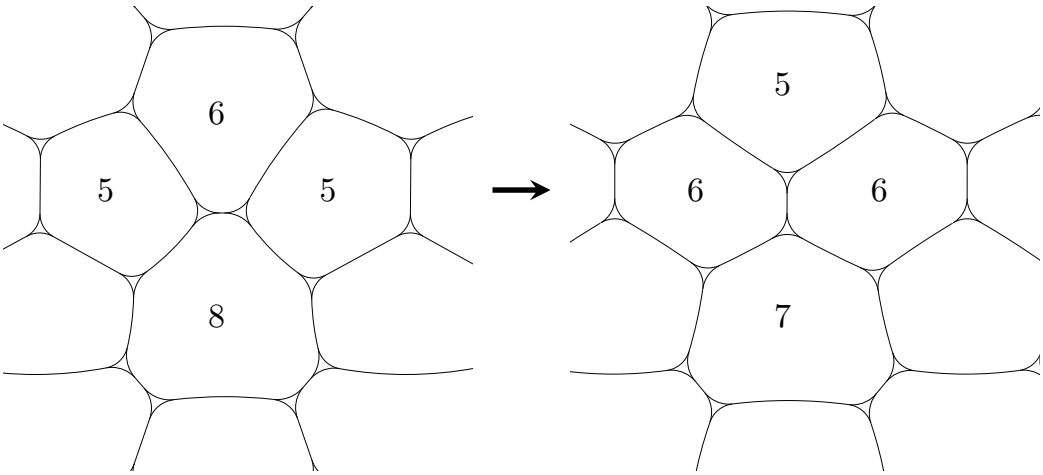

Figure 2.7: Example of a T1 transition where the average coordination number, Z, is unchanged, but the distribution $f(n)$ does change. The numbers indicate the number of neighbours of each bubble involved in the T1.

One notable feature of these statistics for the Plat data that is not represented in the simple fitting function is the steep variation of the curves as Z tends to six. Recall that, for $\phi < 0.05$, only T1 rearrangements that do not change Z are possible (see Section 1.3.6). Such combined changes have no effect on the average coordination number, Z, which remains at the value

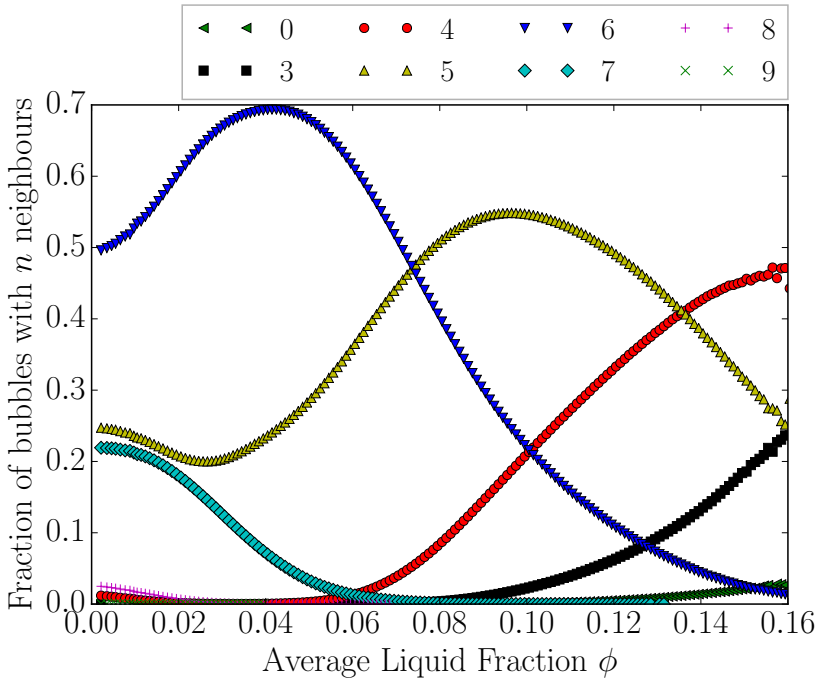

Figure 2.8: The fraction of bubbles with n neighbours as a function of liquid fraction, ϕ for the Plat simulations. Note the minimum in the fraction of five sided bubbles around $\phi \simeq 0.03$ and the maximum in the fraction of six sided bubbles around $\phi \simeq 0.04$.

six, but do affect the distribution $f(n)$, see Figure 2.7. Accordingly, it can be seen in Figure 2.6 that the derivatives $\mathrm{d}f/\,\mathrm{d}Z$ are infinite at the dry limit. However, for the Soft Disk data, there is no such feature at $Z = 6$. This is likely due to the overly simplified Soft Disk model which uses unrealistic bubble-bubble interactions which lack area conservation. In Figure 2.8 it can be seen that by plotting the distributions for the fraction of bubbles with n neighbours as a function of liquid fraction, ϕ, there are no steep vertical slopes in any of the curves at $\phi = 0$.

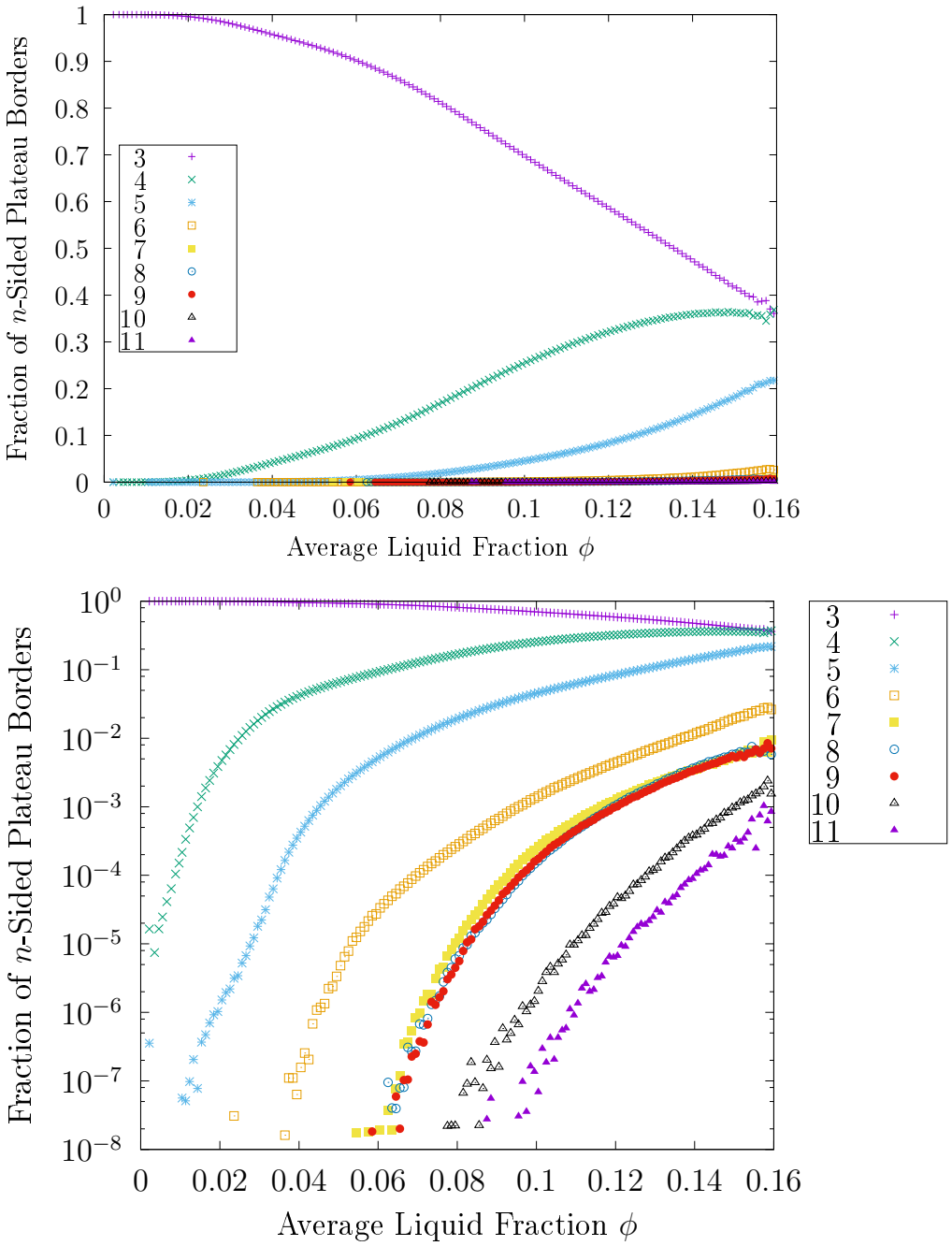

Figure 2.9: Distribution of number of sides of Plateau borders as a function of liquid fraction. Top: The three sided Plateau borders clearly dominate the statistics for any $\phi \lesssim 0.14$. Bottom: The same data with a logarithmic y axis. This shows that a Plateau border with $n+1$ sides is roughly 10 times less likely than one with n sides.

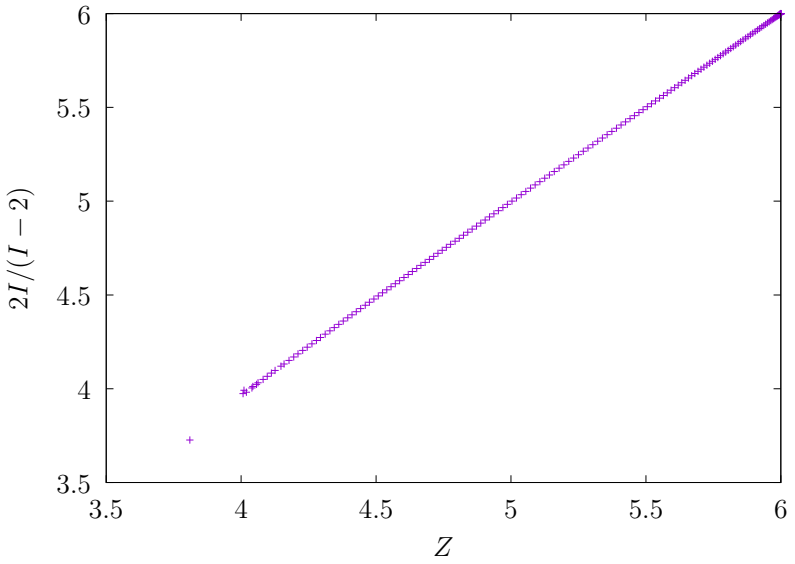

Figure 2.10: Euler's equation versus average coordination number [15]. I is the average number of sides of the Plateau borders. The perfectly straight line verifies that Euler's equation (Equation (2.10)) holds in the Plat simulations.

2.2.5 Distribution of Plateau Border Sides

For completeness, the distribution of the number of sides of the Plateau borders as a function of ϕ is shown in Figure 2.9. This data complements data presented by Hutzler and Weaire [15]. The previous dataset was very limited, while Figure 2.9 is very thorough and complete.

The distribution of number of sides of Plateau borders can be related to the average coordination number via Euler's equation

$$Z = \frac{2I}{I-2}, \tag{2.10}$$

where I is the average number of sides of the Plateau borders in the foam [15]. Figure 2.10 shows that this holds for the Plat simulations.

2.3 Statistics of Bubble Rearrangements

As introduced in Section 1.2.5, the shear modulus and yield stress of foams go to zero in the wet limit. Hutzler *et al.* [36] observed an associated phenomenon, which can be considered to be an additional aspect of the critical behaviour associated with the wet limit. This is the occurrence of cascades of contact changes during equilibration in response to a small stress increment above the yield stress.

The size of the cascades was found to increase with the liquid fraction, possibly tending to infinity (and thus preventing Plat from converging) at the wet limit. However, it was not feasible for Hutzler *et al.* to fully explore the wet limit, at which point the size of the cascades was expected to diverge. Here we return to this phenomenon, using a progressive increase of liquid fraction, rather than stress, as the small perturbation. Where the previous results had to rely on counting the number of contact changes that occurred over the course of the equilibration routine, we will use the technique of successive adjacency matrices described in Section 1.4.1 to approach this more thoroughly.

There are two types of elementary rearrangements in a two dimensional foam of finite liquid fraction, in which a contact between two bubbles is either gained or lost, see Figure 2.11. In what follows, I will count the fraction of bubbles involved in rearrangements in any given step, rather than the rearrangements themselves. Another alternative would be to measure changes in the energy of the system, as Durian did for the more rudimentary bubble model [34, 57] discussed in Section 1.4.2.

As the wet limit is approached, it becomes particularly evident that more elementary rearrangements are provoked by a small increment of ϕ.

The number of rearranged bubbles in one step is computed from the

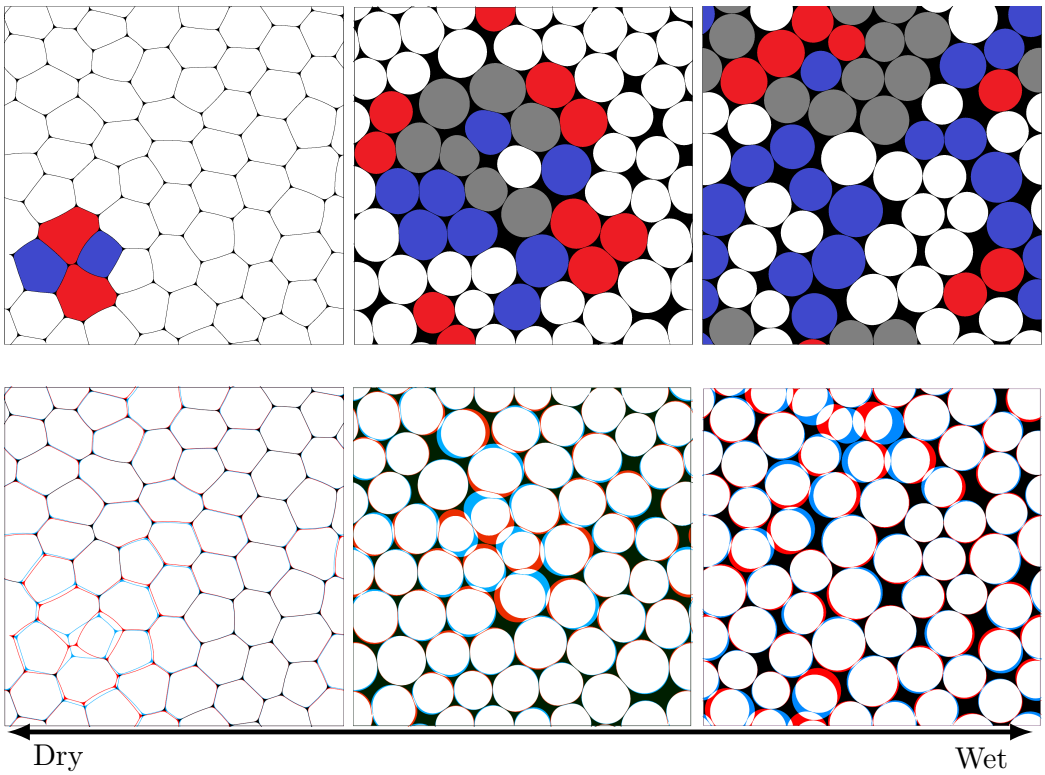

Figure 2.11: Two alternative illustrations of rearrangements due to a small increase in liquid fraction. Top row – Red bubbles lose contacts, blue bubbles gain contacts, and gray bubbles both gain and lose contacts. Bottom row – Red is the liquid before rearrangements, blue is the liquid after rearrangements, and black is unchanged liquid. Left: in a dry foam ($\phi = 0.006$), an increase in liquid fraction $\Delta\phi = 0.001$ only leads to localised rearrangements. Centre: example of extensive rearrangements in a moderately wet foam ($\phi = 0.112$). Right: Rearrangements involving nearly two thirds of all bubbles in a foam ($\phi = 0.149$) close to the critical liquid fraction. Note that the regions in which changes occur appear spatially connected.

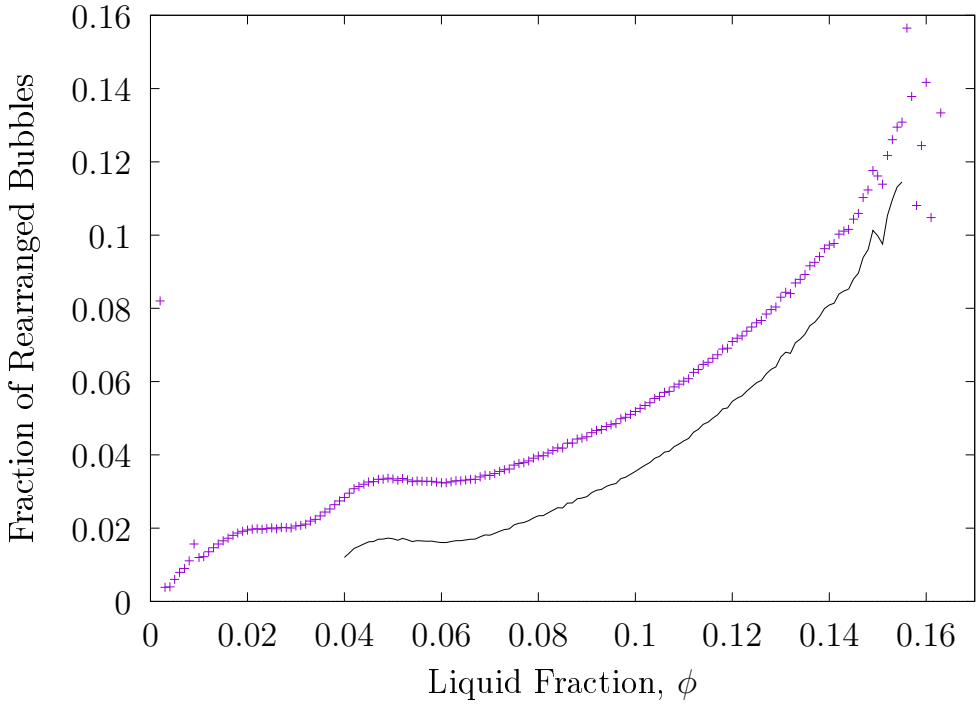

Figure 2.12: Fraction of rearranged bubbles in a sample due to an increase in liquid fraction by $\Delta\phi$ as a function of liquid fraction ϕ. Data points are an average of 10^5 simulations containing 60 bubbles each, with $\Delta\phi = 0.001$. The solid line corresponds to a linear extrapolation of this data to the limit: $\Delta\phi \to 0$. See Figure 2.13.

change of the adjacency matrix between two equilibrium states, as described in Section 1.3.6. Shown in Figure 2.12 is the fraction of bubbles involved in rearrangements (as averaged over all our simulations) when increasing the liquid fraction from ϕ to $\phi + \Delta\phi$ in small increments, $\Delta\phi = 0.001$. Since this average depends on the size of $\Delta\phi$ we have repeated the calculation for a range of values of $\Delta\phi$ from 0.005 to 0.0005 and used this data to linearly extrapolate to the limit $\Delta\phi \to 0$.

The main plot of Figure 2.13 shows the average fraction of rearranged bubbles due to an increase in liquid fraction from ϕ to $\phi + \Delta\phi$ for six different values of $\Delta\phi$. The dependence of this average fraction on $\Delta\phi$ can be studied by taking vertical slices through this data. We have done this for four different values of ϕ, indicated by the lines labelled "Liquid fractions for fits". The result is shown in the inset plot. The average fraction of rearranged bubbles is seen to decreases to a non−zero value when we extrapolate $\Delta\phi$ to zero. The straight line fits contained in the inset all have slopes within error of each other, indicating that the linear shift due to non-zero $\Delta\phi$ is constant. As such, we take an average of the fits, giving an offset of $-(16.4 \pm 0.5)\Delta\phi$. The result of this extrapolation is shown as a solid line in Figure 2.12;

We also generated histograms of the number of rearranged bubbles per step for all our simulation data, at each liquid fraction. Viewing these histograms on a semi−log scale reveals that the tail of the distribution can be well approximated by an exponential distribution (see Figure 2.14, top) of the form:

$$p(\zeta) = \lambda \exp(-\lambda\zeta), \tag{2.11}$$

where ζ is the fraction of rearranged bubbles and λ is called the decay parameter.

For an exponential distribution $1/\lambda$ equals the mean of ζ. Instead of

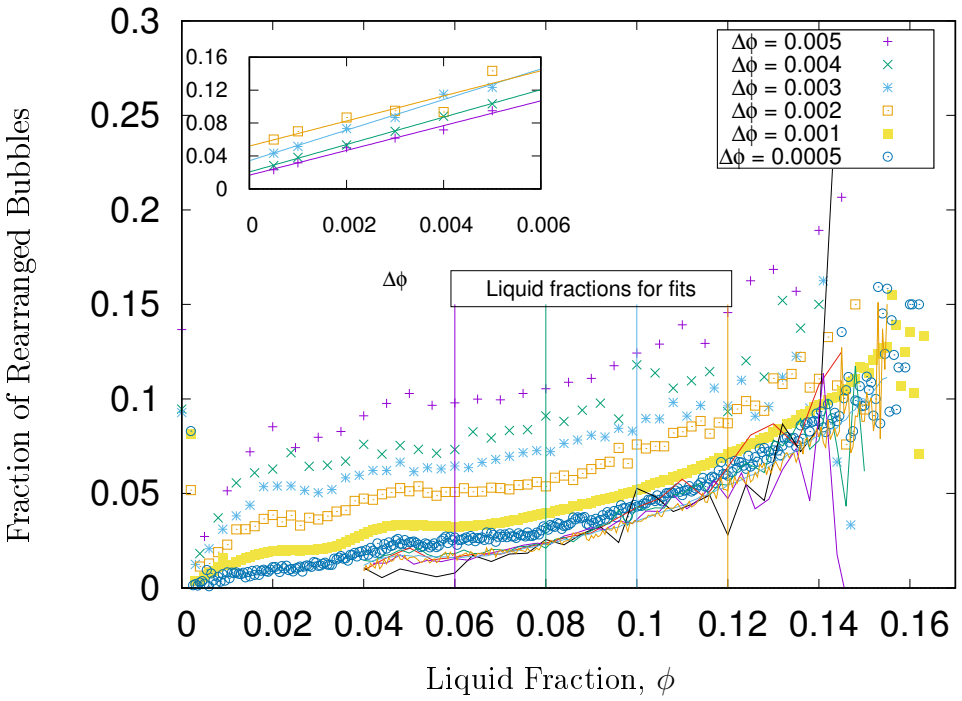

Figure 2.13: Fraction of rearranged bubbles in a sample due to an increase in liquid fraction by a range of $\Delta\phi$ values, each as a function of liquid fraction ϕ (data averaged over 10^5 simulations for $\Delta\phi = 0.001$, and 10^3 simulations for all other values of $\Delta\phi$. Each simulation contains 60 bubbles with $\sigma_R = 0.07$). Inset: Fraction of rearrangements as a function of step size $\Delta\phi$. Data sampled at liquid fractions indicated on the main figure. Solid lines mark the interpolations as $\Delta\phi \to 0$. These solid lines indicate the number of rearrangements that are due to the perturbation of the system, rather than the actual change in liquid fraction.

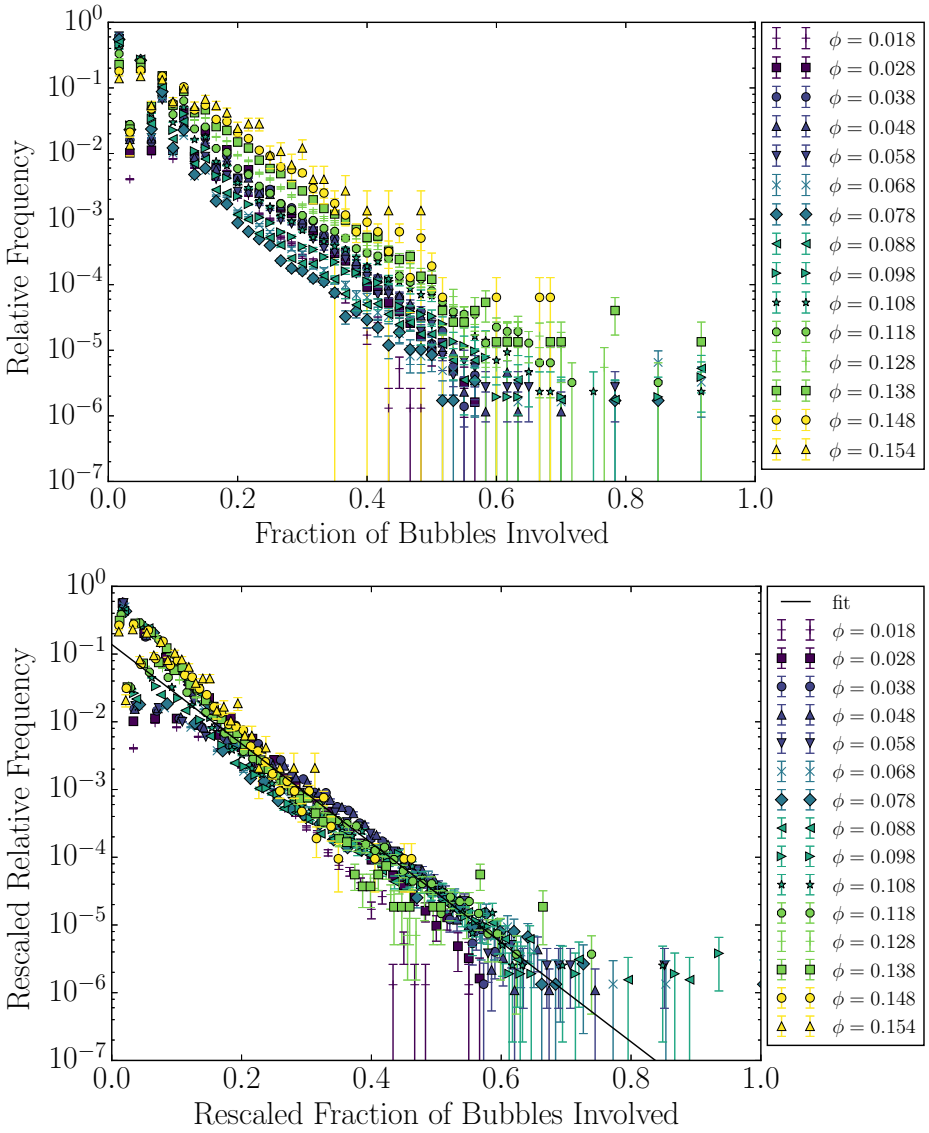

Figure 2.14: Top: Log-linear plot of histograms of the fraction of bubbles involved in rearrangements. Bottom: Manually rescaled histograms as described in the text. The solid line is a straight line fit with slope $\lambda_0 = 17 \pm 2$, showing that the tail is well approximated by an exponential form of Equation (2.11).

fitting 15 different exponentials (corresponding to the 15 datasets shown in Figure 2.14 (top)), resulting in 15 values for λ as a function of ϕ, we have chosen to rescale the data by a scale factor $l(\phi)$ which depends on liquid fraction. In this rescaling $\zeta \rightarrow \zeta/l(\phi)$ and $p(\zeta) \rightarrow l(\phi) * p(\zeta)$ so that the normalisation of the area under the histogram is preserved. This leads to a collapse of the data, as shown in Figure 2.14 (bottom). This rescaled dataset is fitted to Equation (2.11), resulting in one decay parameter, $\lambda_0 = 17 \pm 2$. Then $\lambda(\phi) = \lambda_0/l^2(\phi)$. Figure 2.15 shows the variation of $1/\lambda$ with liquid fraction, ϕ. In the wet limit, the reciprocal of λ tends quadratically to a constant of $1/\lambda(\phi_c) = 0.150 \pm 0.001$, whose value or origin is, as yet, unclear.

Rather than describing the data with an exponential, we have also probed for a power law. However, the limited size of the Plat simulations (60 bubbles) makes is difficult to find a power law, as the range of sizes of events simply is not large enough. Regardless, preliminary analysis indicates that the exponent would decrease in the limit $\phi \rightarrow \phi_c$, making us believe that the exponential distribution is a more appropriate model for the data. Whether this is due to a characteristic of the system, or size effects is not known at this stage.

The cascades of rearrangements bear a resemblance to avalanches. There are a variety of physical systems which exhibit avalanches, ranging from earthquakes [58] and random fuse networks [59], to piles of rice [60]. However, their statistics are usually described by power-laws of the form $p(x) \sim x^{-\alpha}$, where the exponent α has a value between one and two. Indeed, power-laws are often seen as a signature feature of complex systems [61], which also include foams [62]. These have been found, for example, in the statistics of particle rearrangements in flowing colloidal suspensions [63] and the statistics of popping bubbles in collapsing foams [64].

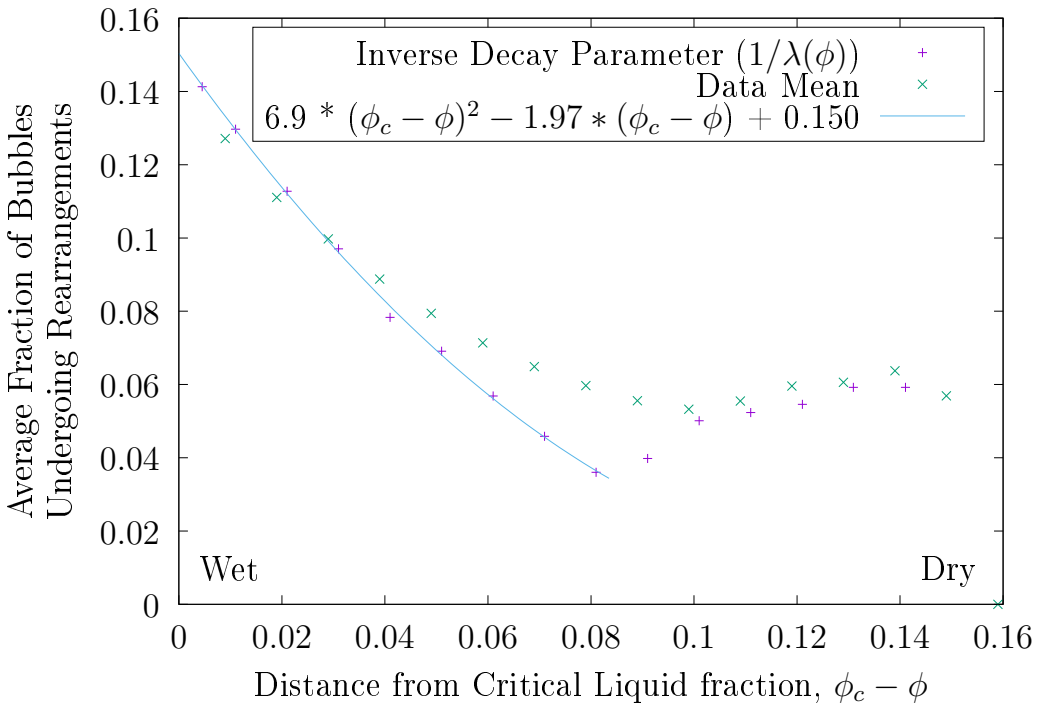

Figure 2.15: Variation of the decay parameter, λ, with liquid fraction, ϕ. $\lambda(\phi) = \lambda_0/l^2(\phi)$, where λ_0 (obtained from Figure 2.14 (bottom)). The solid line is a fit of the form $(6.9 \pm 0.9) \times (\phi_c - \phi)^2 + (-1.97 \pm 0.07) \times (\phi_c - \phi) + (0.150 \pm 0.001)$. Also shown is the mean of the fraction of bubbles involved in rearrangements as a function of liquid fraction (see Section 2.3). The disagreement in the central region of the plot may be due to the inaccuracy of the manual rescaling.

Power law distributions of changes in energy with an exponential cut−off for high energies have been observed in simulations by Durian [57] in packings of soft disks under shear. For these Soft Disk systems, it has been suggested that a pure power−law distribution only occurs at the wet limit [65]. Such simulations, where bubbles are modelled as overlapping disks, are successful in reproducing many rheological properties of foams. However, recent work points to marked differences regarding the variation of average coordination number, $Z(\phi)$, in the wet limit (see Section 2.4.1) [2].

A transition between power law and exponentially distributed avalanches was observed by Ritacco *et al.* [66] and Frette *et al.* [60]. The former was for coalescence of bubbles in a bubble raft, while the latter was observed in sliding grains in rice piles. In both cases, the statistics were controlled by the dissipative forces in each system, viscosity [66] and friction [60] respectively. Our simulations are quasi-static and, therefore, involve no dynamic processes or dissipative forces. We are, therefore, unable to find an analogous control parameter for the distribution of our large scale rearrangements. As such, the reason why the distribution of rearrangements in our simulations follows the exponential form of Equation (2.11) remains elusive at this stage. There have been experiments with three dimensional foams [67] for which avalanches of rearrangements following an increase in liquid fraction have been observed, but there is no statistical data available.

2.4 Comparison of $Z(\phi)$ between Plat and the Soft Disk Model

For a comparison with the Soft Disk model, random packings of overlapping disks with similar conditions as in Plat (same polydispersity i.e. $sigma_R =$

0.07, same sample preparation protocol .i.e liquid fraction increased from 0 to 0.16 in steps of $\Delta\phi = 0.001$) were created using a conjugate gradient energy minimisation routine [68]. The average for $Z(\phi)$, excluding rattlers, was taken over 20,000 independent simulations.

2.4.1 Discussion of Previous Results for $Z(\phi)$

The linear increase of the average coordination number with liquid fraction found in the Plat simulations close to the wet limit (Equation (2.4)) is unexpected, since it is at odds with previous findings from computation, theory, and experiment. As an illustration, Figure 2.16 shows both results from Soft Disk simulation and Plat simulations with the same distribution of bubble sizes in both.

Before presenting further results to support this finding, I will discuss the contradiction with previous results and how to resolve this contradiction.

At first there might seem to exist such a weight of evidence for the square-root scaling that it cannot be disagreed with (Equation (1.4)), but this is not the case. We will discuss the two strands of contrary evidence in turn. These are, firstly, results from the soft-disk model, and secondly, experimental data for bidisperse two dimensional foams.

As discussed in Section 1.2.4, the Soft Disk model produces a square-root relationship for $Z(\phi)$. However, the model of interaction used in the Soft Disk model does not represent realistic bubble-bubble interactions. One should, therefore, treat the prediction that two dimensional foams will produce the same square-root relationship in lowest order with some caution.

Experimental evidence of the square-root scaling, as found from measurements of two-dimensional photoelastic disks under compression [22], is in agreement with the prediction of the bubble-model. This is as one might

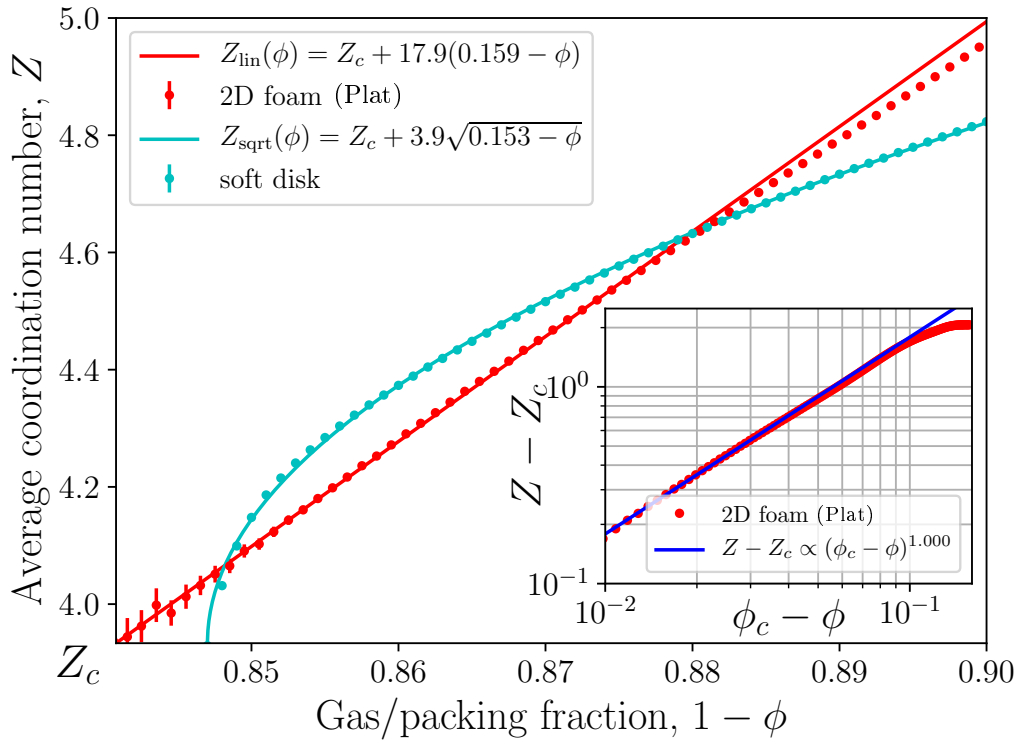

Figure 2.16: For two dimensional foams (Plat) close to the critical liquid fraction, Z was found to vary linearly with $\phi_c - \phi$ (red data points). The average was done over 600,000 independent simulations with 60 bubbles to compare with the Plat results. A linear fit (solid red line) in the displayed range gave a slope of $k_{\mathrm{f}} = 17.9 \pm 0.1$ and a critical liquid fraction of $\phi_c = 0.159 \pm 0.001$. In the wet limit (at ϕ_c), Z_c is given by $Z_c = 4(1 - 1/N)$ due to finite size effects. This results in $Z_c = 3.933$ for $N = 60$ bubbles. For comparison, $Z(\phi)$ is also plotted for a soft disk systems ($N = 60$ with 20,000 simulations), which shows the mentioned square-root scaling. Inset: Double-logarithmic scale for $Z - Z_c$ versus liquid fractions $\phi_c - \phi$ up to $\phi = 0$. By fitting a linear function (solid line), the ϕ_c which gives the best linear relationship is obtained as $\phi_c = 0.159 \pm 0.001$.

expect to be applicable in this case, at least for qualitative purposes.

Let us now turn to the second strand of supposed evidence for the square-root relationship by examining further experimental results which bear directly on two dimensional foams.

Katgert and van Hecke [21] performed experiments with disordered rafts of bidisperse bubbles beneath a glass plate. The distance between plate and liquid surface was varied to obtain foams at different values of liquid fractions. The concept of a liquid fraction is not well defined for such quasi-two dimensional bubble rafts. In particular, in the wet limit where the gap between covering plate and liquid interface is similar to the bubble extension parallel to the plate, the three dimensional nature of the bubbles becomes more relevant. For this reason, Katgert and van Hecke [21] proceeded by imaging their rafts from the top to obtain an area liquid fraction. Based on their analysis, Katgert and van Hecke established $Z - Z_c \propto (\phi - \phi_c)^\alpha$, with exponent $\alpha \simeq 0.70$, Z_c close to 4, and ϕ_c close to 0.84 [21]. Due to the problem in defining a liquid fraction for such a quasi-two dimensional experiment, and in optically identifying contacting bubbles, we do not think that these experimental results can be taken to contradict our Plat findings, even though Katgert and van Hecke describe their wet foams as consisting of "soft frictionless disks".

Our results in two dimensions also suggest that a deviation from the square root scaling in $Z(\phi)$ for three dimensional foams might be observed, since we conjecture that the reason for the deviation in the two dimensional case is the model of interaction. However, the scaling does not have to be linear. Apart from the non-pairwise interaction, the energy for the three dimensional bubble-bubble interaction is also not harmonic. It scales with the form $f^2 \ln(1/f)$, first predicted by Morse and Witten, where f is the force

exerted between droplets (see Chapter 3 for details).

However, similar to the two dimensional case, evidence for the square root scaling in three dimension seems to be very strong at first glance. Experiments from Jorjadze *et al.* [69] with droplet emulsion in three dimensions show a good agreement with the square root increase in $Z(\phi)$. However, as in the experiments of Katgert and van Hecke, the identification of contacting bubbles and the definition of a liquid fraction is not straight forward. Jorjadze *et al.* reconstructed the droplets as overlapping spheres and defined contacts as overlaps. The gas fraction is then the spherical volume reduced by the overlaps which is simply $1-\phi$. Thus, it cannot be ruled out that this procedure contains a bias towards the square root scaling of $Z(\phi)$ as in the Soft Disk model.

The distribution of contacts in a packing can be predicted via the granocentric model [70] which has recently been extended to two dimensional cellular structures [71] and two dimensional packings of discs [72]. However, this model cannot predict the variation of Z with ϕ in packings as it only applies to the wet limit (or jamming point).

2.4.2 Link Between $Z(\phi)$ and the Radial Density Function, $g(r)$

The *radial distribution function*, $R(r)$, is defined as the probability to find a particle a given distance r away from another particle. In two dimensions the *radial density function* is given by $g(r) = \frac{1}{2\pi r}R(r)$, and can be visualised as in Figure 2.17.

For soft disk packings it has been argued that the square root scaling of Z as seen in Relation (1.4) is connected with the variation of the radial density function, $g(r)$. The argument goes that the number of particles within $\Delta\epsilon$ of

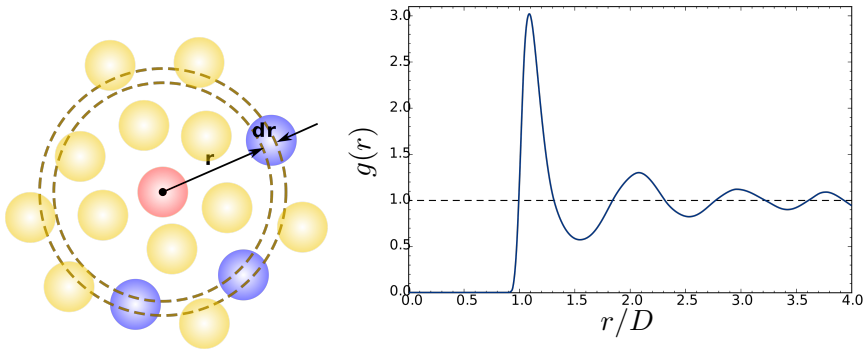

Figure 2.17: The radial density function, $g(r)$, gives the probability of two disk centers being a distance r apart.

touching is equal to the change in Z when compressed by $\Delta\epsilon = (\phi_c - \phi)/(2\phi_c)$

$$\Rightarrow Z(\phi) - Z_c = 2\pi\rho \int_D^{D+\Delta\epsilon} g(r) r \mathrm{d}r, \tag{2.12}$$

i.e. the integral of $g(r)$ over a circular shell is equal to $Z(\phi)$ [14, 23, 73], although the validity of this argument is still under discussion [74].

From simulations of three dimensional monodisperse soft spheres with diameter $D = 1$ close to the jamming transition, the behaviour of $g(r)$ is found to be divergent according to the power law

$$g(r) = \frac{c_\mathrm{d}}{\sqrt{r-1}}, \tag{2.13}$$

where c_d is a constant [23].

A similar divergence can be found in two dimensional polydisperse systems, when the radial density function is rescaled to $g(\xi)$ with the rescaled interparticle distance $\xi = r/(R_i + R_j)$, where R_i and R_j are the radii of two disks with distance r apart [14]. Assuming that the systems deforms in an affine way (see Equation (2.14)), integrating $g(r)$ over r then results in the square root scaling for $Z(\phi)$ of Relation (1.4) [14, 23, 73].

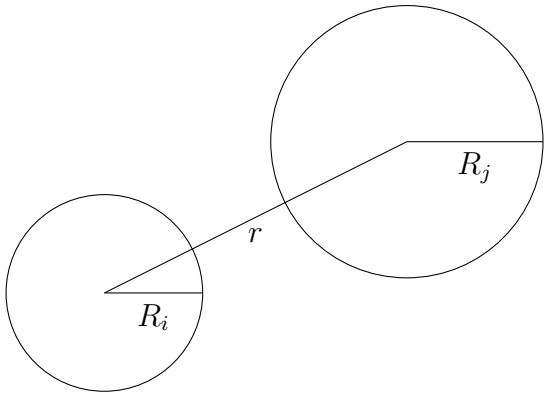

Figure 2.18: Interpartical distance measurements for calculating $g(r)$. The rescaled interparticle distance is $\xi = r/(R_i + R_j)$.

2.4.3 Linking the Radial Density Function to the Distribution of Separations, $f(w)$

For two dimensional foams, such an argument involving $g(\xi)$ is not straightforward to develop, since bubbles are deformable and only have well-defined centres in the wet limit (at ϕ_c) where they are circular. For this reason we will consider a different approach, which involves a distribution of separations, $f(w)$, between bubbles (or disks), as in the work of Siemens and van Hecke [75]. Here, the separation w is the shortest distance between two bubble arcs/disk edges (see Fig 2.19). For the soft disk system, this separation is then related to their distance by their radii, $r = w + R_i + R_j$. Therefore $w = r - D$ (D being the average disk diameter), so $f(w)$ is identical to $g(r)$ close to the divergence, when shifted by the average disk diameter D. Thus $g(r - D) = f(w)$ and $g(\xi - 1) = f(w/D)$.

Let us now consider the compression of a two dimensional, polydisperse foam/disk sample of initial liquid fraction ϕ_c to a final value of $\phi < \phi_c$. The fractional compression, $\Delta\epsilon$, is given by $\Delta\epsilon = (\phi_c - \phi)/(2\phi_c)$, and is considered to be infinitesimally small.

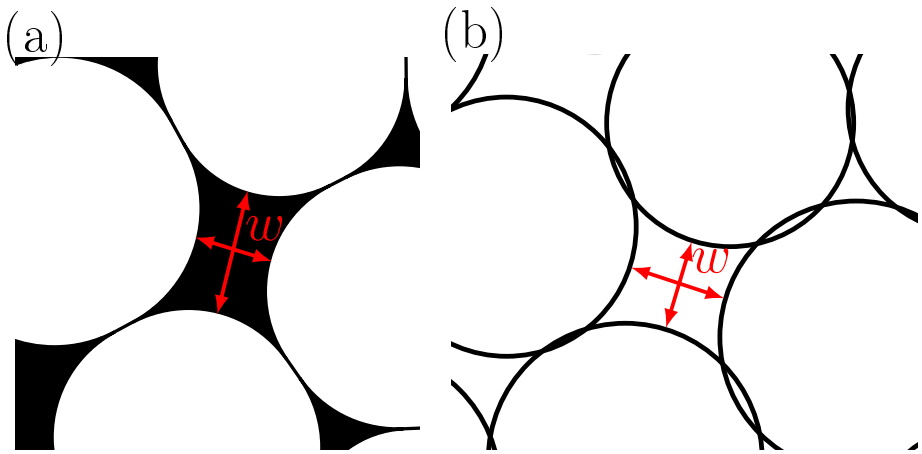

Figure 2.19: An Illustration of the separation, w, between (a) bubbles and (b) soft disks. The separation is defined as the shortest distance between two bubble arcs/disk edges. Its distribution $f(w)$ is connected to $Z - Z_c$ via an integration (see Equation (2.14)) [14, 23].

We can estimate $Z(\phi)$ for the case of an *affine compression* from $f(w)$. An affine compression is one where the whole system compresses smoothly without any internal changes, i.e. the internal compressions between bubbles are proportional to the external compression of the system. In this case the deformation of the sample will lead to an increase in coordination number due to bubbles coming together that initially, i.e. in the wet limit (at ϕ_c), were closest to each other. For an affine deformation, the fractional compression can be expressed as $\Delta\epsilon \approx \Delta w/D$. Thus, the average number of contacts in two dimensions can be estimated by integrating $\rho f(w/D)$ over a radial shell up to $D\Delta\epsilon$, and Equation (2.12) becomes

$$\begin{aligned} Z(\phi) - Z_c &= 2\pi\rho \int_0^{\Delta\epsilon} \mathrm{d}w f(w)(D+w) \\ \Rightarrow Z(\phi) - Z_c &= 2\pi\rho \int_0^{D\Delta\epsilon} \mathrm{d}w f(w)(1+w/D), \end{aligned} \tag{2.14}$$

where $\rho = 4\phi_c/(\pi D^2)$ is the particle number density (number of bubbles per

unit volume).

2.5 Distribution of Separations, $f(w)$, for Two Dimensional Foams and Soft Disk Systems

Figure 2.20 shows the distribution, $f(w)$, for both foams and packings of soft disks with the same system size ($N = 60$) and area polydispersity. The difference between our results for simulated two dimensional foams and two dimensional disk packings is striking. Whereas in the case of disks, $f(w)$ diverges in the limit

$$w/D \to 0 \quad \text{as} \quad f(w) = \frac{c_\mathrm{d}}{\sqrt{w/D}} \tag{2.15}$$

as expected from the divergence of $g(\xi)$ with $c_\mathrm{d} = 0.25 \pm 0.01$, for the two dimensional foams a finite limiting value $c_\mathrm{f} = 2.9 \pm 0.7$ is reached in this limit. Only at values of $w/D \gtrsim 10^{-2}$, $f(w)$ is the same for both foams and soft disks; see Figure 2.20.

The variation of $Z(\phi)$ was shown to be consistent with the distribution of separations $f(w)$ for the two dimensional foam, which is connected to $Z - Z_c$ via the integration shown in Section 2.4.3. When inserting the power law expression from Equation (2.15) that we obtained for the soft disk simulation into Equation (2.14), we get

$$\begin{aligned} Z(\phi) - Z_c =& 2\pi\rho \int_0^{D\Delta\epsilon} \mathrm{d}w \frac{1}{\sqrt{w/D}}(1 + w/D) \\ =& \sqrt{128\phi_c} c_\mathrm{d} \sqrt{\phi - \phi_c} + \mathcal{O}\left(\sqrt{\phi - \phi_c}^3\right) \\ \approx& (2.6 \pm 0.1)\sqrt{\phi - \phi_c}\,, \end{aligned} \tag{2.16}$$

where we neglected terms of higher order. For ϕ_c, the value 0.841 ± 0.002 was used [34].

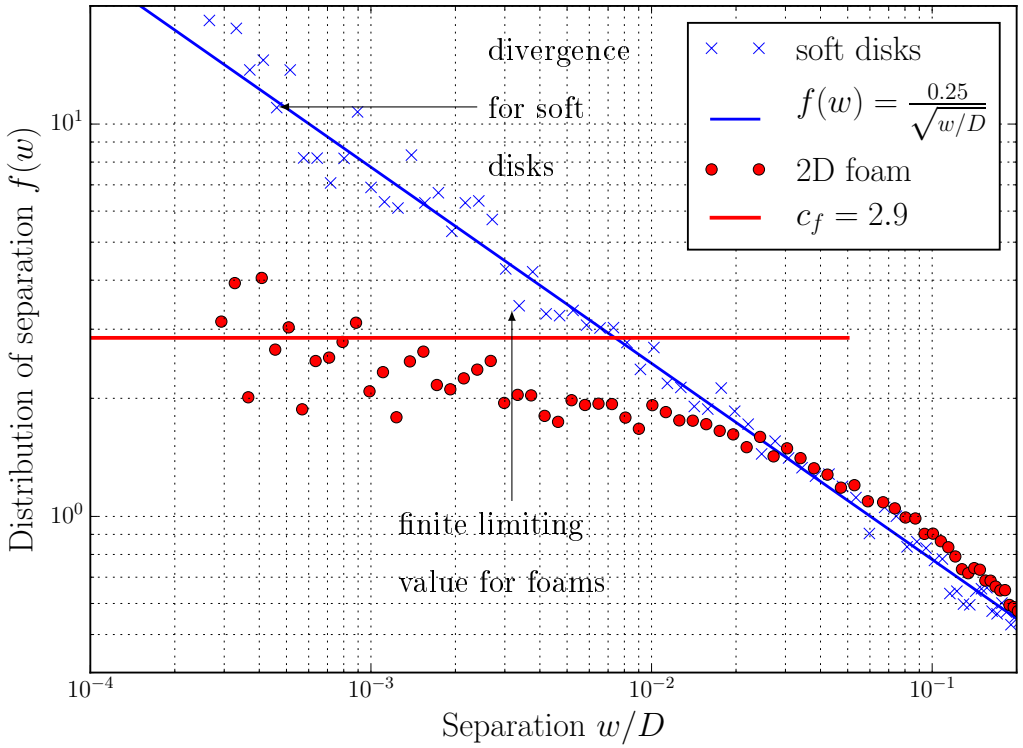

Figure 2.20: Distribution of separations, $f(w)$, for two dimensional foam (red circles) and two dimensional disk packing (blue crosses) at a similar average coordination number $Z_{\mathrm{SD}} = 4.07 \pm 0.01$ for soft disks and $Z_{\mathrm{foam}} = 4.06 \pm 0.01$ for the two dimensional foam. The data shown presents averages obtained from 1379 packings, each containing 60 bubbles or disks. In the case of foams, the finite value at $f(w)$ in the limit of $w/D \to 0$ is consistent with the observed linear increase of the average coordination number Z, according to the approximate argument, given in Section 2.5. The decay of $f(w) \propto (w/D)^{-1/2}$ in the same limit as in the case of the disk packings is consistent with the square root increase of Z.

Fitting the soft disk data for $N = 60$ to a square root function, $Z - Z_c = k_d\sqrt{\phi - \phi_c}$ for all $Z < 4$ gives $k_d = 3.86 \pm 0.01$ and $\phi_c = 0.847 \pm 0.001$.

For the two dimensional foam simulation, the finite limiting value, c_f, can be inserted for $f(w)$ in the limit $w/D \to 0$ in Equation (2.14). By integrating, we then obtain for $Z(\phi)$

$$\begin{aligned} Z(\phi) - Z_c &= 2\pi\rho \int_0^{D\Delta\epsilon} \mathrm{d}w c_f(1 + w/D) \\ &= 4\ c_\mathrm{f}(\phi - \phi_c) + \mathcal{O}\left((\phi - \phi_c)^2\right) \\ &\approx (11.6 \pm 2.8)(\phi - \phi_c)\,. \end{aligned} \tag{2.17}$$

Again, we neglected terms of higher order.

Qualitatively both estimations agree with expectations, although the apparent difference in the prefactor remains to be resolved. In both cases, the prefactors are underestimated when obtained from our data for soft disk/bubble separations.

	$\lim_{w\to 0} f(w)$	$Z(\phi) - Z_c$	
		Computed via $f(w)$	Direct calculation
2D foam:	2.9 ± 0.7	$(12 \pm 3)(\phi - \phi_c)$	$(18.1 \pm 0.1)(\phi - \phi_c)$
soft disks:	$\frac{0.25\pm0.01}{\sqrt{w/D}}$	$(2.6 \pm 0.1)\sqrt{\phi - \phi_c}$	$(3.86 \pm 0.01)\sqrt{\phi - \phi_c}$

Table 2.1: A summary of our results for two dimensional foams and soft disks. An estimation of variation of $Z(\phi)$ results in the expected power-law relation, but an underestimation of the expected prefactor. Differences in the distribution of separation $f(w)$, and the estimated and directly measured average coordination number $Z(\phi)$, for two dimensional foam and soft disk simulation in the wet limit were found.

Table 2.1 summarises all results that we found to differ in two dimensional foams and soft disks. It demonstrates that the linear variation of Z close to ϕ_c

is consistent with the distribution of separation found in wet foams. However, this is still short of a full explanation of the asymptotic properties of the wet limit.

2.6 Conclusions

A detailed study of the statistics of two dimensional foams at equilibrium has been presented here, spanning the entire range of liquid fraction from the dry to the wet limit. This was based on extensive computer simulations using the Plat software that were not practical when Plat was developed in the early 1990s. The reconstituted program still has difficulty in coping with the wet limit, which should be addressed in future. However, we have succeeded in calculating the excess energy of foams, the coordination number, the distribution of cell sides, and the number of rearrangements over the full range of liquid fraction.

An alternative approach to simulate wet foams with the Surface Evolver software [37] is associated with different complications. As it stands this software uses finite contact angles and it has been shown by Cox *et al.* [45] that this largely suppresses the large scale rearrangements analysed here.

In addition to providing further possibilities for analysing properties of two dimensional foams, we hope that our numerical results stimulate new experiments. These may be realised in a variety of ways, see Section 1.1 for examples. Although a two dimensional liquid fraction is not well defined in any of those cases, such experiments should give an indication whether large scale rearrangements occur on small increases of liquid fraction in the wet limit, and increase in the manner suggested here.

The variation of Z as a function of liquid fraction was one of the first

problems that was tentatively addressed with the Plat software, as soon as it was developed in the early 1990s. The very limited data sets available at the time ($\phi \leq 0.125$, 100 cells [33], 530 cells [76]) showed that a linear extrapolation of the data leads to $Z = 4$ at $\phi_c \simeq 0.16$ [55]. However, even though later simulations using a lattice gas model for foams also showed a linear variation of Z very close to ϕ_c, this data was based on an even smaller sample of only 30 bubbles [77].

The success of Durian's bubble model [34, 57] in reproducing the Herschel−Bulkley type rheology that is associated with emulsions and foams [24], and its ease in simulating packings of 10,000 or more bubbles, led to it being treated as the most efficient model for simulations of two dimensional foams in general. Thus, its square-root variation of Z with liquid fraction away from ϕ_c was also expected to hold for two dimensional foams. Here I have shown, based on a large amount of new data, that this is not the case. For two dimensional foams we find that the average coordination number varies linearly in this limit. The reason for this differing behaviour must ultimately lie in the different contributions that disk or bubble contacts make to the total energy of the packing. In a foam the energy per bubble per contact increases with the number of contacts [46]. Energy minimisation might thus favour a reduction in the number of contacts in the wet limit of foams, compared to disk packings.

In summary, I have shown that the disordered structure of a polydisperse two dimensional foam is significantly different compared to a soft disk packing with the same polydispersity as evidenced by the different $Z(\phi)$ and corresponding distribution of separations. This is most likely due to the fact that bubble-bubble interactions are much more complicated than the simple pairwise interaction used in the Soft Disk model While this study only

focussed on a two dimensional foam system, similar deviations are likely for other two dimensional jammed systems with soft, deformable particles. The relevance to three dimensional packings of soft particles, such as emulsions, biological cells [78, 79], and microgel particles [80] remains to be examined.

In order to further investigate the influence of the deformability of bubbles on the properties of foams a new model is required. In this new model, the interactions of one bubble with all of its neighbours will be coupled via the conservation of area. In the following chapter I will show how we can use the work of Morse and Witten in three dimensions to derive such a model for two dimensions. I will also give an implementation of this model for simulating a two dimensional foam, and some preliminary results from these simulations.

Chapter 3

Simulating Two Dimensional Foams Using Morse–Witten Model of Bubble Deformation

In 1993, Morse and Witten published a paper entitled "Droplet Elasticity in Weakly Compressed Emulsions" [48]. In it, the authors describe, in unfortunately brief terms, a process by which they derive a first order theory for the deformation of a droplet under low compression. Additionally, and very importantly for us, the paper establishes a way to include the effects of all neighbours in bubble−bubble interactions. That is to say, we can now describe how a bubble's response to a contact is changed by additional contacts around the bubble. This arises from the inclusion of volume conservation in the model, a feature lacking from the Soft Disk model. Morse and Witten used this to produce an expression for the deformation energy of a monodisperse three dimensional emulsion with small deformations. They found that it scales logarithmically with contact force. This in itself is not intuitive or obvious in any way, and so is an interesting result. Unfortunately,

this work has seen very little follow-up until recently, due in part no doubt to the sophisticated and highly compressed nature of the original work.

Buzza and Cates [81] calculated the elastic modulus of three dimensional droplets on a simple cubic lattice under uniaxial strain using two different models. Using a simple truncated sphere approximation, they found a sharp cut−off discontinuity in the elastic modulus at the wet limit. Using a model based on the theory of Morse and Witten, they found it to goes to zero smoothly as $1/\ln(\phi_c - \phi)$ as the wet limit is approached. $\phi_c - \phi$ is a measure of how far the system is from the wet limit. Experimentally they measured a linear dependence of the elastic modulus on $\phi_c - \phi$. Therefore, they concluded that the experimental data could not be explained in terms of a model of droplets on a monodisperse simple cubic lattice. They suggest that it is the disorder in the experimental systems that is responsible for the linear behaviour. Thus, it is important to be able to model disorded, polydisperse systems.

Höhler and Cohen-Addad [82] compared the calculation of several physical properties of crystalline bubble arrangements close to the wet limit using different interaction models. Primarily they compared a two-body interaction law of the type used in the Soft Disk model (Section 1.4.2) with a many-body law derived from the Morse−Witten theory; a Surface Evolver calculation provided a baseline. They found that, for properties such as the uniaxial elastic modulus, the many-body interaction agreed with the Surface Evolver calculation over a range of values of ϕ, but the two-body law did not. They also found that they could largely reproduce the results of the many-body law using a two-body law that included a logarithmic term in the limit where the contact force goes to zero. The critical scaling of a logarithmic interaction cannot be approximated by a power law, see Figure 3.1. The two-body law

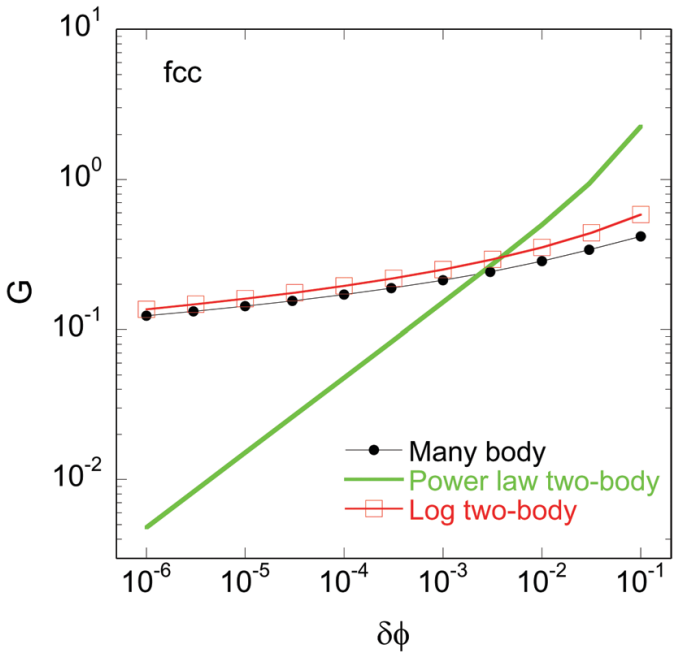

Figure 3.1: Shear modulus, G, versus excess packing fraction, $\delta\phi$, reproduced from [82]. This shows the agreement between the many-body law and the two body law with a logarithmic term in contrast with the power law(Equation (3.1)), which cannot approximate a logarithmic interaction.

used was of the form

$$f(\delta R) = \kappa(z)\alpha(z)\frac{((1+\delta R)^{-3}-1)^{\alpha(z)-1}}{(1+\delta R)^4}, \tag{3.1}$$

where δR is the contact deformation, and $\kappa(z)$ and $\alpha(z)$ are fitted functions that depend only on the coordination number. In general, they found that the deformation of a bubble or droplet at a given contact depends on the entire set of forces a bubble experiences due to all its neighbours. The model based on the theory of Morse and Witten reproduced this behavior quantitatively without any free parameters, validating the Morse−Witten model.

In the following section, I will attempt to present the derivation of the Morse−Witten theory in a clearer fashion for foams. I will show how the

case of multiple contacts of bubbles differs from the single contact case. I will then apply this concept to the simulation of a disordered, polydisperse, two dimensional foam.

In Chapter 4, I will show a different application of the three dimensional Morse−Witten theory. It can be used to derive a simple formula for the determination of the surface tension of a drop of liquid [3]. This formula uses two length measurements and contains no free parameters. We compare this with exact calculations of the solution of the Young−Laplace equation and find it exact in the limit of small deformation.

3.1 Morse–Witten Theory

3.1.1 A Summary of the Derivation of the Morse–Witten Theory in Three Dimensions

The original paper by Morse and Witten, and much of the subsequent work mentioned above, has been recently reviewed by Weaire and Höhler [47]. I will summarise their explanation of Morse and Witten's derivation without delving into the detailed mathematics. This is followed by an explanation of Weaire *et al.*'s [83] corresponding derivation in two dimensions with equal sized bubbles. To this I add my generalisation of the capping method which accounts for the contacting bubbles being of different sizes. This I further generalise to the case of multiple contacts per bubble (in Section 3.1.5), from which I formulate a two dimensional Morse−Witten foam model (Section 3.2). I then develop an algorithm to find equilibrium configurations of Morse−Witten foams (Section 3.3), implement this in a simulation, and test it against Plat (Section 3.4). I conclude with some preliminary results

from these simulations, and a discussion about extending the model to three dimensions.

The initial problem is "What shape does a single bubble take when pressed against a flat plate by buoyancy?" Equivalently, as Morse and Witten did, one can consider a droplet under gravity, the difference is merely one of orientation. This problem has rotational symmetry about the axis between the centre of contact with the plate and the centre of mass of the bubble. We will call this the z direction and consider a cross sectional profile vertically through the bubble. The surface of the bubble will be described in terms of a radial coordinate, $\rho(\theta)$, and a polar angle, θ. The cross-sectional profile is given by

$$\rho(\theta) = R_0 + \delta R(\theta), \tag{3.2}$$

where R_0 is the radius of the undeformed bubble and $\delta R(\theta)$ is the deformation in polar coordinates (see Figure 3.2).

The equation that describes the shape of this profile is the Young−Laplace equation (Equation (1.6)), which relates the curvature of the surface to the difference in pressure across the bubble surface. The pressure difference ΔP can be split up into the constant pressure difference between the internal and external pressures at $z = 0$, and the pressure gradient due to hydrostatics $\Delta\rho g z$, where $\Delta\rho$ is the density difference between the inside and the outside of the bubble and g is the usual acceleration due to gravity. The constant pressure difference itself can be further split into ΔP_0, a constant pressure offset to be determined by volume conservation, and $2\gamma/R_0$, the Laplace pressure of the undeformed bubble. This leaves us with

$$\Delta P = \Delta P_0 + \frac{2\gamma}{R_0} + \Delta\rho g z. \tag{3.3}$$

The total curvature is expressed in terms of the change in the profile, $\delta R(\theta)$

giving

$$\frac{2}{r} = \frac{(\delta R+1)\left(-(\delta R+1)\delta R'' + 3\delta R'^2 + 2\delta R^2 + 4\delta R + 2\right) - \cot(\theta)\delta R'(\delta R'^2 + (\delta R+1)^2)}{2(\delta R+1)(R'^2 + (\delta R+1)^2)^{3/2}}, \tag{3.4}$$

and this is linearised in the deformation δR to give

$$\frac{2}{r} = -\left(2 + \cot\theta\frac{\partial}{\partial\theta} + \frac{\partial^2}{\partial\theta^2}\right)\frac{\delta R(\theta)}{R_0^2} + \frac{2}{R_0}. \tag{3.5}$$

Substituting Equation (3.5) and Equation (3.3) into Equation (1.6) we get

$$-\gamma\left(2 + \cot\theta\frac{\partial}{\partial\theta} + \frac{\partial^2}{\partial\theta^2}\right)\frac{\delta R(\theta)}{R_0^2} = \Delta P_0 + \Delta\rho g R_0\cos\theta, \tag{3.6}$$

where we have used the approximation $z = R_0\cos(\theta)$ and subtracted the common Laplace pressure from both sides. The approximation is valid in systems where surface tension dominates, i.e. $\gamma \gg \Delta\rho g R_0^2$. By applying the constraints of surface smoothness at $\theta = \pi$, volume conservation, and that the centroid of the bubble coincides with the origin, this is solved by

$$\frac{\delta R(\theta)}{R_0} = \frac{-FG(\theta)}{\gamma R_0} \tag{3.7}$$

where

$$G(\theta) = -\frac{1}{4\pi}\left\{\frac{1}{2} + \frac{4}{3}\cos\theta + \cos\theta\ln\left[\sin^2(\theta/2)\right]\right\} \tag{3.8}$$

and $F = 4\pi\Delta\rho g R_0^3/3$ is the total buoyancy force exerted by the bubble on the plate. This concludes the explanation of Morse and Witten's derivation.

A polar plot of this solution is given in Figure 3.2. The left shows the full profile as given by the Morse−Witten theory. Note that, due to the logarithmic term in Equation (3.8), there is a divergence in the profile at the point of contact. In the left of Figure 3.2 this is highlighted in red. This is perfectly acceptable as that component of the profile is actually unused. If we consider a contact between a bubble and a hydrophobic plate, the bubble surface is tangent to the plate at the meeting point. Therefore, the bubble

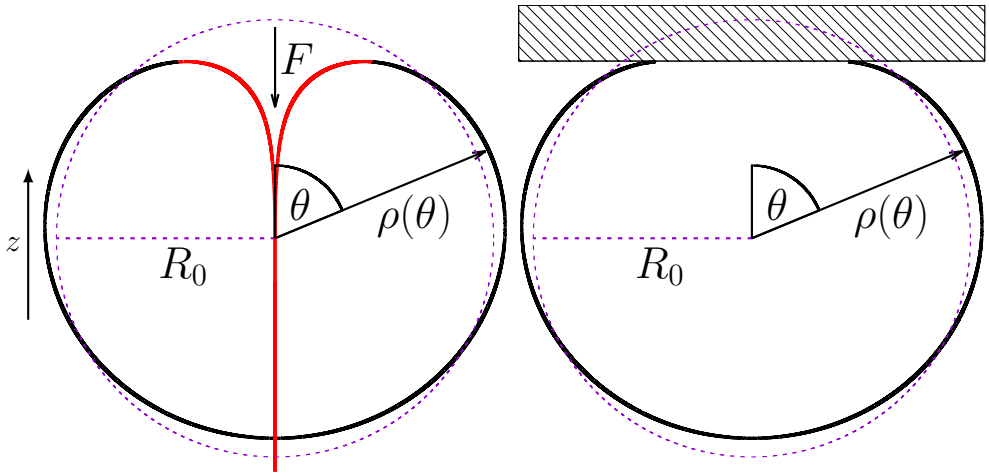

Figure 3.2: Profile of the solution to the linearised Young–Laplace equation according to Morse and Witten representing a cross-section of a three dimensional bubble with volume $4/3\pi R_0^3$ pressed against a plate by buoyancy. The undeformed bubble is indicated in dashed blue. θ is the radial coordinate and $\theta = 0$ at the center of the point of contact. Note the unphysical divergence of the profile in the vicinity of the contact, highlighted in red (left). If we consider a bubble in contact with a plate (right), the section of the profile outside the contact region is used, and we neglect the divergent piece inside the contact region.

profile is simply truncated at the point where its slope is equal to the slope of the plate as in Figure 3.2 (right), where this slope is zero and the profile is capped by a flat disk at the contact. This has the effect of including the small additional volume between the bubble and the cap as part of the bubble. This additional volume is of order f^2, and thus can be neglected in this theory. For contact angles increased from zero the point of contact between the two bubbles moves closer to the center of the contact. This reduces the amount of volume neglected in this approach.

3.1.2 A Summary of the Derivation of the Morse–Witten Theory in Two Dimensions

Now we wish to carry out an analogous derivation in two dimensions. The profile this will give us will form the basis for the new model of two dimensional foams we wish to create. This was not carried out by Morse and Witten in their original paper, but it has been done by Weaire *et al.* [83] and proceeds as follows.

The pressure difference in two dimensions is given by

$$\Delta P = \Delta P_0 + \frac{\gamma}{R_0} + \Delta\rho g z. \tag{3.9}$$

(In two dimensions the Laplace pressure has no factor of 2 as there is only one principal curvature). The linearised curvature expression is

$$\frac{1}{r} = -\left(1 + \frac{\partial^2}{\partial\theta^2}\right)\frac{\delta R(\theta)}{R_0^2} + \frac{1}{R_0}. \tag{3.10}$$

Combining these with the Young–Laplace equation in two dimensions, the equation to be solved for the change in the profile becomes Substituting Equation (3.10) and Equation (3.9) into Equation (1.8) ($\Delta p = \gamma/r$) we get

$$-\gamma\left(1 + \frac{\partial^2}{\partial\theta^2}\right)\frac{\delta R(\theta)}{R_0^2} = P_0 + \Delta\rho g R_0\cos\theta \tag{3.11}$$

where P_0 is a constant pressure offset to be determined from area conservation. Again, we have used the approximation $z = R_0\cos(\theta)$ and subtracted the common Laplace pressure from both sides. The solution is of the form

$$\delta R(\theta) = -\frac{R_0 F}{2\gamma\pi}G(\theta), \tag{3.12}$$

with

$$G(\theta) = (\theta - \pi)\sin(\theta) + \frac{\cos(\theta)}{2} + 1, \tag{3.13}$$

and $F = \pi R_0^2 \Delta\rho g$, the buoyancy force in two dimensions. In general, the force experienced by a bubble does not have to be a buoyancy force. The natural normalisation in two dimensions is therefore the surface tension, γ, rather than the buoyancy, and the normalised force is $f = F/\gamma$. (In three dimensions the surface tension does not have the dimensions of a force, so we use γR_0 instead, which does have the required dimensions).

Equations (3.13) represents the deformation of the bubble in such a way that its centroid (or centre of mass), which represents its location, is kept fixed. The polar angle, θ, is measured from the contact with the flat plate (or equivalently, identical neighbour, see Figure 3.3). Note that there is no logarithmic term in the two dimensional profile, hence the profile does not diverge at the point of contact. There is still a kink, a discontinuity in the slope at the point of contact. The distance from the centroid to the kink is simply $\rho(0) = R_0\left[1 - (3F)/(4\pi\gamma)\right]$. In the case of a point force, this is correct. It can be adapted, as in the three dimensional case, by the introduction of a flat "cap" at the contact, see Figure 3.3. In this case, only the profile outside the cap area is used. This has the effect of including the small additional area between the bubble and the cap as part of the bubble. This additional are is of order f^3, and thus can be neglected in this theory.

The point where the profile is ended and the cap begins can be found quite readily. Since the orientation is arbitrary, we choose one such that the direction of gravity is perpendicular to the contact cap. Then, the slope of the cap is zero as in Figure 3.3. The slope is defined as

$$s(\theta) = \frac{\frac{\partial}{\partial\theta}\left[\rho(\theta)\cos(\theta)\right]}{\frac{\partial}{\partial\theta}\left[\rho(\theta)\sin(\theta)\right]}. \tag{3.14}$$

Performing the differentiation we get

$$s(\theta) = \frac{2[(F - 2\pi\gamma)\sin(\theta) + F(\pi - \theta)\cos(2\theta)]}{\cos(\theta)[4\pi\gamma + 4F(\pi - \theta)\sin(\theta) - 2F] - F}. \tag{3.15}$$

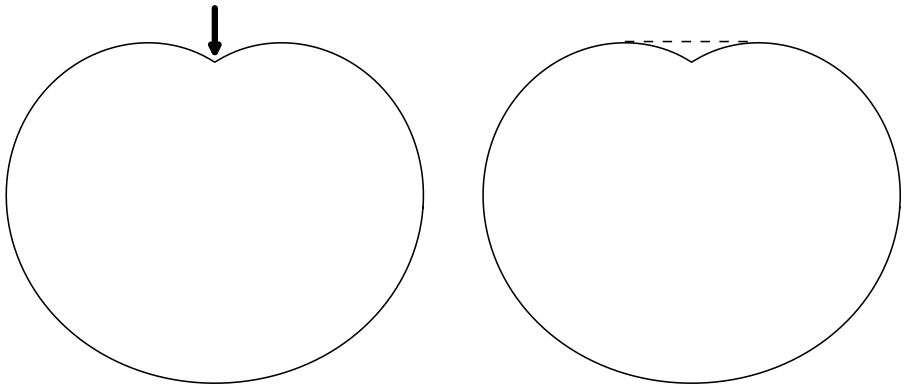

(a) **(b)**

Figure 3.3: The shape of the two dimensional Morse−Witten profile given by Equation (3.13). (a) The profile $\rho(\theta)$ of a two dimensional bubble under the action of a point force $f = F/\gamma$. (b) Illustration of the capping of the profile to represent a flat contact. In the simple case of a contact with a wall or an identical bubble the cap meets the profile where the slope of the profile equals the slope of the cap (zero in this case). Note that, in contrast with the three dimensional case (Figure 3.2), there is no logarithmic divergence in two dimensions.

Expanding this to first order in the angle θ this reduces to

$$s(\theta) = -\frac{2\pi(F - 2\gamma\theta)}{4\pi\gamma + F(4\pi\theta - 3)}, \tag{3.16}$$

and further expanding to the first order in the contact force F it further reduces to

$$s(\theta) = \frac{F}{2\gamma} - \left(1 + \frac{3F}{4\pi\gamma}\right)\theta. \tag{3.17}$$

Setting $s(\theta_0) = 0$, we get the polar angle at which the profile is truncated

$$\theta_0 = \frac{2\pi F}{3F + 4\pi\gamma}. \tag{3.18}$$

The distance from the centroid to the cap is then $\rho(\theta_0)\cos(\theta_0)$, which, to

second order in the force, is

$$R_0 + \delta R(\theta_0) = R_0 \left(1 - \frac{3F}{4\pi\gamma} + \frac{F^2}{8\gamma^2}\right). \tag{3.19}$$

By comparing this with $\rho(0)$, we can see that the correction term is simply $R_0F^2/(8\gamma^2)$, the second order term in Equation (3.19). This means that the correction that would have to be introduced in order to maintain area conservation is of order F^3, and thus negligible in this theory.

3.1.3 Modelling an Ordered Assembly of Equal Sized Bubbles

At this stage, we have almost all of the components required to model a monodisperse ordered foam, we just need to examine the case of multiple contacts. We will make use of the fact that Equation (3.13) is the solution of a linearised differential equation, and thus a linear combination of solutions is also a solution.

This setup will no longer involve gravity, and so will not contain a buoyancy force. However, the pressure gradient in Section 3.1.2, that was due to buoyancy, is still valid. It is now simply provided by a fictitious body force at each contact that is equal and opposite to the contact force. Since the contact forces are in mechanical equilibrium, so are their corresponding body forces. The result is that the net fictitious force is zero in mechanical equilibrium.

By symmetry, every contact is deformed equally, and the contact forces are equal. The deformation at contact i is given by the following sum over all contacts j that a bubble has

$$\delta R_i = -\frac{R_0}{2\gamma\pi} \sum_j FG(\Delta\theta_{ij}), \tag{3.20}$$

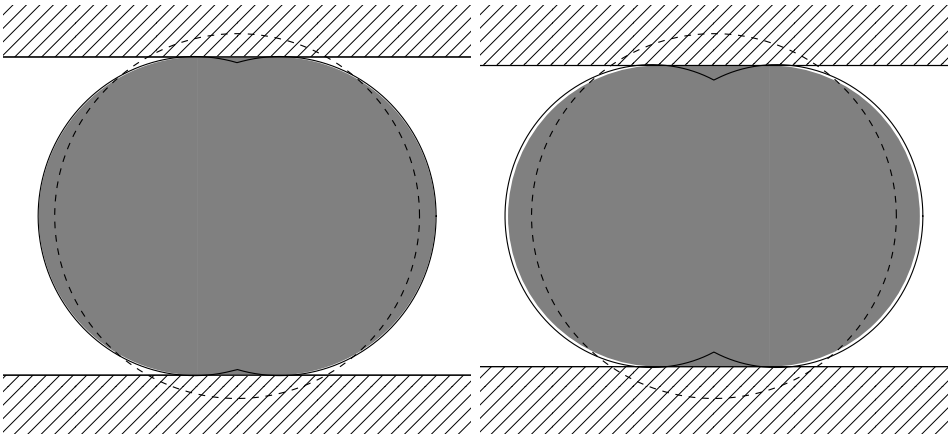

Figure 3.4: The shape of a two dimensional bubble trapped between two parallel lines (grey area). In the Morse−Witten model (solid line) this is represented as two opposing contacts of equal magnitude (left: $f = 0.5$, right: $f = 0.8$). Note that the solid line is not the boundary of the grey area, that it appears this way just indicates the close agreement between the analytic case and the Morse−Witten approximation. The dashed line shows the undeformed bubble of radius R_0. The deformation of each contact is approximately 13% relative to R_0.

where $\Delta\theta_{ij}$ is the angle between the line from the centre of the bubble to contact i and the line from the centre of the bubble to contact j.

Including the correction from Equation (3.19), this becomes

$$\delta R_i = -\frac{R_0}{2\gamma\pi}\sum_j FG(\Delta\theta_{ij}) + \frac{R_0F^2}{8\gamma^2}. \tag{3.21}$$

In the case of Z contacts per bubble, with angles of $\Delta\theta = 2\pi/Z$ between each contact, the sum can be calculated analytically. Weaire *et al.* [83] showed this to be

$$\delta R = \frac{\pi R_0}{6Z\gamma}F + \frac{R_0F^2}{8\gamma^2}. \tag{3.22}$$

The case of two opposite contacts, representing a bubble trapped between two parallel lines, can be easily tested. In this case the shape of a bubble,

according to the Young−Laplace law, is two semicircles separated by a rectangle. Figure 3.4 illustrates this test for normalised contact forces $f = 0.5$ and $f = 0.8$, giving a relative deformation ($\delta R/R_0$) of approximately 13% and 17% respectively. Here, the exact solution is shown as the grey area and the Morse−Witten model is the solid line, while the undeformed bubble is the dashed circle. The close agreement of the two for $f = 0.5$ is remarkable, given that the theory is derived in the wet limit (low deformation, low force) and mostly first order in the force. At the larger force of $f = 0.8$ the differences between the two becomes more apparent.

3.1.4 Contact Between Two Bubbles of Different Sizes

Next I will provide a generalisation of the capping method to account for contacts between bubbles of different sizes. In this case, the ideal cap on the bubble profiles, the shared contact line, is now curved due to a pressure difference between the bubbles. Therefore, the point of contact between the two bubbles is shifted inside the dimple of the larger bubble and outside the dimple of the smaller bubble. This is where the slopes of the profiles of the two bubbles are equal in magnitude and opposite in direction. We will not worry about the curved nature of the contact line, but we need to find the relationship between the point where the profiles contact and the magnitude of the contact force.

We require then to find the relationship between the contact force and the deformation of each bubble, represented by x_i, i.e the distance along the centre−centre line from the undeformed bubble to the contact point (see the inset of Figure 3.5). To lowest order, x_i is the distance that the point at the cusp of the contact is displaced, which is $-\delta R_1(0) = 3R_1 f/4\pi$ from Equation (3.13). This is indicated in red in the inset of Figure 3.5. However,

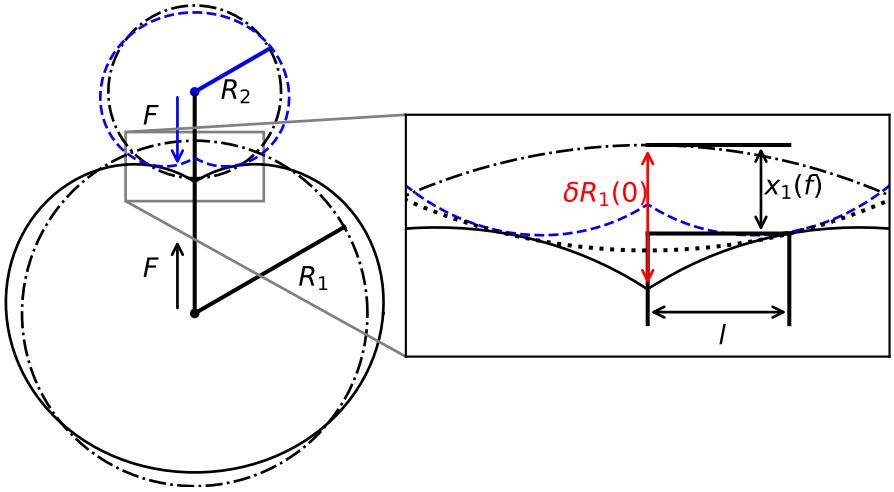

Figure 3.5: Two different sized two dimensional bubbles held in contact with each other by opposed body forces F, as calculated using Equations (3.2) and (3.13). Their undeformed circular forms, with radii R_1 and R_2, are again illustrated by the dashed lines. Here we have used a large force for illustrative purposes; the theory is not accurate for deformations as large as this. Note the corrected deformation of bubble 1 at the point of contact is indicated by $x_1(f)$, and calculated with Equation (3.26).

this overestimates the deformation at the contact and would cause contacting bubbles to overlap incorrectly. Instead we would like to know the distance by which the cap is displaced, rather than the cusp of the profile.

A simple derivation of the required relation between F and x_i follows. As with many other aspects of the theory, this deals with lowest-order expressions only, and can therefore be developed easily by using these approximations from the beginning. Thus, we can take the force between two bubbles, to lowest order to be

$$F = 2lp_0, \tag{3.23}$$

where $2l$ is the width of the contact (Figure 3.5) and p_0 is the mean of the

two (lowest order) bubble pressures $p_i = \gamma/R_i$. This is because, to lowest order, the contact between two bubbles is flat. Hence

$$F = \theta_i R_i \gamma \left(\frac{R_1 + R_2}{R_1 R_2} \right), \tag{3.24}$$

where $2\theta_i$ is the opening angle of the contact. We can also express x_i in terms of θ_i, as

$$x_i = R_i - \cos(\theta_i)\rho(\theta_i) \simeq -\delta R_i(\theta_i) \tag{3.25}$$

This improved expression for the deformation of bubble i (= 1 or 2) is then expanded as a polynomial to $\mathcal{O}(f^2)$ to give

$$x_i(f) = \frac{3fR_i}{4\pi} - \frac{f^2 R_i}{2(2 + R_1/R_2 + R_2/R_1)}, \tag{3.26}$$

which is indicated in the inset of Figure 3.5. The relative deformation, x_i/R_i, is the same for each of the two bubbles. The centre−centre distance Δ_{12} is then given by

$$\Delta_{12} = (R_1 - x_1(f)) + (R_2 - x_2(f)). \tag{3.27}$$

For two bubbles with radii $R_1 = R_0 + \Delta R$ and $R_2 = R_0 - \Delta R$, this results in the dimensionless change in separation as

$$1 - \frac{\Delta_{12}}{2R_0} = \frac{x_1(f) + x_2(f)}{2R_0} = \frac{3f}{4\pi} - \frac{f^2}{8}\left[1 - \left(\frac{\Delta R}{R_0}\right)^2\right]. \tag{3.28}$$

Since the term linear in f has no ΔR in it, terms of order f^2 or higher need to be considered in the expansion of Equation (3.25) to account for polydispersity. This is in contrast to the situation in three dimensions, see Section 3.4.1. (Note that, in the monodisperse case, i.e. $\Delta R = 0$, the correction term in Equation (3.28) reduces to $f^2/8$, not to $f^2/4$, as wrongly stated in the appendix of Weaire *et al.* [83]. This had no consequences for the results presented in that paper.) In the other extreme, when $\Delta R = R_0$, i.e.

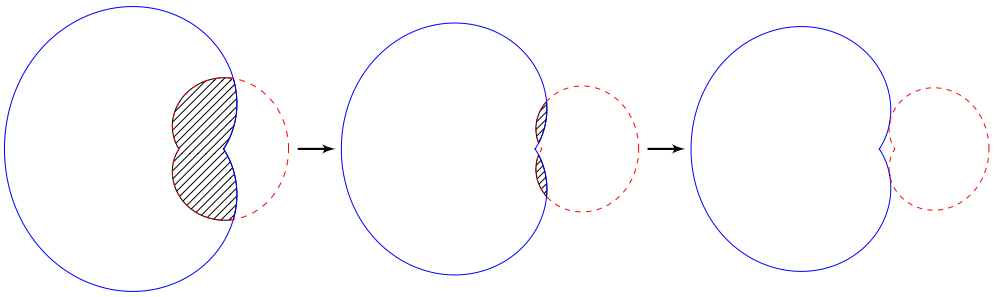

Figure 3.6: Sequence of bubble positions illustrating the procedure used to numerically measure centre−centre distance as a function of contact force magnitude. The bubbles are each held in contact by a body force which opposes the contact force. The centres of the two bubbles are moved apart until the area of overlap is below 1×10^{-8}. This is repeated for a range of force magnitudes from 0.01 to 1.

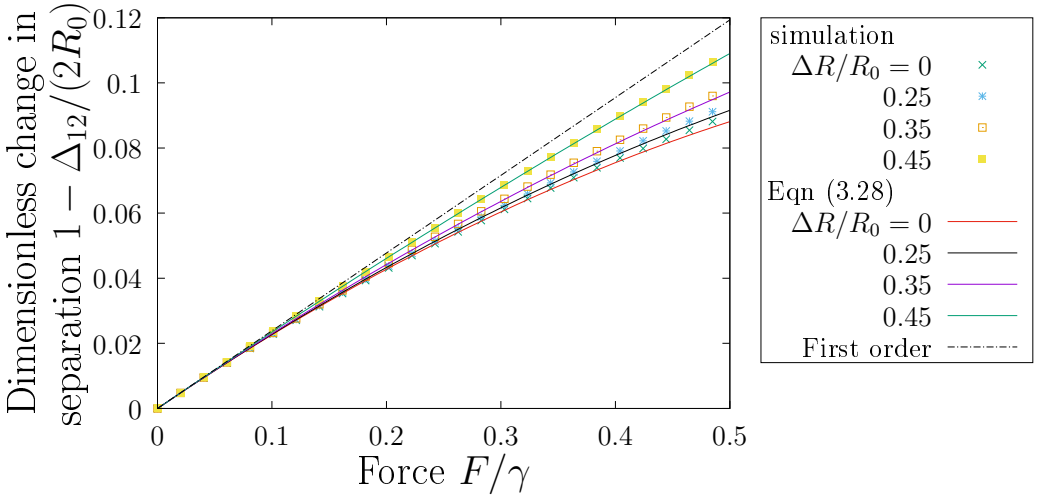

Figure 3.7: Dimensionless change in separation $1 - \Delta_{12}/(2R_0)$ versus force $f = F/\gamma$ between two 2D Morse−Witten bubble profiles (Figure 3.5) for varying size difference $\Delta R/R_0$. Symbols refer to numerical results, solid lines to Equation (3.26). Up to a normalised force of 0.5 the relative error of the theory is less than 2%, beyond this the theory begins to become less accurate.

$R_2 = 0$, the correction term vanishes as the interaction is properly described by a point force, and no longer an approximation.

In order to test the accuracy of Equation (3.26), we proceed as follows. For a given force, f, and size relationship $\Delta R/R_0$, we draw two overlapping bubbles with facing contacts, using Equations (3.2) and (3.13) (see sequence in Figure 3.6). The bubbles are each held in contact by a body force which opposes the contact force. The centres of these are moved apart until their area of overlap is zero, giving the separation for that force. The rightmost image, where the bubbles are just in contact, is what we wish to achieve. However, the process used here is not practical for large systems, so for large scale simulation we will use the approximation given by Equation (3.28).

For the range of normalised force shown ($0 < f < 0.5$), Equation (3.28) produces a relative error $< 2\%$ (the relative error when considering only the linear part of Equation (3.28) is up to 25%).

3.1.5 Contact with Multiple Bubbles

We will now apply the case of the single contact between two bubbles of different sizes to a bubble i with multiple contacts j, i.e. a bubble in a foam. In this case, the deformation, x_{ij}, of bubble i at its contact with bubble j, is determined by the sum over all of the contacts of bubble i,

$$x_{ij} = -\frac{R_i}{2\pi\gamma}\left(\sum_k^N F_{ik} g(\Delta\theta_{jk})\right) - \frac{R_i F_{ij}^2}{2\gamma^2(2 + R_i/R_j + R_j/R_i)}. \tag{3.29}$$

Here $\Delta\theta_{jk}$ is the angle between the centre-centre lines of bubbles ij and ik, and k enumerates all the contacts of bubble i (including j).

Figure 3.8 shows Equation (3.29) in action. The profile of a bubble with four unequal contact forces at four unevenly spaced points is shown on the left. On the right is a closer look at just the top contact, where the cap of

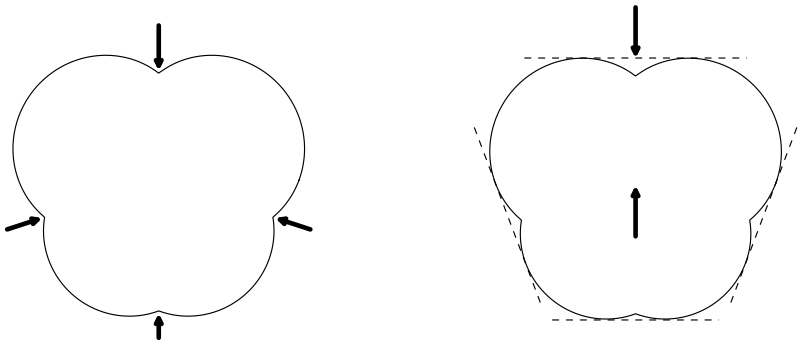

Figure 3.8: Left: The profile of a two dimensional Morse−Witten bubble resulting from the linear combination of the individual profiles associated with each of the four contacts. Right: Capping the profile to show the effective deformation at each contact. The capping procedure is similar to mean field aproximations, where the remaining contacts are averaged while considering one contact in particular.

the contact is shown as a dashed line. The contribution of the other three contacts can be thought of as providing the body force for the top contact, the body force being illustrated in the centre of the bubble. This is similar to the ideas of mean field theory, where the interactions of the other contacting bubbles are averaged while considering one particular contact.

Note, however, that the linearised theory contains errors of order f^2 from the outset, which we do not claim to eliminate. Given that, the theory is surprisingly successful in improving the lowest order estimate.

3.2 Formulation of a Two Dimensional Morse–Witten Foam Model

We will proceed to apply Equation (3.29) to find an equilibrium structure of a polydisperse foam, in a numerical simulation. We consider N bubbles in

equilibrium in a square box with periodic boundary conditions. The bubbles are represented by their centroid positions ($\mathbf{c}_i$) and radii, R_i. A contact between bubbles i and j has an associated contact force of magnitude F_{ij}.

This non-linear problem is naturally approached by iterative methods. While its defining equations are simple, its implementation is challenging, because of the role of the contact network, which needs to be continually monitored and updated, as explained below.

3.2.1 Defining Equations

We seek an equilibrium configuration which satisfies the conditions stated in *A-D* below where the variables to be yielded by iteration are

- the centre positions, $\mathbf{c}_i$,
- the contact force magnitudes, F_{ij},
- and the contact deformations, x_{ij}.

A) Force-Deformation Relation

Forces and deformations must be consistent, that is, satisfy Equation (3.29).

B) Deformation-Displacement Relations

For each contact, the separation of centres of mass, located at positions $\mathbf{c}_i$ and $\mathbf{c}_j$ must be consistent with the deformations x_{ij} and x_{ji}, according to

$$R_i - x_{ij} + R_j - x_{ji} = |\mathbf{c}_i - \mathbf{c}_j|. \tag{3.30}$$

C) Action-Reaction

At each contact the force on bubble i due to bubble j must balance the force on bubble j due to bubble i, so

$$F_{ij} = F_{ji}. \tag{3.31}$$

D) Equilibrium of Forces

The vector net forces on each bubble i must satisfy

$$\sum_{j}^{N} F_{ij} \frac{\mathbf{c}_j - \mathbf{c}_i}{|\mathbf{c}_j - \mathbf{c}_i|} = 0. \tag{3.32}$$

3.2.2 The Contact Network

As the system approaches equilibrium, the shapes and positions of bubbles change. The contact network is not finally determined until equilibrium is reached, consistent with the above conditions. It requires updating as the approach to equilibrium proceeds. As discussed at the beginning of this chapter, Buzza and Cates [81] applied the Morse−Witten theory to the case of an emulsion where the drops are arranged on a simple cubic lattice, for which this difficulty does not arise. Höhler and Cohen-Addad [82], while including a slight polydispersity, also used crystalline systems in which contact changes were excluded. In the soft disk model contact changes occur naturally as part of the energy minimisation proceedure as each contact is independant. For the disordered foams discussed here the contacts are coupled together, thus a new methodology is thus needed to deal with bubble rearrangements (topological changes).

3.3 Implementation of the Morse–Witten Model

3.3.1 Iterative Scheme

We have developed a practical iterative scheme that can produce an equilibrium structure satisfying the conditions of Section 3.2. Separate steps of iterations are designed to bring the configuration closer to satisfaction of these conditions.

A) Force-Deformation Relation

Given a configuration and deformations of each bubble contact, the corresponding forces are found by solving Equation (3.29) for F_{ik}, for each bubble in turn. This is a non-linear equation, hence we solve it iteratively. This difficulty is also to be found in the work of Höhler and Cohen-Addad [82], and we adopt the same method as was used by them. That is, in each iteration, the forces from the previous iteration are inserted in the quadratic term, leaving a linear system of equations to be solved. Additionally, we apply some damping to this procedure, implemented as

$$F^{(n+1)} = aF^{(n+1)} + (1-a)F^{(n)} \tag{3.33}$$

where we have found $a = 0.9$ to be a sufficient criterion. This helps to prevent divergent oscillations in the forces.

B) Deformation-Displacement Relations

The deformations are updated by

$$x_{ij}^{(n+1)} = x_{ij}^{(n)} + \frac{R_j}{R_i + R_j}\Big[(R_i - x_{ij}^{(n)} + R_j - x_{ji}^{(n)}) - |\mathbf{c}_j - \mathbf{c}_i|\Big] \tag{3.34}$$

in order to satisfy Equation (3.30).

C) Action-Reaction

F_{ij} and F_{ji} are replaced by their average magnitude in order to balance contacts.

D) Equilibrium of Forces

Each bubble located at position $\mathbf{c_i}$ is moved in the direction of the net force acting on it, according to

$$\mathbf{c}_i^{(n+1)} = \mathbf{c}_i^{(n)} + b \sum_j^N F_{ij}^{(n+1)} \frac{\mathbf{c}_i - \mathbf{c}_j}{|\mathbf{c}_i - \mathbf{c}_j|}, \tag{3.35}$$

where $b = 0.1R_0/\gamma$. This is the largest value found for which the algorithm converges. If non-convergence is encountered, this value can be decreased, at the cost of slower approach to convergence.

The flowchart of the iteration is shown in Figure 3.9. Note that it contains additional steps in which the contact network is, if necessary, altered.

3.3.2 Updating the Contact Network

Negative Forces

A negative force indicates a spurious contact that is formed while the system is out of equilibrium and these are removed from the contact network. In practice, at most one negative force is eliminated per bubble in a given iteration to provide stability of the algorithm. This is performed after updating the forces.

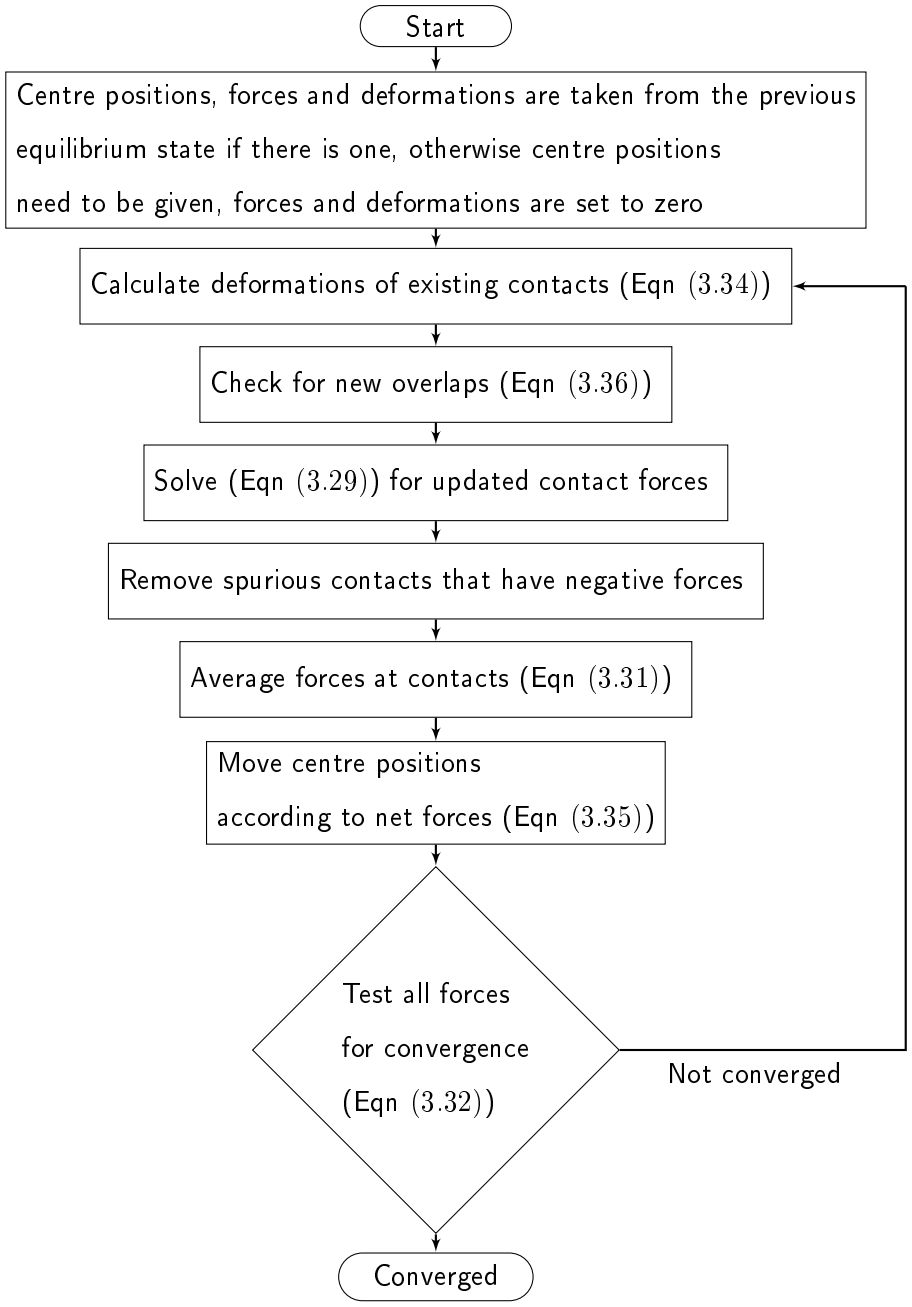

Figure 3.9: Iteration scheme for the computation of a two dimensional Morse−Witten foam. While the net forces are not balanced, deformations, overlaps, and contact forces are calculated and the centroid positions moved accordingly. For a given collection of bubbles in a given confinement this procedure can be used to find an equilibrium configuration.

Overlapping Bubbles

After moving the bubble positions, nominally non-contacting bubbles may overlap with each other. To detect this we calculate

$$x_{ij} = \frac{R_j}{R_i + R_j}\Big[\rho(\theta_{ij}) + \rho(\theta_{ji}) - |\mathbf{c}_j - \mathbf{c}_i|\Big] \tag{3.36}$$

for each possible pair i, j. For $x_{ij} > 0$, bubbles i and j overlap, which requires an update of the contact network. This is performed before updating the forces.

3.3.3 Convergence

The algorithm is terminated when the two dimensional foam is close to equilibrium, satisfying all of the above requirements. This is determined numerically by calculating the net force on each bubble in the foam using the left hand side of Equation (3.32). We deem this equation to be satisfied for all bubbles if the largest net force encountered, F/γ, is less than 10^{-4}.

In this case, the recurrence relation for the centroid positions given by Equation (3.35) will have converged, leading also to a convergence of Equation (3.30) for the deformations. Thus, solving the deformation-force relationship Equation (3.29) repeatedly will produce the same set of contact forces each time and all the defining equations will be satisfied.

When the algorithm converges, the approach to convergence is exponential, as in Figure 3.10. When convergence does not occur, the maximum net force features oscillations, as in Figure 3.11. Both of these examples are for the ten bubbles test simulations depicted in Figure 3.12, at $\phi = 0.138$ and $\phi = 0.137$ respectively. Visual inspection of the resulting foams does not reveal any obvious differences or abnormalities, so the results are not

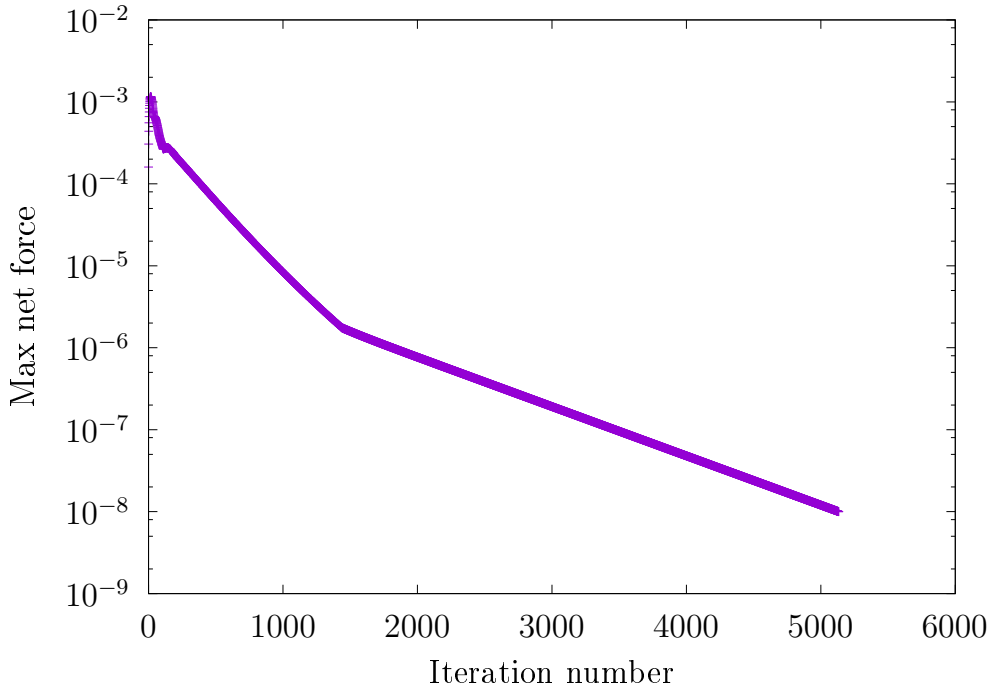

Figure 3.10: A semi-logarithmic plot of the maximum net force as a function of iteration number for a test simulation of ten bubbles. In this case the convergence criterion was set to 10^{-8} to study the behavior. Since the remaining net force decreases exponentially with the iteration number, a small increase in the number of iterations provides a large decrease in the remaining net force, but it will never go to zero net force (just small enough). A criterion of 10^{-8} was deemed to be excessive in practice, so 10^{-4} was selected for general use.

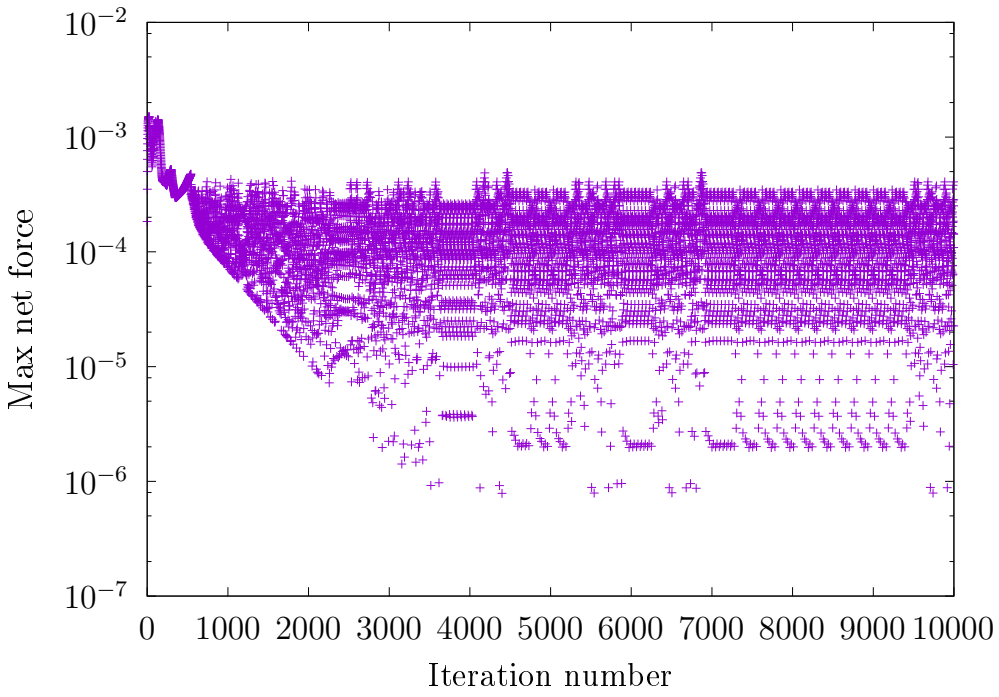

Figure 3.11: An example of a ten bubble simulation that did not approach convergence. Instead, the maximum net force appears to enter into oscillations. This is avoided if the convergence criterion is not excessively small.

discarded. It is not yet clear how the algorithm may be improved to avoid this, some suggestions will be outlined in Chapter 5.

3.4 Tests and Typical Results

We have run tests of the above scheme for systems of up to 200 bubbles, in a square box with periodic boundary conditions. The computations converged satisfactorily for liquid fractions exceeding around $\phi = 0.12$, below which the forces diverge. We have not identified the reason for non-convergence beyond that point, but it is hardly surprising in a non-linear problem of this kind. This may be rectified in due course, see Section 5.3.

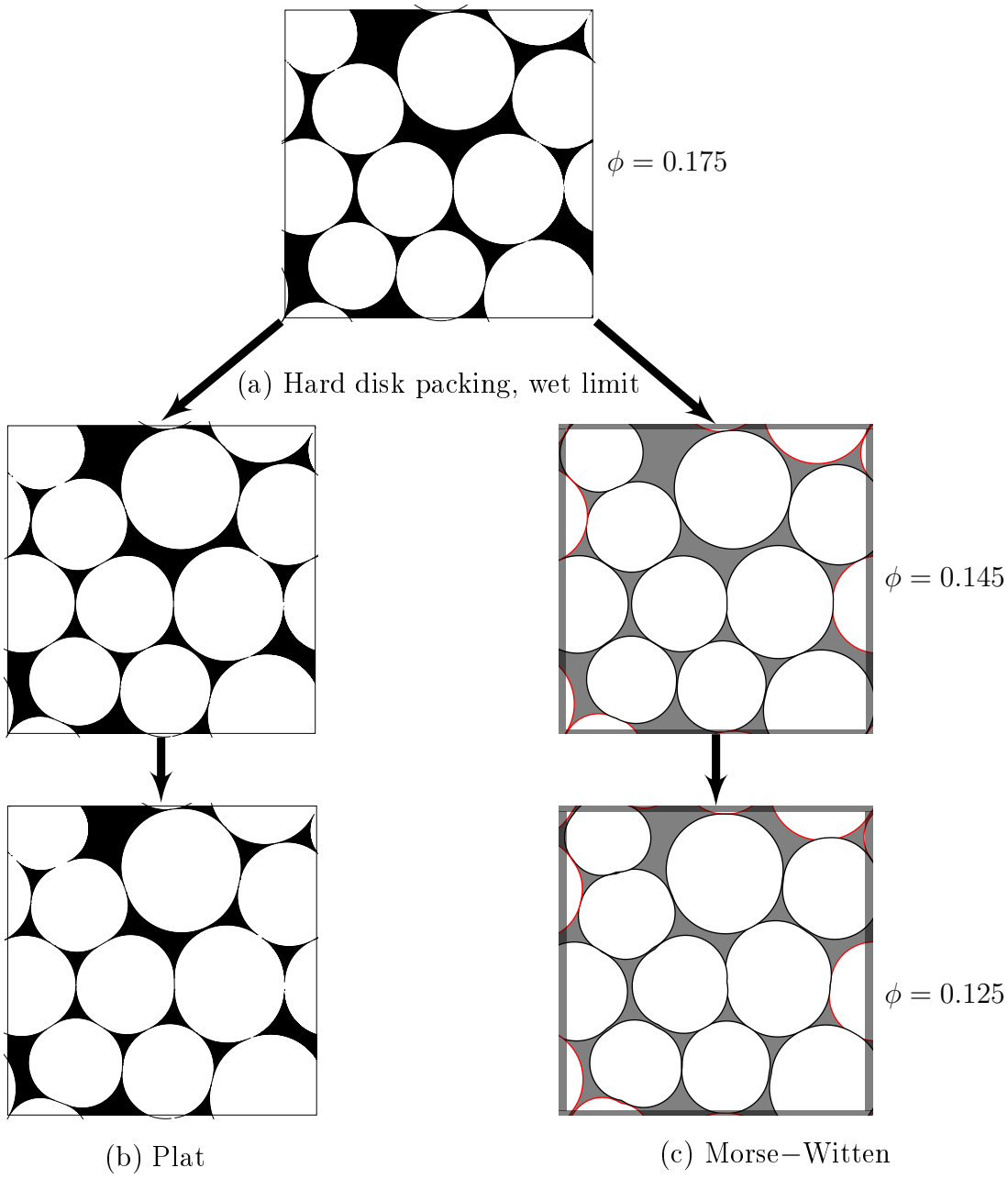

Figure 3.12: Comparison of polydisperse two dimensional foam as computed using the Plat simulation software [32] and the Morse−Witten formulation. Each structure is derived from the same hard disk packing (a), by gradually decreasing the liquid fraction in steps of $\Delta\phi = 0.001$. The two simulation methods produce almost the same sequence of contact changes. Note that in (c) the contact dimples are still visable. They are left in for simplicity when plotting, but are corrected in the simulations.

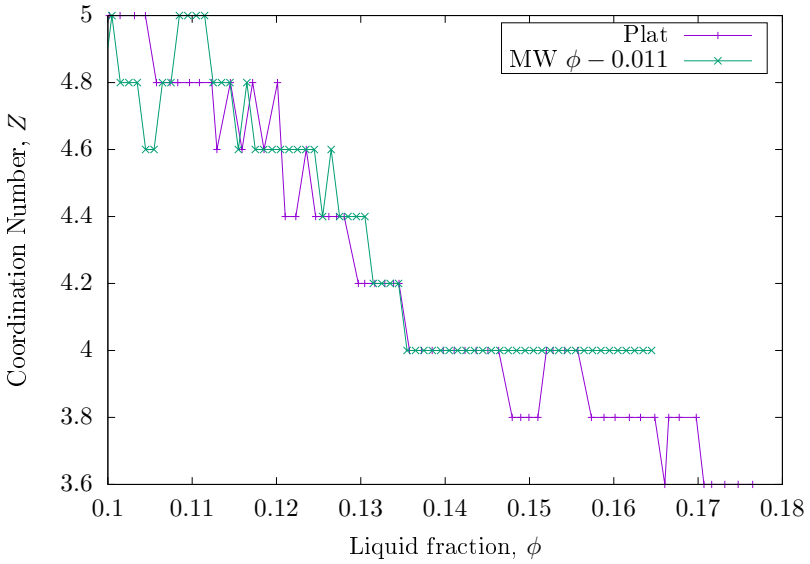

Figure 3.13: The coordination number of the two foam simulations depicted in Figure 3.12 as a function of ϕ. The Morse−Witten simulation has been shifted by -0.011 in order to align the two curves. The broad alignment of the successive steps in the coordination number Z shows that most of the same contact changes occur in both simulations. Around $\phi < 0.12$ the models begin to disagree, this is consistent with other limitations of the Morse−Witten model.

In order to validate the method, we have compared it with simulations using the Plat software, as introduced in Section 2.1.1. To begin, a system of ten bubbles with a polydispersity of $\sqrt{\langle R^2\rangle/\langle R\rangle^2 - 1} \simeq 0.12$ was generated using the Plat software and the liquid fraction, ϕ, reduced until a hard disk packing was achieved (Figure 3.12(a), top). As discussed in Section 1.2.1, a hard disk packing corresponds to a foam in the wet limit (at $\phi = \phi_c$) where all of the degrees of freedom are exactly taken up by the contacts between bubbles, and there are no additional constraints. In this case the average number of contacts is $4(1 - 1/N) = 3.6$ [2]. Ten bubbles constitutes a small enough system that, despite the general failure of Plat to converge in the wet

limit (see Section 2.1.2), the cost of repeating simulations until it is found to be successful is sufficiently small (10 seconds) so as to make it feasible. The centre positions of the bubbles were extracted and used to create a Morse−Witten simulation of the same system. The liquid fraction of both simulations was then decremented in parallel, down to a liquid fraction of approximately $\phi \approx 0.12$.

We found that the Morse−Witten simulation produced almost the same contact changes as the Plat simulation, although at values of ϕ shifted by roughly $\Delta\phi \simeq 0.01$ higher (see Figure 3.13). In looking at this comparison, it should be borne in mind that the Morse−Witten formalism is inherently approximate.

We next consider the excess energy of a Morse–Witten foam, defined (in dimensionless form) by

$$\varepsilon = \frac{1}{4\pi R_0 \gamma} \sum_{i=0}^{N} \sum_{j} x_{ij} F_{ij}, \tag{3.37}$$

where j enumerates the contacts of bubble i.

For ordered monodisperse foam, Princen calculated $\varepsilon(\phi)$ exactly [84, 45]. This presents a good test for the Morse–Witten model, which can be solved exactly in this case. Figure 2.3(a) shows excellent agreement between Princen's exact result and the analytic solution of the Morse–Witten model in the wet limit ($\Delta\phi < 0.02$). Our numerical simulation results match the analytic solution of the Morse–Witten model.

Also shown is a simple approximate solution of the Morse–Witten model, which can be obtained as follows. The energy per contact is given by elementary methods as $0.5F\delta R/(\gamma R_0)$ and using the relation

$$\frac{F}{\gamma} = \frac{6Z}{\pi} \frac{\delta R}{R_0} \tag{3.38}$$

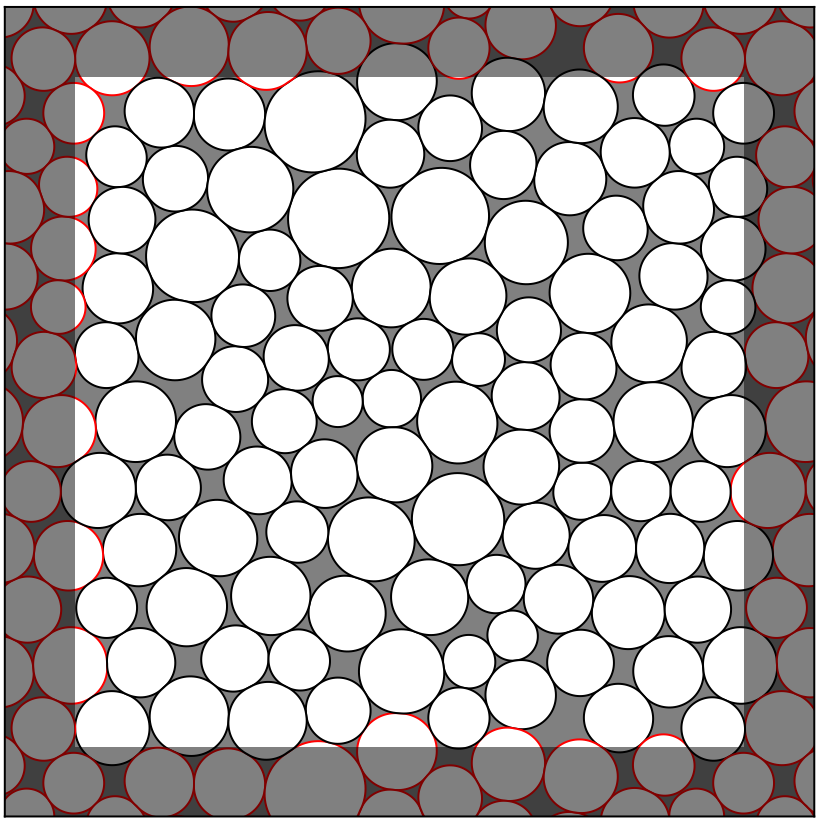

Figure 3.14: Example of a 100 bubble simulation at $\phi = 0.13$. Periodic boundaries are indicated by the grey border. Periodic copies of bubbles from the unit cell are plotted in red.

from Weaire *et al.*[83], along with the affine compression relation $\delta R/R_0 = \Delta\phi/2(1-\phi)$, we obtain

$$\varepsilon(\Delta\phi) = \left(\frac{3}{\sqrt{2\pi}}\frac{\Delta\phi}{\Delta\phi + \phi_h}\right)^2, \tag{3.39}$$

where $\phi_h = \pi/2\sqrt{3}$ is the critical packing fraction for a hexagonal disk arrangement. This relation (shown in Figure 2.3(a)) is in excellent agreement with both our numerical data for monodisperse foam in the wet limit and the result of Princen for $\Delta\phi < 0.015$.

In order to study the variation of excess energy ε as a function of liquid

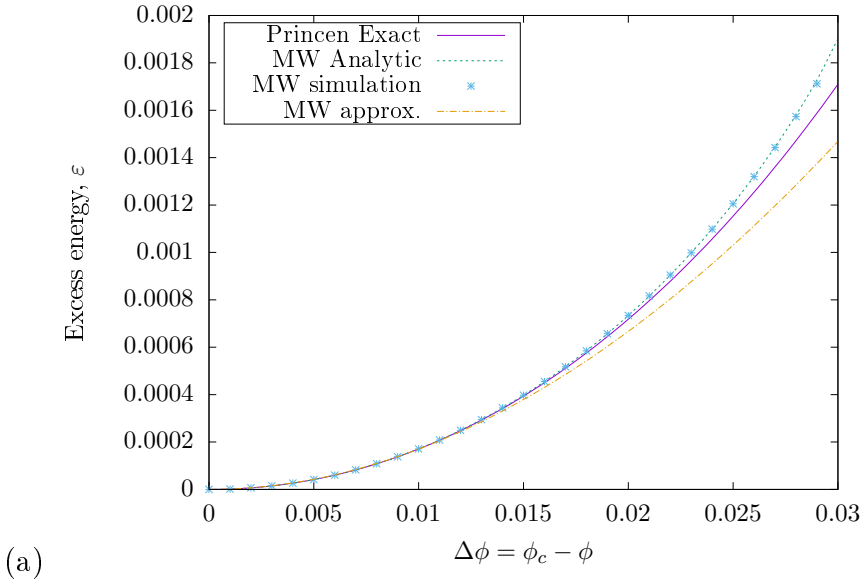

(a)

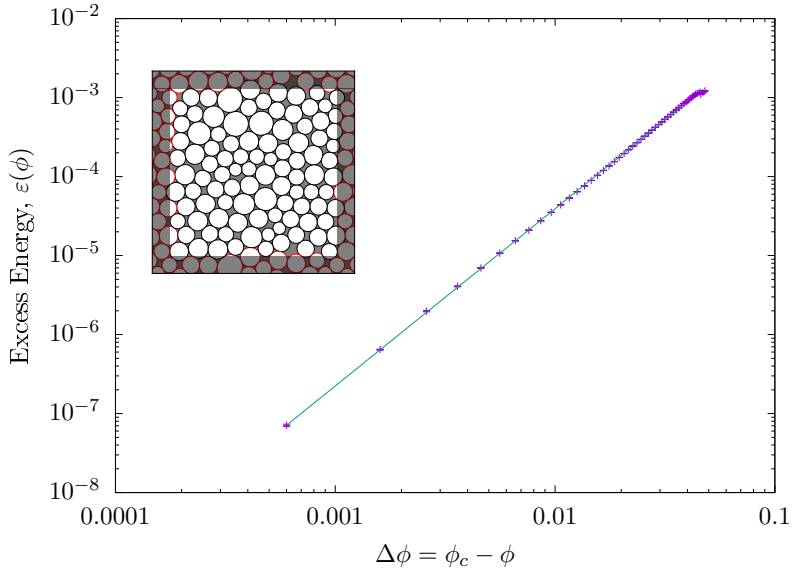

(b)

Figure 3.15: Variation of normalised excess energy ϵ (Equation (1.3)) as a function of $\Delta\phi = \phi_c - \phi$). (a) In the case of an ordered monodisperse foam the Morse–Witten theory reproduces the exact result first derived by Princen [45, 84] (data points: simulation, dashed line: analytic). Also shown is a simple analytic approximation obtained from Morse–Witten theory (Equation (3.39)) (dot-dashed line). (b) For disordered foams, our simulations of 1000 systems of 100 bubbles each show that the excess energy is proportional to $\Delta\phi^{2.2}$. An example of one of the simulated foams is shown in the inset.

fraction of polydisperse foams, 1000 foams of 100 bubbles each were prepared with an average polydispersity of 0.21 ± 0.02. These simulations were run for a range of liquid fraction from 0.18 to 0.12 in steps of 0.001. They were started deliberately higher than the expected value of $\phi_c \simeq 0.16$ so that the transition from unjammed collection of disks to jammed foams will not be missed. The critical value ϕ_c, marks the onset of the excess energy.

Our simulations show that, similar to results from Plat [1], close to ϕ_c, the energy varies roughly quadratically with the distance $\Delta\phi = \phi_c - \phi$ from ϕ_c. Therefore, the values for ϕ_c were calculated individually for each 100 bubble system by fitting a straight line to the lowest eight points of the square root of the energy curve that were above 10^{-4}. The average value obtained from this procedure is 0.843 ± 0.003, consistent with previously published values for ϕ_c [33, 2, 55, 22, 34, 56]. The energy curves for these simulations were shifted by their respective ϕ_c values, and then averaged with a bin width of 0.001 in $\Delta\phi$ to smooth the data. Figure 3.15 shows that, based on our 1000 simulations, $\varepsilon(\Delta\phi) \propto \Delta\phi^{2.2}$.

In the study of granular matter, it is common to compute the contact force network [85, 86]. Granular packings are characterised by a very slow decay of the distribution of forces greater than the mean. Whether this is exponential or faster than exponential depends on the details of the simulations/experiments, such as dimensionality, solid friction, and partial size distribution [87, 88, 89].

In Figure 3.16(a) we show the contact force network for an equilibrated Morse−Witten foam of 100 bubbles at a liquid fraction of $\phi = 0.13$. The width of each line in the contact network is proportional to the force magnitude. In addition, the bubbles are shaded according to their individual excess energies. Also shown in Figure 3.16 is a preliminary normalised distribution

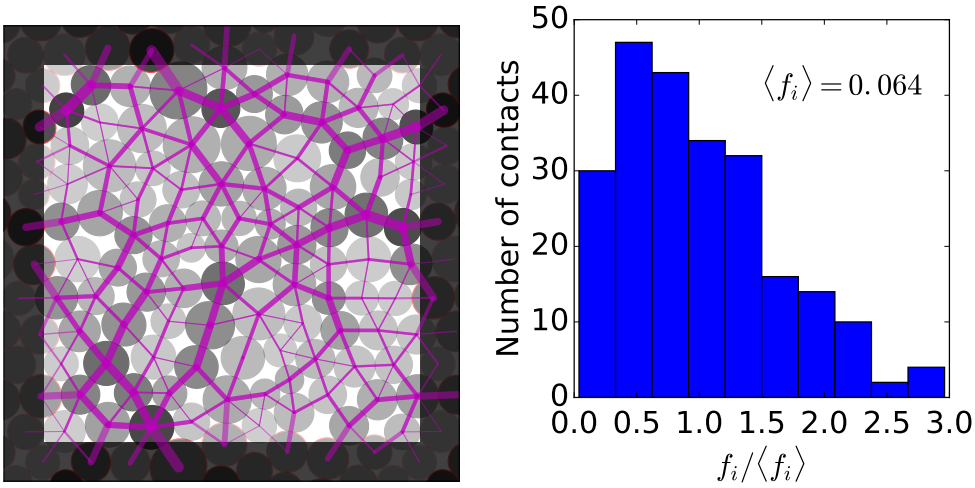

(a) Force network **(b)** Force distribution

Figure 3.16: (a) Wet foam ($\phi = 0.87$) with 100 bubbles showing the contact force network. The thickness of the lines is proportional to the force magnitude and the grey scale is proportional to the individual excess energy of a bubble. (b) Normalised distribution of forces. This is in qualitative agreement with that found by Höhler and Cohen-Addad [82].

of contact forces. This is broadly similar to that found by Höhler and Cohen-Addad [82]; however, further simulations are required to analyse its shape.

3.4.1 Extension to a Three Dimensional Foam

The methodology developed above for the simulation of a two dimensional foam based on the Morse−Witten model also lends itself to application for three dimensions. As in two dimensions the foam will be represented by the centroid of all bubbles and a network of contacts. In three dimensions, the profile is expressed analogously to Equation (3.2), and Equation (3.13) becomes

$$\frac{\delta R(\theta)}{R_0} = \frac{-F}{\gamma R_0} G(\theta) \tag{3.40}$$

where

$$G(\theta) = -\frac{1}{4\pi}\left\{\frac{1}{2} + \frac{4}{3}\cos\theta + \cos\theta \ln\left[\sin^2(\theta/2)\right]\right\}, \tag{3.41}$$

as in Section 3.1.1. The expression for the deformation of bubble i, equivalent to Equation (3.29) and derivable in the same way, is given by

$$x_1(F) = \frac{F}{4\pi\gamma}\left[\frac{11}{6} - \frac{2R_2}{R_1+R_2} + \ln\left(\frac{FR_2}{4\pi R_1\gamma(R_1+R_2)}\right)\right], \tag{3.42}$$

to lowest order in F. The relative change in separation (equivalent to Equation (3.28)) between two bubbles where $R_1 = R_0 + \Delta R$ and $R_2 = R_0 - \Delta R$ is

$$1 - \frac{\Delta_{12}}{2R_0} = \frac{F}{4\pi\gamma R_0}\left(\frac{5}{6} + \ln\left(\frac{F}{8\pi\gamma R_0}\right)\right). \tag{3.43}$$

Again, symmetry tells us not to expect any terms of odd orders of ΔR in the separation. Equation (3.42) would need to be expanded to order F^2 to give terms of ΔR^2. Taking, for example, $\Delta R = 0.1R_0$, $F = 0.5\gamma R_0$, the relative error that would result from using a formula for a monodisperse foam would be of order 10^{-4}. This explains the success by Höhler and Cohen-Addad [82] in using an expression derived for the monodisperse case in treating a slightly polydisperse case.

In order to model a three dimensional foam, an equivalent to Equation (3.29) is required. This is obtained by adding a non-local term to Equation (3.42) (see Höhler and Cohen-Addad, [82]) giving

$$x_{ij}(F) = \frac{F}{4\pi\gamma}\left[\frac{11}{6} - \frac{2R_j}{R_i+R_j} + \ln\left(\frac{FR_j}{4\pi R_i\gamma(R_i+R_j)}\right)\right] + \sum_{k\neq j} G(\Delta\theta_{jk})\frac{F_{ik}}{\gamma}. \tag{3.44}$$

Similar to the procedure of Section 3.1.4, we determined the separation of two three dimensional Morse−Witten bubbles at their point of contact, for a given force F. We found that Equation (3.43) is reasonably accurate up to $F/(R\gamma) \sim 0.5$ (corresponding to the dry limit) for low polydispersity,

and $F/(R\gamma) \sim 0.05$ (corresponding to $\phi \sim 0.24$) for high polydispersity. The appearance of a logarithmic term makes the three dimensional case somewhat different from the two dimensional one presented here; nevertheless, we hope that further improvement of the two dimensional methods will assist in the greater computational task of implementation in three dimensions.

3.5 Conclusion

We have started this chapter by explaining the Morse−Witten theory for the deformation of bubbles and drops. This was then reformulated in two dimensions, before arriving at a methodology for the simulation of two dimensional foams close to the wet limit.

We have shown how polydispersity can be accommodated in the Morse−Witten theory in such a way as to give satisfactory results for a typical disordered polydisperse foam that is close to the wet limit. The extension of the theory to three dimensions is quite natural, although the implementation becomes conceptually more difficult to visualise and check, and there is an obvious increase in computational demands. The transparency of the theory and its direct relation to a force network (Figure 3.16(b)) is attractive. However, it should be noted that it has proven to be a computational challenge that was hardly anticipated, and is worthy of further attention.

In the polydisperse foam the interfaces are curved. This is accounted for in the model presented here, being incorporated into Equation (3.29) for dealing with differences in bubble sizes. One might well ask what is the case in a monodisperse disordered foam? Despite some doubts in the past, this can indeed exist, even in two dimensions. Since the bubbles are not equivalent, surely their pressures are slightly different, hence the interfaces

are curved? This is correct in principle, but the effect is surely much smaller than in the case of polydisperse bubble, and of higher order in the forces than what is considered here.

Chapter 4

Using the Three Dimensional Morse–Witten Model to Compute the Surface Tension of Bubbles or Droplets

Efforts to determine the surface tension of a liquid drop from measurements of its shape date back to the 19^{th} century. In this chapter I will show how the Morse−Witten theory, introduced in Chapter 3, can be successfully applied to this problem, in the case of both hanging and sitting drops. After a brief review of historical work (Section 4.1), I will discuss how this problem can be treated within the framework of the Morse−Witten model. This includes the derivation of the analytic expression that depends on two simple length measurements, and on knowing the relative density of the two fluids. In Section 4.3, I will demonstrate both the theoretical accuracy of the derived expression, using numerical solutions of the Young−Laplace equation, together with an assessment based on some preliminary experimental data.

4.1 History of Surface Tension Measurements

The history of the measurement of the surface tension of a liquid by the observation of the shape of a liquid drop in equilibrium under gravity (or the conditions for its instability) goes back well into the 19^{th} century. The most notable milestone was the contribution of Bashforth and Adams [90], which is still widely cited, in both the present context and the methodology of the numerical solution of ordinary differential equations. Their objective was to provide extensive and accurate tables of drop radius versus surface tension, by means of which the value of surface tension could be extracted from shape measurements.

Many methods follow the same general approach, later translated into modern computational form. While reliable, they are still elaborate and somewhat obscure, since they generally involve "black box" commercial or open software for computation of shape using image analysis. Here we offer a complementary method - an extremely simple and transparent alternative, grounded in analytic theory.

Evaluation of surface tension of a *sessile* (sitting) drop (see Figure 4.1 (left)), based on a simple formula which only involved a pair of length measurements (maximum drop diameter and height of drop from top to equator), appears to date back to Worthington in 1885 [93]. He improved upon an initial (cruder) formula by Georg Quincke (1858) [94], which only involved one length (the total height of the drop). Various further simple formulae were suggested, and are reviewed in the book by Rusanov and Prokhorov [95]. However, all of these approximations have one thing in common: they only apply for wide (flat) sessile drops, corresponding to drop diameters exceeding 1.5cm in the case of water, i.e. much larger than the capillary length (see Section 1.2.2). Rusanov and Prokhorov proceed to state in 1996 that in order to calculate

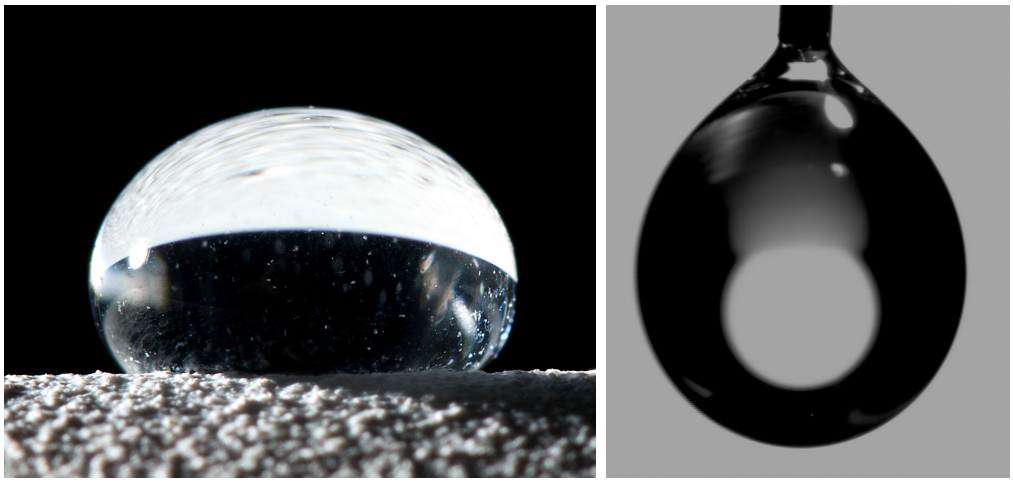

Figure 4.1: Examples of a (left) sessile and (right) pendant drop. Image credit: (left) Brigham Young Univ. 2014. URL: https://www.laboratoryequipment.com/news/2014/05/super-waterproof-surfaces-make-water-bounce-ball (visited on 01/29/2018), (right) Flickr user 'Rather Anonymous'. 2005. URL: https://www.flickr.com/photos/79262083@N00/34743746/in/photostream/

surface tension for the case of sessile drops of smaller dimensions, "one needs to use numerical methods" [95].

The analysis of *pendant* (hanging) drops (see Figure 4.1 (right)) using a pair of length measurements dates back to Andreas *et al.* [96] in 1938, who used the maximum drop diameter and the drop diameter as measured at that distance away from the apex. Surface tension may then be computed from tabulated values obtained from numerical solutions of the Young−Laplace equation (see Section 1.3.2) [97, 98], together with numerical approximations and interpolations [99]. (The table initially provided by Andreas *et al.* [96] was based on experimental measurements of drop shapes.)

For a sessile drop, the above choice for measurements of drop dimensions is not possible. The maximum drop diameter (measured at a horizontal plane),

and the distance of this plane from the apex provides an alternative pair of dimensions, suitable for the characterisation of both pendant and sessile drops. The pair features in the (cumbersome) second order perturbation solutions of the Young–Laplace equation, as derived by O'Brien and van den Brule [100] for the computation of surface tension. It is also used in our method described below.

None of the above methods, we believe, have the transparency and analytical basis of what is described here. Our method can be applied in either two or three dimensions for both pendant and sessile drops. The two dimensional case may be of limited practical value, but we will also present the resulting equation for line-tension in that case.

All of what we present applies equally well to the case of a bubble in a liquid under gravity, with obvious changes.

The new formula is based on the theory of Morse and Witten (Section 3.1.1), which provides an explicit analytical formula for drop shape, in a linear approximation (Equation (3.8)). That is, it is exact in the limit of high surface tension (or small drop size). We will indicate the regime in which this approximation is reasonably accurate (within 2% of the true surface tension) in Section 4.3.

Our work should prove to be a useful and instructive adjunct to the principal current methods. It yields an immediate value for the surface tension, by means of a simple formula, requiring only two length measurements related to the drop profile.

4.2 Application of the Morse–Witten Theory to Pendant and Sessile Drops

Here I show how the analytic theory of Morse and Witten was applied to the problem of measuring surface tension. Much of the theoretical work in Hutzler *et al.* [3] was carried out by Hutzler and Weaire, while the numerical calculations were performed by Ryan-Purcell. My main contribution to this is Section 4.3, where I explore the theoretical accuracy of the method by comparing it with direct numerical solutions of the Young−Laplace equation. The result is an analytic relationship between the drop size and the accuracy of the Morse−Witten estimate of the surface tension.

To demonstrate the essence of the method, Figure 4.2 shows examples of both sessile and pendant liquid drops, together with relevant notation. We will derive a formula for their values of surface tension γ in terms of the two distances, L_x (maximum "equatorial" drop radius) and L_y (distance of this equator to the drop apex), which are indicated in Figure 4.2. This assumes knowledge of $\Delta\rho g$, the product of density difference of two fluids and acceleration due to gravity. The boundary condition at a contacting plane or nozzle outlet is does not factor into the measurement, provided it does not break the rotational symmetry of the drop.

To these cases we apply the analytic results of Morse and Witten (Equation (3.8)). These were not motivated by our present objective; rather they were aimed at developing a method of simulating the interactions of multiple bubbles (or drops) and exploring the form of that interaction in the limit of slight contact [82] as we laid out in Chapter 3. To our knowledge, the results of Morse and Witten have never been used to provide insights or methods for surface tension methods, as below, or indeed introduced into the general

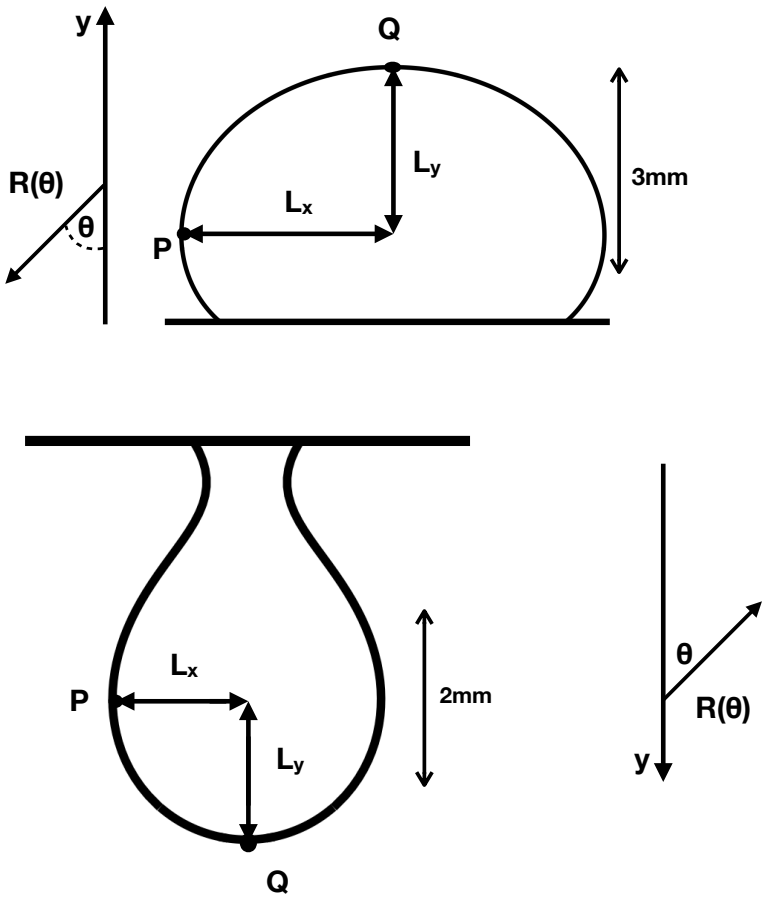

Figure 4.2: Examples of profiles of sessile and pendant drops (computed by integrating the Laplace equation (Equation (4.9)) using standard numerical methods [101]) with relevant notation. Measurements of both L_x and L_y are sufficient to obtain an estimate of surface tension (for given value of $\Delta\rho g$). (Top) Sessile water drop: $\Delta\rho g = 9810kg/m^3$, volume $4\pi/3(3mm)^3$ and surface tension of water, $\gamma = 72mN/m$ result in values $L_x = 2.645mm$ and $L_y = 2.235mm$. Using Equation (4.8) we arrive at an estimate of surface tension as $71.7mN/m$, underestimating the exact value by about 0.4 %. (Bottom) For a pendant water drop of volume $4\pi/3(2mm)^3$ measurements of $L_x = 1.474mm$ and $L_y = 1.593mm$ result in an estimate of surface tension as $71.9mN/m$, using Equation (4.8). The exact value is thus underestimated by about 0.2 %, indicating high accuracy.

theory of sessile and pendant drops. This may be attributed to the difficulty of the theoretical framework presented by Morse and Witten [83]. Despite this, its essential results are simple, compact, and easily applied.

The analysis described in Chapter 3 gives the profile of a bubble or drop as

$$\rho(\theta) = R_0 + \delta R(\theta) \tag{4.1}$$

where

$$\frac{\delta R(\theta)}{R_0} = \frac{-FG(\theta)}{\gamma R_0} \tag{4.2}$$

and

$$G(\theta) = -\frac{1}{4\pi}\left\{\frac{1}{2} + \frac{4}{3}\cos\theta + \cos\theta \ln\left[\sin^2(\theta/2)\right]\right\}. \tag{4.3}$$

These describe the profile of a deformed drop in spherical coordinates R and θ (the third coordinate being irrelevant on grounds of symmetry) in response to an applied force, F, acting at $\theta = 0$.

In the case considered here, F is the gravitational (or buoyancy) force of the undeformed sphere given by $F = \pm\frac{4}{3}R_0^3\pi\Delta\rho g$, where the '+' sign is for sessile and the '$-$' sign for pendant drops. We note that Morse and Witten [48] only considered the case in which $F \geq 0$, corresponding to a sessile drop (or a drop contacting another drop). The possibility of also studying pendant drops appears to be a new application of the theory.

Note again the divergence of the profile at the point of contact visible in Figure 4.3 for both the sessile and pendant cases. As in Section 3.1.1, the divergent part of the profile may be neglected by selecting appropriate boundary conditions. The remaining solution for the displacement $\Delta R(\theta)$ is small for all angles θ, for small F.

In general, our method can be applied in various situations, such as Figure 4.2 (top) or (bottom), which feature non-zero contact angles, provided an equator exists (i.e. contact angle $> 90°$). In this case, the configuration

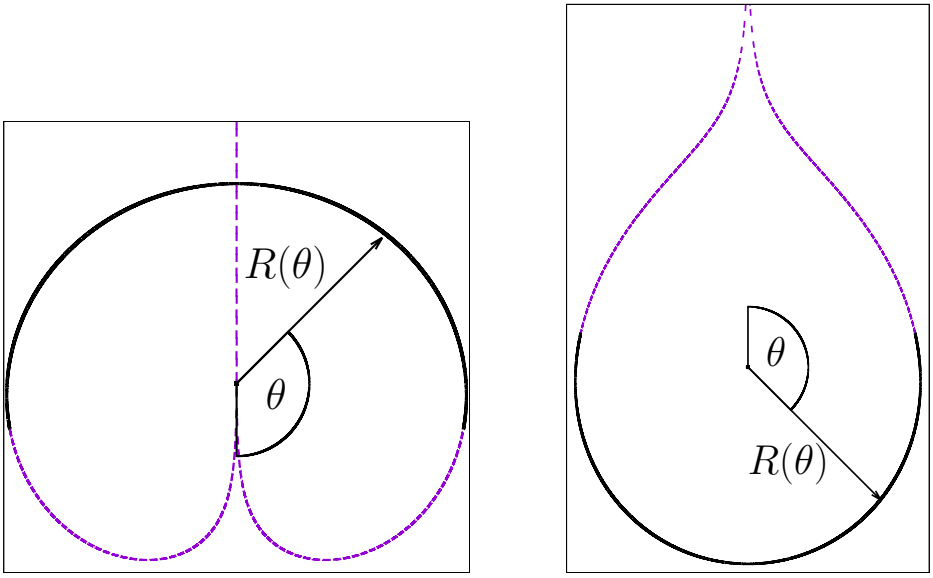

Figure 4.3: Examples of profiles of sessile and pendant drops, obtained from the result of Morse and Witten, Equations (3.2) and (3.8). Only the parts indicated by thick solid lines represent the physical drops of Figure 4.2. The end points of the thick solid lines have been chosen to be near the equator for illustrative purposes. Note that our derived equation for surface tension, Equation (4.8), applies regardless of the boundary conditions imposed within the other part of the profiles (and also regardless of the volume that is enclosed).

can be extended past the contact plane to create the standard Morse−Witten setup, as shown in Figure 4.3 with a small force $F = \pm\frac{4}{3}\pi R_0^3 \Delta\rho g$.

In the following we adopt the Morse−Witten result, Equation (3.8) originally or Equation (4.3) above, to arrive straightforwardly at a method of estimating surface tension γ.

At the equator (point P in Figure 4.2), the tangent of the profile of the drop is vertical for our chosen coordinate system. The corresponding angle, θ_P, is thus determined from

$$\frac{\mathrm{d}}{\mathrm{d}\theta}(\rho(\theta)\sin\theta)|_{\theta=\theta_P} = 0, \tag{4.4}$$

where $\rho(\theta)$ is given by Equation (4.1). Solving for θ_P, where we write $\theta_P = \pi/2 + \delta\theta_P$, and Taylor expanded cosine and sine terms to first order in $\delta\theta_P$ we get

$$\delta\theta_P \simeq \frac{2F(3\log(2)-4)}{3(5F+8\pi\gamma R_0)}. \tag{4.5}$$

From this, and keeping only terms to first order in F, we can compute the location of P=(P$_x$,P$_y$).

$$\begin{aligned} P_x &= R_0\left(1+\frac{F/(\gamma R_0)}{8\pi}\right) \\ P_y &= R_0\left(1-\frac{F/(\gamma R_0)}{4\pi}(\ln 2 - 1/2)\right). \end{aligned} \tag{4.6}$$

We thus obtain the following expression for L_x and L_y, with $L_x = P_x$ and $L_y = \rho(\pi) - P_y$,

$$\begin{aligned} L_x &= R_0\left(1+\frac{F/(\gamma R_0)}{8\pi}\right) \\ L_y &= R_0\left(1-\frac{F/(\gamma R_0)}{4\pi}(\ln 2 - 1/2)\right). \end{aligned} \tag{4.7}$$

We proceed by computing the sum and difference of L_x and L_y, resulting in $L_x - L_y = (\ln 2/4\pi)F/\gamma$ and $L_x + L_y = 2R_0 - (\ln 2 - 1)/(4\pi)F/\gamma$. Setting $F = \pm\frac{4}{3}R_0^3\pi\Delta\rho g$, as above, we can eliminate R_0 to arrive at the following exact expression for surface tension, which we denote by γ_{MW}, since it is based on Morse−Witten theory,

$$\gamma_{MW} = \frac{\Delta\rho g \ln 2}{24}\frac{(L_x+L_y)^3}{|L_x-L_y|}\left[1 \mp 3c + 3c^2 \mp c^3\right], \tag{4.8}$$

with $c = \left(\frac{1-\ln 2}{\ln 2}\right)\frac{|L_x-L_y|}{L_x+L_y}$ ($\mp$: $-$ for sessile drop, $+$ for pendant). There are no terms with order higher than c^3. This expression is accurate in the limit $\gamma^{-1} \to 0$, as will be shown below. For practical purposes the c^2 and c^3 terms are negligible.

4.3 Assessment of the Accuracy of the new Formula

Figure 4.2 shows examples of the application of Equation (4.8) to estimate surface tension for test cases representing sessile and pendant water drops. Shown are accurate solutions of the Young−Laplace equation (Equation (4.9), below), computed by standard numerical methods [101], for $\Delta\rho g = 9810kg/m^3$, volume $4\pi/3 \times (3mm)^3$, and surface tension of water, $\gamma = 72mN/m$. The Young−Laplace equation being solved is

$$2\kappa = \frac{\Delta\rho g}{\gamma}x + \frac{\Delta P_0}{\gamma}, \tag{4.9}$$

where κ is the mean curvature, $\Delta\rho$ is the density difference between the drop and its surroundings, g is the acceleration due to gravity, γ is the surface tension of the interface, and ΔP_0 is difference in pressure between the two fluids when they are not in contact. The solution for the boundary shape as a function of height is found using standard numerical methods [101]. Determination of L_x and L_y from these solutions results in estimates of surface tension from Equation (4.8) as $\gamma_{MW} = 71.7mN/m$ (sessile drop) and $\gamma_{MW} = 71.9mN/m$ (pendant drop), corresponding to 0.4% and 0.2% errors, respectively.

To investigate the variation of accuracy of our estimate γ_{MW} compared to the exact result, we have carried out simulations for a range of drop volumes and surface tensions (γ) (for a fixed density of water). We present our results in Figure 4.4 in terms of the variation of $L_x - L_y$ with $L_x + L_y$, the relevant combinations in Equation (4.8). Drop volumes for the simulations were chosen such that γ_{MW} (Equation (4.8)) was within either 0.5%, 1%, 1.5%, or 2% of the value of γ set in the simulation. From Figure 4.4, we find that, for data with the same percentage accuracy ϵ, $L_x - L_y$ varies roughly

linearly with $L_x + L_y$ i.e.

$$\frac{(L_x - L_y)}{(L_x + L_y)} = c\epsilon \tag{4.10}$$

where the constant $c = 0.11 \pm 0.01$ (sessile drop), and $c = -0.06 \pm 0.01$ (pendant drop). Given values for L_x and L_y, this allows the computation of the accuracy of the estimate of γ from Equation (4.8).

Figure 4.5 shows Equation (4.8) and the data from Figure 4.4 in the form of a plot of the dimensionless ratios $\Delta\rho g/\gamma(L_x + L_y)^2$ versus $|L_x - L_y|/(L_x + L_y)$. The small deviations between the theory based on the Morse−Witten result and the precise numerical values is an indication of the accuracy of the Morse–Witten approximation, Equation (4.8), for both sessile and pendant drops. As expected, the Morse−Witten result is asymptotically exact in the limit of small deformation.

Having established the accuracy of the theory, what accuracy can we expect from applying Equation (4.8) to actual physical measurements? Images obtained with digital cameras result in a length resolution of at best $0.001mm$ per pixel. It is straightforward to see that L_x can be determined to within $\pm$ 1 pixel. However, there has been some discussion as to the accuracy of determining, L_y [102, 95], which, when treated in the framework of random errors, is greatly magnified. When looking at a pixelated image, it is obvious that the accuracy in L_y is also ± 1 pixel. This systematic error is due only to the coarse-graining of the picture. The error in γ_{MW} is then given by

$$\Delta\gamma_{MW}(L_x, L_y) = ((\frac{\partial\gamma_{MW}}{\partial L_x})^2 + (\frac{\partial\gamma_{MW}}{\partial L_y})^2)^{1/2}\Delta L \tag{4.11}$$

where ΔL is the accuracy in L_x or L_y.

To test our result we have applied Equation (4.8) to photographs of a pendant water drop published by [103] (Figure 4.6). Values for L_x and L_y were obtained using the ImageJ software [104], resulting in $\gamma_{MW} = 69mN/m$.

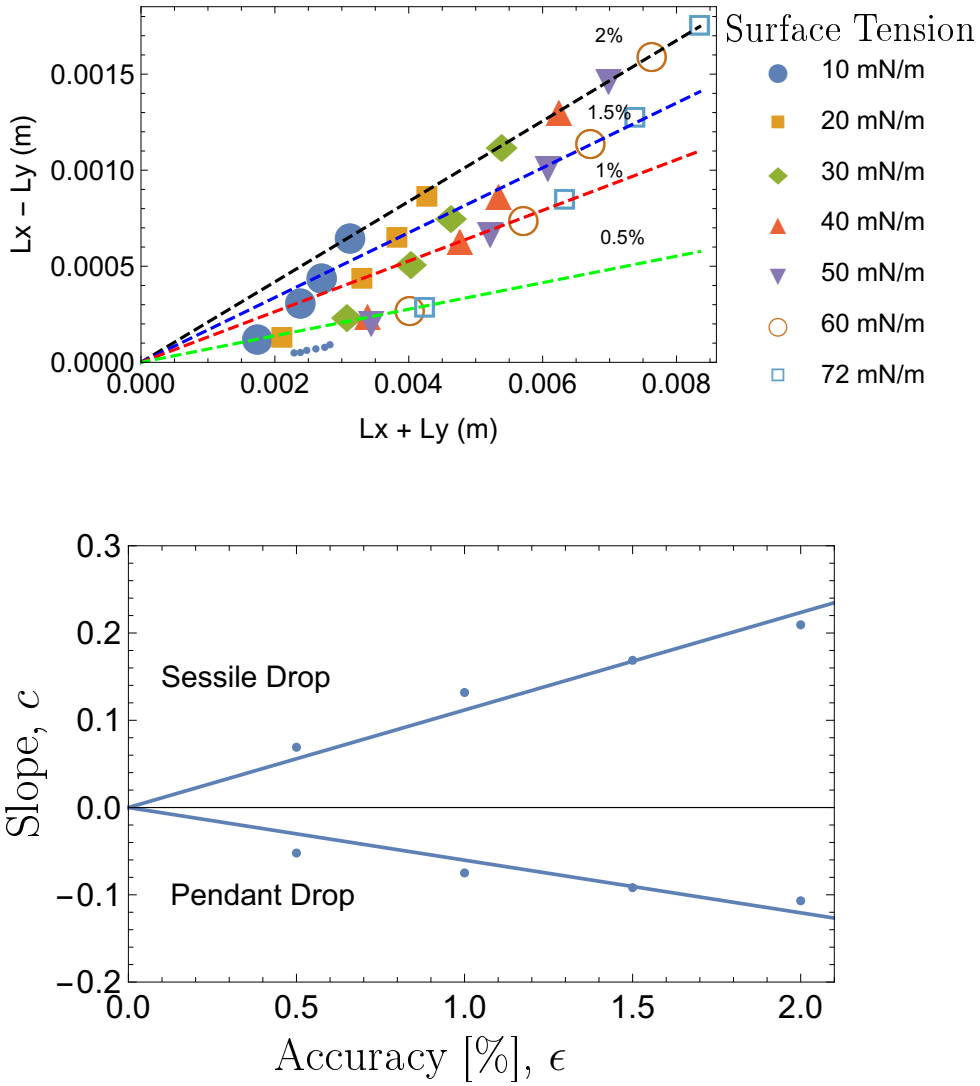

Figure 4.4: (Top) Variation of the difference of our two length measurements $(L_x - L_y)$ as a function of their sum $(L_x + L_y)$ for numerical solutions, carried out for both sessile and pendant drops over a range of values of surface tensions equal to and below that of water. Dashed lines mark the respective accuracy of the estimate γ_{MW}. (Bottom) Slope of the lines of constant accuracy as a function of accuracy, see Equation (4.10). For details, see Section 4.3.

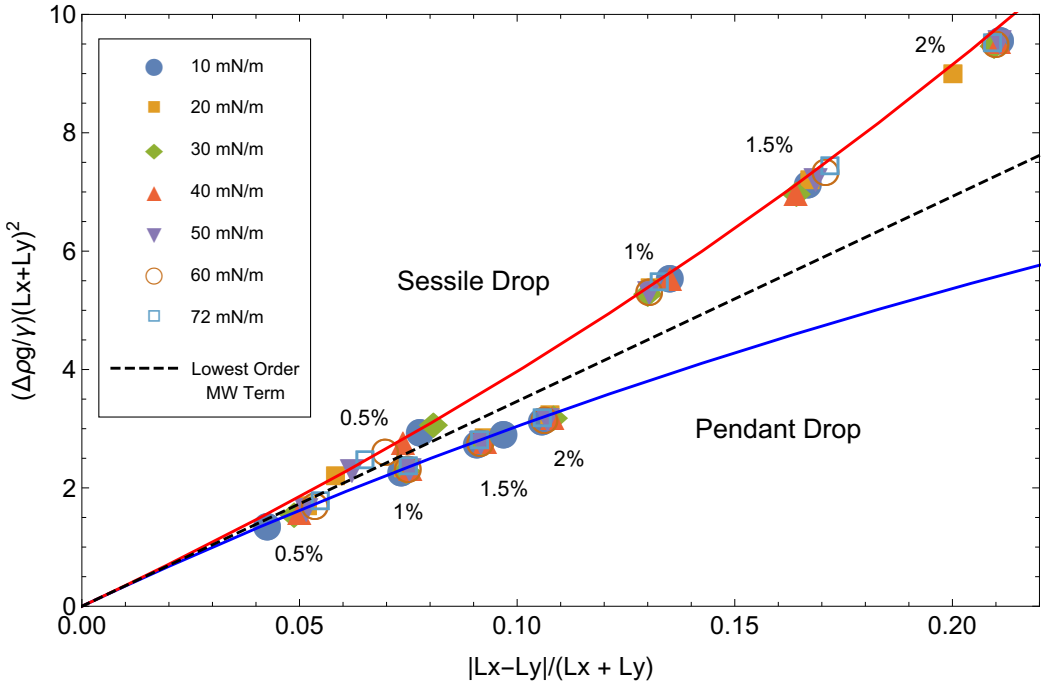

Figure 4.5: A dimensionless plot of the data in Figure 4.4. Solid lines are obtained from Equation (4.8), with the sessile case in red and pendant case in blue. The dashed line is the prefactor of Equation (4.8). The percentages indicated refer to the percentage error inγ_{MW} relative to the γ set in the simulation.

Note that in the published version of the image, the pixel resolution is only $\Delta L = 0.01mm$. Evaluating $\Delta\gamma_{MW}$ we get $\pm 6mN/m$. Our value of $\gamma_{MW} = 69 \pm 6mN/m$ is then in agreement with the value of $72mN/m$ given by the authors [103].

Figure 4.7 shows a drop of a water and glycerol mixture in silicone oil.

4.4 Conclusions

Following the work of Rotenberg *et al.* [105] and Huh and Reed [106] in 1983, many papers were published that describe the evaluation of surface

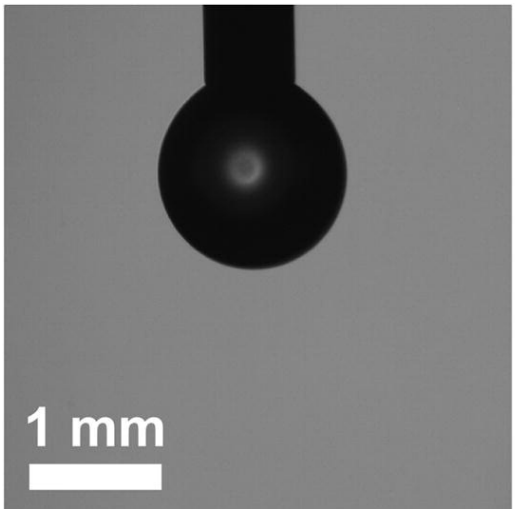

Figure 4.6: Sample pendant drop image from Berry *et al.* [103]. Calculated $\gamma_{MW} = 69 \pm 6mN/m$ is in agreement with the value of $72mN/m$ given by the authors.

Figure 4.7: Example of a pendant drop. Image credit: Steven Burke, TCD Foams group.

tension based on the comparison of an image of the entire drop profile with numerical solutions (see, for example, [107, 108, 103]). While such an approach will be more accurate for numerical evaluation, we believe that the method described here offers complementary advantages. It is based on an analytically tractable theory, which is exact in the limit of small drop deformation, the mathematical procedure is brief and transparent, and it results in an equation for surface tension, Equation (4.8), which has a very simple form.

The formula can also be generalised to other pairs of measurements (e.g. the pair used by [97], see Section 4.1), by using non zero values on the right hand side of Equation (4.4). This might mitigate measurement error, and it will also allow for an extension of our formula to the case of a sessile drop with contact angle greater than $\pi/2$ (where L_x doesn't exist). We will examine this in future work, in which we will apply our result to the analysis of experimental data for pure water and surfactant solutions, requiring a computational scheme to extract values of L_x and L_y from high resolution drop images. As we have shown above, the determination of these lengths to high accuracy is important for an accurate estimation of surface tension.

Finally, for completeness, the derivation shown in Section 4.2 can also be carried out for two-dimensional drops, using the corresponding two dimensional equations of the Morse−Witten model [83]. This results in the following expression (exact for the model),

$$\tilde{\gamma}_{MW\,two\,dimensional} = \frac{(\pi - 2)}{4} \Delta\tilde{\rho} g \frac{L^3}{|L_x - L_y|}. \tag{4.12}$$

Here $L = L_x$ for a pendant drop and $L = L_y$ for a sessile drop, $\tilde{\rho}$ denotes a two dimensional density (mass/area) and $\tilde{\gamma}_{MW}$ is a line tension (with dimension of a force). However, it is unlikely to be of much use, as even quasi-two dimensional systems will be better understood with the three dimensional

form.

Chapter 5

Outlook

Having summarised the achievements of each chapter locally, I will outline how one could progress the different strands of the work here.

5.1 Improvements to the Plat Software

As mentioned in Chapter 2, the Plat simulation exhibits a tendency to fail in the wet limit. A fix to this issue would be highly desirable as the Plat simulation is not based on any approximations and is thus more accurate than any approximation, such as the Soft Disk model, or the Morse−Witten model. In Section 5.1.1 I will discuss the problem of arc breakage, and in Section 5.1.2 I will outline interesting features of the failure statistics of Plat.

5.1.1 The Problem of Arc Breakage

The failure is related to an ambiguity in the size of an arc defined only by its curvature and end points. Since an arc is a piece of a circle of radius equal to the radius of curvature r, there are in general two arcs that satisfy this definition as shown by the solid lines in Figure 5.1.

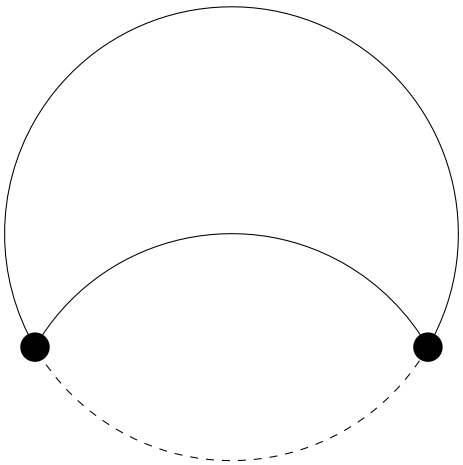

Figure 5.1: An illustration of the large arc - small arc ambiguity in the Plat simulation. The two solid lines indicate the two possible arcs with the same curvature that fit between the endpoints (black circles). The smaller arc is mirrored by the dashed line to illustrate how the large and small arc together make up a whole circle with radius equal to the radius of curvature.

If the total angle of the smaller arc is denoted by θ, then the larger arc has a total angle of $2\pi - \theta$. Problems in the simulation arise when θ approaches π. In this situation, if one of the endpoints gets displaced outwards, then it is possible that the separation between the endpoints becomes larger than $2r$, and the arc will no longer fit between the endpoints. This is termed *arc breakage* and if it is not dealt with, will cause the program to crash.

This problem was identified from the outset by Bolton and Weaire [31], their attempt to address this problem is outlined below, but it is insufficient. The procedure involves first detecting when arc breakage occurs, followed by an attempt to fix it. Detection is straightforward and simply a matter of measuring the distance between endpoints of an arc relative to the curvature of the arc. If arc breakage is detected on a bubble−bubble arc, the perimeter

of both bubbles is traversed, and any broken arcs along it are switched from being large to small or small to large (provided the accompanying change in area is in the correct direction). Then, the pressure in the bubble being traversed is lowered in an attempt to reduce the curvature of the arcs, allowing them to fit between their endpoints once more. This procedure is referred to as *border popping* [31]. This is quite successful in moderately wet foams ($\phi \lesssim 0.1$), but not very successful for foams approaching the wet limit.

In the wetter foams ($\phi \gtrsim 0.1$), what happens is that an endless sequence of border popping is triggered which neither crashes the program, nor resolves the issue. Therefore it is clear that the border popping procedure alone is insufficient to fully resolve the arc breakage. The next step would be to move the vertices that constitute the endpoints of the broken arcs. This is tricky because each vertex is at the edge of a contact with a neighbouring bubble. A potential solution would be to trigger a contact loss at one edge of a broken arc. It would be necessary to figure out how to pick the contact that should be lost, and whether this can be done in a stable and consistent manner. Finding a simple configuration that leads to continuous arc breakage is straightforward, this can then be used as a test system to study this in detail.

5.1.2 Analysis of the Failure Rate of Plat

Examining the liquid fraction reached by a simulation before it failed gives rise to Figure 5.2. This depicts the number of successful simulations as a function of liquid fraction, $N(\phi)$. The features of such quantity are of interest in the general context of failure statistics, where it is presented in its normalised form, i.e. $S(\phi) = N(\phi)/N(0)$, this is also called the survival function [109], The *mortality*, or *failure rate*, $\mu(\phi)$, of the Plat simulations

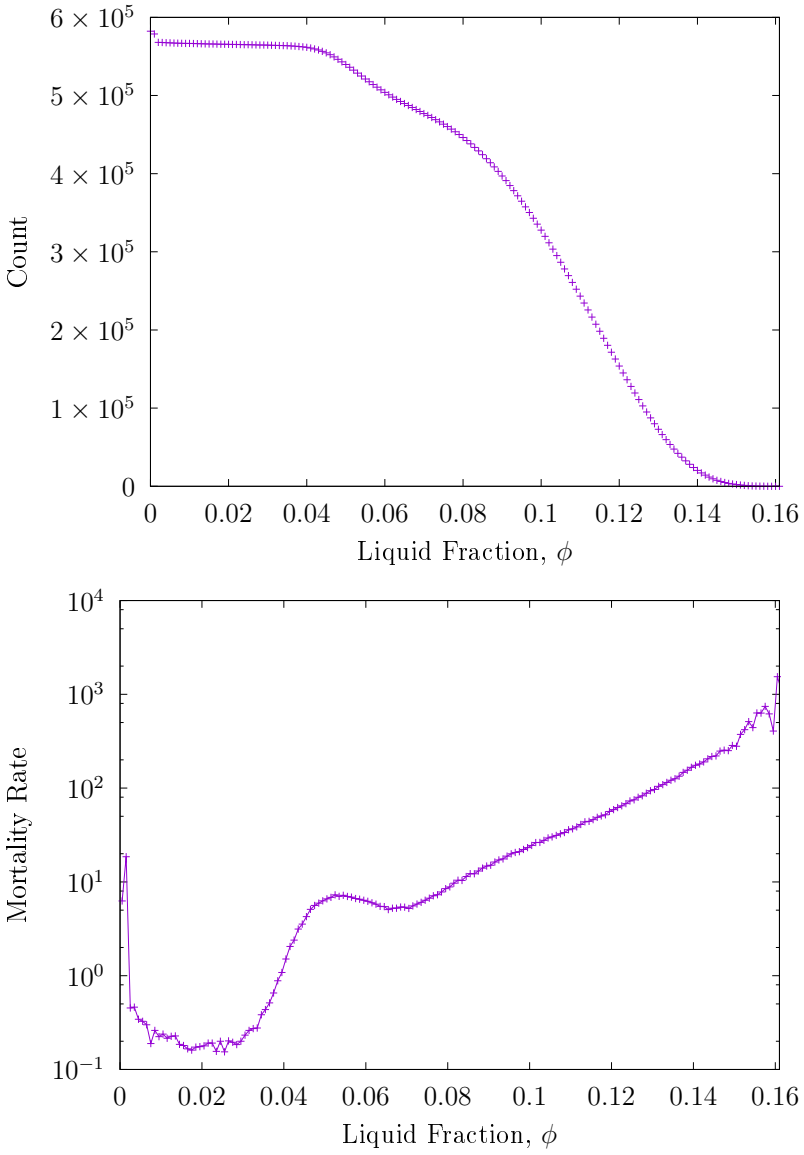

Figure 5.2: (Top) Number of successful simulations as a function of liquid fraction. The decrease in successful simulations at higher liquid fractions is due to stalls of the Plat software (see Sec. 2.1.1). (Bottom) Failure (Equation (5.1)) of simulations as a function of liquid fraction. The typical features of mortality data are visible here: a brief period of high mortality in the beginning, a period of low failure in the middle, and a strong increase (exponential in this case) in failure in the end.

may be defined as

$$\mu(\phi) = -\frac{1}{s(\phi)}\frac{\mathrm{d}s(\phi)}{\mathrm{d}\phi} = \frac{\mathrm{d}\ln[s(\phi)]}{\mathrm{d}\phi}. \tag{5.1}$$

This is shown in Figure 5.2. The typical features of failure data are visible in this plot: a brief period of high failure in the beginning, a period of low failure in the middle, and an increase in mortality in the end. Interestingly, in the Plat data, this increase is exponential and does not scale according to a power-law, as is commonly found for the failure of technical devices [109]. The exponential increase is seen in human mortality data, where it is called the Gompertz law [110].

Additional features this data displays are a brief decrease in mortality before the exponential increase, at $\phi \simeq 0.05$. This could be related to features in the local distribution of contacts, see Figure 2.8. Identifying what this feature represents, and how it is related to the initial problem of failure in the Plat simulation may shed light on how to fix the failures of Plat.

5.2 Further Analysis Using the Two Dimensional Morse–Witten Model

In Chapter 3 I have shown how we can use the theory of Morse and Witten to build a model of two dimensional foams. As discussed in Section 2.4.1, the variation of coordination number as a function of liquid fraction has been a quantity of interest in foams for a long time. Here I will outline where an analysis of $Z(\phi)$ might lead for the Morse−Witten model.

A log-log plot of preliminary data (Figure 5.3) reveals a scaling of $Z - Z_c = \Delta Z \propto \Delta\phi^{0.52}$, consistent with results for packings using the soft disk model [111]. In Chapter 2 such a scaling was disputed based on extensive computer

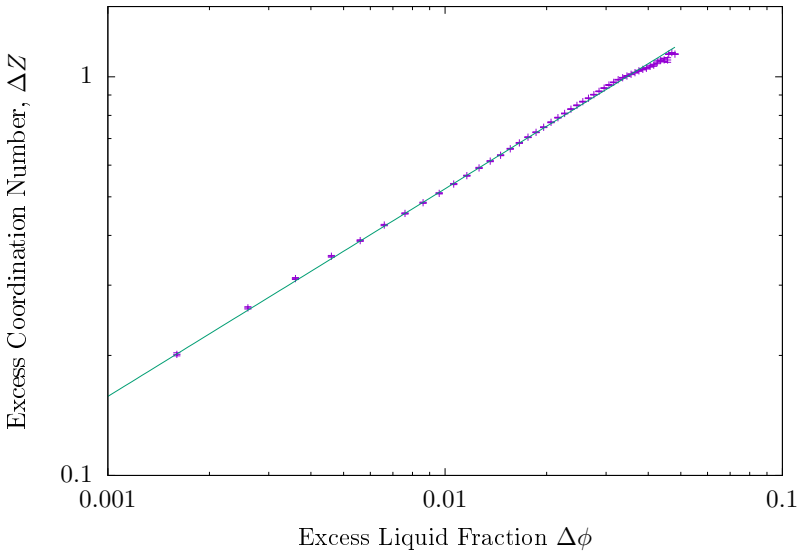

Figure 5.3: Preliminary $Z(\Delta\phi)$ data for the two dimensional Morse−Witten model. In the case of disordered foams, our simulations show an increase in the excess coordination number with $\Delta\phi$ of the form $\Delta Z \propto \Delta\phi^{0.52}$, consistent with previous simulations using the bubble model.

simulations with Plat which resulted in $\Delta Z \propto \Delta\phi$, and it was argued that this was due to the deformability of soft bubbles. The preliminary results presented here appear to put some doubts on this argument. Further simulations with Plat and the Surface Evolver software (currently restricted to finite contact angles in two dimensions as mentioned in Chapter 1) would be required to determine whether the reported linear scaling with $\Delta\phi$ might be due to some inherent bubble-bubble attraction that arises from the algorithms. An examination of the distribution of separations ($f(w)$, as in Section 2.5), may be required to give some insight into the functional form of $Z(\Delta\phi)$.

5.3 Limitations of the Two Dimensional Morse–Witten Model

The range of ϕ that is possible to study with the Morse−Witten model is limited by the assumptions that underpin the theory. Currently, in simulations with $\phi < 0.12$, the contact forces diverge to infinity and cause the simulation to crash. Whether this is due to the approximations of the theory, or the implementation of the algorithm is not yet known.

The first approximation made in Section 3.1.2 is to linearise the expression or the curvature. For the single contact case, this is valid for a contact force F much less than the surface tension γ i.e. the dimensionless contact force $f \ll 1$ [47]. Figure 2.19 reinforces this fact, showing that the capping procedure for two bubbles of different size in contact is only accurate up to $f < 0.5$. Exactly how this is related to the range of ϕ accessible by the simulation is unclear and needs to be investigated, but it is worth investigating whether it is related to our current minimum achievable liquid fraction of 0.12.

A larger range of ϕ would require the inclusion of higher order terms in the curvature expression. However, the difficulty with this is twofold. Firstly, solving a nonlinear differential equation for $\delta R(\theta)$ would prove extremely difficult. Secondly, the solutions to nonlinear differential equations are no longer additive, removing the ease of coupling the contacts on a bubble to each other. Therefore, the entire system of coupled, nonlinear differential equations would have to be solved for the whole foam simultaneously at each step. While not necessarily impossible, this problem would be much more involved, without any of the benefits of simplicity and relative ease of understanding the current model enjoys.

5.3.1 Other Two Dimensional Systems that could be Modelled with the Morse–Witten Theory

Systems under an external force may also be modelled with the Morse−Witten theory. All that would be required in this case is to add the desired additional force to the calculation of the net force on a bubble. For example, one could add a gravitational term to Equation (3.32), and the corresponding Equation (3.35).

The theory of Morse and Witten may also be applied to the case of deformable disks in ordered channel structures. These structures have been studied for the case of hard disks [112]. Using our model of deformable disks instead of the Soft Disk model would provide area conservation, and thus more applicable results.

5.4 Developing a Three Dimensional Morse–Witten Model

There already exist several models widely used for studying three dimensional foams, so why introduce yet another one? The three dimensional Bubble Model is as approximate as the two dimensional one (see Section 2.4.1) and does not reproduce the many body effects that the Morse−Witten model does, as was discussed in Chapter 3 [82]. Another common tool, Surface Evolver, can only model foams of any polydispersity if they are dry. It can only manage wet foams if they are ordered (and thus have advantageous symmetries), and even then any topological changes that should happen must be handled manually. Therefore there is a need for a model that is relatively straight forward to implement, and can deal with wet polydisperse foams in

three dimensions. The wet foam model involving the least simplifications in two dimensions is Plat (zero approximations). However, this approach cannot be extended to three dimensions as there are two principal curvatures in three dimensions, as opposed the single principal curvature in two dimensions. This leaves extending the Morse−Witten model to three dimensions.

How can this be achieved? The first step is to verify that the force-deformation relation in Equation (3.44) produces systems of equations that are solvable (i.e. no singularities in the matrix equations). Once this is confirmed, a three dimensional visualisation of the foam needs to be implemented. Without this it becomes more difficult to debug any simulations and verify that the results are physical. After that the overall algorithm proceeds much the same as in two dimensions, in fact the flowchart (Figure 3.9) should be transferable.

There are a number of simple test cases where the results are already known that the model will need to pass. The first of these is a simple ordered monodisperse foam. Here, the results can be compared with reliable Surface Evolver calculations, and to the Z-cone model [113, 114, 38]. Once the model produces correct results for a simple monodisperse foam, the relative energy of foams with bubbles arranged in face centred cubic (fcc) and hexagonally close packed (hcp) crystal structures may be compared. It was a longstanding puzzle that wet monodisperse foams prefer to order as fcc, despite the fact that, for hard spheres, there is no obvious difference in the energy and packing fraction of fcc and hcp structures. This was addressed by computing the energy difference between fcc and hcp foams with Surface Evolver [39]. It is expected that the Morse−Witten model will reproduce the differences between the energies of the two different crystal structures. After this, the introduction of polydispersity may be tested in two ways:

modeling an ordered bidisperse foam crystal (like an NaCl crystal), and an ordered crystal with slight random polydispersity of the kind that Höhler and Cohen-Addad [82] studied. In the former case it is expected that the Morse−Witten model will be able to produce the same excess energy, $\varepsilon(\phi)$, as Surface Evolver for ϕ close to the wet limit. In the latter it is expected that this implementation of the Morse−Witten model will reproduce the results of Höhler and Cohen-Addad's implementation.

After passing the above tests, the model implementation will be ready for use in simulating random polydisperse foams. Once these foams pass visual inspection, and the simulations converge, the model can be used to study a range of properties including, but not limited to, $Z(\phi)$ and $\varepsilon(\phi)$.

Another application could be the study of columnar packings of deformable spheres. Currently, columnar structures of equal volume soft spheres have been well studied [115, 116], but those models use overlapping spheres rather than deformable ones. The use of deformable spheres that conserve volume would allow better comparison with experiments, as currently the bubble interaction strength must be related to an effective spring constant.

5.5 Further Application of the Morse–Witten Theory to Measuring the Surface Tension of Drops

The expression for surface tension (Equation (4.8)) derived from the Morse−Witten theory in Section 4.2 may be applied to any liquid boundary on a fluid-fluid interface, as long as the difference in density between the two fluids is known. In particular, it might be applicable to an experiment that has recently seen

some media attention, namely the pitch drop experiment [117, 118]. This is a long running experiment (since 1944 in Trinity College Dublin (TCD), and 1927 in the University of Queensland in Brisbane) which enables the estimation of the viscosity of a sample of pitch by allowing it to drip from a funnel. With a very high viscosity (one drop every 10 years), the pitch drop can have a very elongated profile. In this regime the Morse−Witten based formula may perform better than the Young–Laplace fitting methods currently employed [103].

However, one important aspect of this that should not get overlooked is the question of whether the Morse−Witten expression, which is derived from an equilibrium theory, can actually be applied to the slowly dripping pitch drop. In other words, is the pitch drop slow enough to be considered quasi-static? This can be quantified using the *Deborah number*, the ratio of the relaxation time to the observation time [119]. If the Deborah number is small, i.e. the relaxation time is smaller than the observation time, the pitch drop can be considered to be in equilibrium. It appears that way (10 years between drips), but this can be tested experimentally by using another liquid that is quite viscous, but not prohibitively so. Honey would be an ideal candidate, being much more viscous than water, but not nearly as viscous as pitch, taking mere tens of seconds to drip. Analysing the drop shape as it evolves in time would provide information on whether the surface tension is consistent at all for a slowly dripping drop, and if so, when over the course of the drip is it most stable. In general further experiments would provide a better understanding of the accuracy and reliability of the surface tension calculation presented in Chapter 4.

Bibliography

[1] F. F. Dunne et al. "Statistics and topological changes in 2D foam from the dry to the wet limit". In: *Philosophical Magazine* 97.21 (2017), pp. 1768–1781.

[2] J. Winkelmann et al. "2D foams above the jamming transition: Deformation matters". In: *Colloids and Surfaces A: Physicochemical and Engineering Aspects* 534 (2017), pp. 52–57. ISSN: 0927-7757.

[3] Stefan Hutzler et al. "A simple formula for the estimation of surface tension from two length measurements for a sessile or pendant drop". In: *Philosophical Magazine Letters* 98.1 (2018), pp. 9–16.

[4] B Haffner et al. "Ageing of fibre-laden aqueous foams". In: *Cellulose* 24.1 (2017), pp. 231–239.

[5] F. Dunne et al. "Implementation of Morse–Witten theory for a polydisperse wet 2D foam simulation". In: *Submitted to Philosophical Magazine* (2018).

[6] Paul Stevenson. *Foam engineering: fundamentals and applications*. John Wiley & Sons, 2012.

[7] N. D. Denkov et al. "The role of surfactant type and bubble surface mobility in foam rheology". In: *Soft Matter* 5 (2009), pp. 3389–3408.

[8] N Politova, S Tcholakova, and ND Denkov. "Factors affecting the stability of water-oil-water emulsion films". In: *Colloids and Surfaces A: Physicochemical and Engineering Aspects* 522 (2017), pp. 608–620.

[9] H. S. Hele-Shaw. "The Flow of Water". In: *Nature* 58 (May 1898), p. 34.

[10] L. Bragg and W. M. Lomer. "A dynamical model of a crystal structure. II". In: *Proc. Royal Soc. London Series A* 196 (1949), pp. 171–181.

[11] S. J. Cox and E. Janiaud. "On the structure of quasi-two-dimensional foams." In: *Philosophical Magazine Letters* 88 (2008), pp. 693–701.

[12] Gijs Katgert, Matthias E. Möbius, and Martin van Hecke. "Rate Dependence and Role of Disorder in Linearly Sheared Two-Dimensional Foams". In: *Phys. Rev. Lett.* 101 (5 July 2008), p. 058301.

[13] I. Cantat et al. *Les mousses – Structure et dynamique*. Paris: Éditions Belin, 2010.

[14] M. van Hecke. "Jamming of soft particles: geometry, mechanics, scaling and isostaticity". In: *J. Phys.: Condens. Matter* 22 (2010), 033101 (24pp).

[15] D. Weaire and S. Hutzler. *The physics of foams*. Oxford: Clarendon press, 1999.

[16] Wiebke Drenckhan and Dominique Langevin. "Monodisperse foams in one to three dimensions". In: *Current Opinion in Colloid & Interface Science* 15.5 (2010), pp. 341–358. ISSN: 1359-0294.

[17] M. Reza Sadr-Lahijany, Purusattam Ray, and H. Eugene Stanley. "Dispersity-Driven Melting Transition in Two-Dimensional Solids". In: *Phys. Rev. Lett.* 79 (17 Oct. 1997), pp. 3206–3209.

[18] Sascha Hilgenfeldt. "Size-topology correlations in disk packings: terminal bidispersity in order–disorder transitions". In: *Philosophical Magazine* 93.31-33 (2013), pp. 4018–4029.

[19] J.C. Maxwell. "L. On the calculation of the equilibrium and stiffness of frames". In: *Philosophical Magazine* 27 (1864), pp. 294–299.

[20] Charles H Bennett. "Serially deposited amorphous aggregates of hard spheres". In: *Journal of applied physics* 43.6 (1972), pp. 2727–2734.

[21] G. Katgert and M. van Hecke. "Jamming and geometry of two-dimensional foams". In: *EPL (Europhysics Letters)* 92.3 (2010), p. 34002.

[22] T. S. Majmudar et al. "Jamming Transition in Granular Systems". In: *Phys. Rev. Lett.* 98 (5 Jan. 2007), p. 058001.

[23] C.S. O'Hern et al. "Jamming at zero temperature and zero applied stress: The epitome of disorder". In: *Physical Review E* 68.1 (2003), p. 011306.

[24] V. J. Langlois, S. Hutzler, and D. Weaire. "Rheological properties of the soft disk model of 2D Foams". In: *Phys. Rev. E* 78 (2008), p. 021401.

[25] Peter Sollich et al. "Rheology of soft glassy materials". In: *Physical review letters* 78.10 (1997), p. 2020.

[26] Prashidha Kharel. "Internal Dynamics and Flow Properties of Dense Granular Materials". In: (2018).

[27] Corey S. O'Hern et al. "Random Packings of Frictionless Particles". In: *Phys. Rev. Lett.* 88 (7 Jan. 2002), p. 075507.

[28] W. H. Herschel and R. Bulkley. "Konsistenzmessungen von Gummi-Benzollösungen". In: *Kolloid Zeitschrift 39, 291-300 (1926)* 39 (1926), pp. 291–300.

[29] HM Princen and AD Kiss. "Rheology of foams and highly concentrated emulsions: III. Static shear modulus". In: *Journal of Colloid and Interface Science* 112.2 (1986), pp. 427–437.

[30] F. Bolton and D. Weaire. "The effects of Plateau borders in the two-dimensional soap froth. I. Decoration lemma and diffusion theorem." In: *Phil. Mag. B* 63 (1991), pp. 795–809.

[31] F. Bolton and D. Weaire. "The effects of Plateau borders in the two-dimensional soap froth. II. General simulation and analysis of rigidity loss transition." In: *Phil. Mag. B* 65 (1992), pp. 473–487.

[32] F. Bolton. "Software PLAT: A computer code for simulating two-dimensional liquid foams". In: *https://github.com/fbolton/plat* (1996).

[33] F. Bolton and D. Weaire. "Rigidity loss transition in a disordered 2D froth". In: *Physical Review Letters* 65 (1990), p. 3449.

[34] D. J. Durian. "Foam mechanics at the bubble scale". In: *Phys. Rev. Lett.* 75 (1995), pp. 4780–4783.

[35] H. M. Princen. "Rheology of Foams and Highly Concentrated Emulsions II. Experimental Study of the Yield Stress and Wall Effects for Concentrated Oil-in-Water Emulsions". In: *J. Colloid Interface Sci.* 105 (1985), pp. 150–171.

[36] S. Hutzler, D. Weaire, and F. Bolton. "The effects of Plateau borders in the two-dimensional soap froth, III. Further results". In: *Phil. Mag. B* 71 (1995), p. 277.

[37] K. A. Brakke. "The Surface Evolver". In: *Experimental Mathematics* 1 (1992), pp. 141–165.

[38] S Hutzler et al. "Z-cone model for the energy of an ordered foam". In: *Soft matter* 10.36 (2014), pp. 7103–7108.

[39] D. Whyte et al. "The relative energy of fcc and hcp foams". In: *Philosophical Magazine Letters* 95.6 (2015), pp. 319–323.

[40] S J Cox et al. "Vertex corrections in the theory of foam drainage". In: *Journal of Physics: Condensed Matter* 13.21 (2001), p. 4863.

[41] D. Lipsa et al. "FoamVis: Visualization of 2D Foam Simulation Data". In: *IEEE Transactions on Visualization and Computer Graphics* 17.12 (Dec. 2011), pp. 2096–2105. ISSN: 1077-2626.

[42] A. Wyn, I. T. Davies, and S. J. Cox. "Simulations of two-dimensional foam rheology: Localization in linear Couette flow and the interaction of settling discs". In: *The European Physical Journal E* 26.1 (May 2008), pp. 81–89. ISSN: 1292-895X.

[43] I.T. Davies and S.J. Cox. "Sedimenting discs in a two-dimensional foam". In: *Colloids and Surfaces A: Physicochemical and Engineering Aspects* 344.1 (2009), pp. 8–14. ISSN: 0927-7757.

[44] Simon Cox and I. Tudur Davies. "Simulations of quasi-static foam flow through a diverging-converging channel". In: *Korea-Australia Rheology Journal* 28.3 (Aug. 2016), pp. 181–186. ISSN: 2093-7660.

[45] S. J. Cox et al. "Ideal wet two-dimensional foams and emulsions with finite contact angle". In: *Soft Matter* 14 (28 2018), pp. 5922–5929.

[46] M. D. Lacasse, G. S. Grest, and D. Levine. "Deformation of small compressed droplets". In: *Physical Review E* 54.5 (1996), pp. 5436–5446.

[47] R. Höhler and D. Weaire. "Can liquid foams and emulsions be modeled as packings of soft elastic particles?" In: *Submitted to Advances in Colloid and Interface Science* (2018).

[48] DC Morse and TA Witten. "Droplet Elasticity in Weakly Compressed Emulsions". In: *EPL (Europhysics Letters)* 22.7 (1993), pp. 549–555.

[49] L.D. Landau et al. "CHAPTER I - FUNDAMENTAL EQUATIONS". In: *Theory of Elasticity (Third Edition)*. Ed. by E.M. LIFSHITZ, A.M. KOSEVICH, and L.P. PITAEVSKII. Third Edition. Oxford: Butterworth-Heinemann, 1986, pp. 1–37. ISBN: 978-0-08-057069-3.

[50] B. N. Delaunay. "Sur la sphère vide." French. In: *Bull. Acad. Sci. URSS* 1934.6 (1934), pp. 793–800.

[51] D. Weaire and J. P. Kermode. "Computer simulation of a two-dimensional soap froth. II. Analysis of results". In: *Phil. Mag. B* 50 (1984), pp. 379–395.

[52] J. P. Kermode and D. Weaire. "2D-Froth: A Programme for the Investigation of 2-Dimensional Froths". In: *Comp. Phys. Commun* 60 (1990), pp. 75–109.

[53] D. Weaire and J. P. Kermode. "Computer simulation of a two-dimensional soap froth. I. Method and motivation". In: *Phil. Mag. B* 48 (1983), pp. 245–259.

[54] S Hutzler and D Weaire. "The osmotic pressure of a two-dimensional disordered foam". In: *Journal of Physics: Condensed Matter* 7.47 (1995), p. L657.

[55] D Bideau and JP Troadec. "Compacity and mean coordination number of dense packings of hard discs". In: *Journal of Physics C: Solid State Physics* 17.28 (1984), p. L731.

[56] Q. Sun and S. Hutzler. "Lattice gas simulations of two-dimensional liquid foams". In: *Rheologica Acta* 43.5 (2004), pp. 567–574. ISSN: 1435-1528.

[57] D. J. Durian. "Bubble-scale model of foam mechanics: Melting, nonlinear behavior, and avalanches". In: *Phys. Rev. E* 55 (1997), pp. 1739–1751.

[58] B. Gutenberg and C. F. Richter. "Magnitude and energy of earthquakes". In: *Science* 83.2147 (1936), pp. 183–185.

[59] L De Arcangelis and HJ Herrmann. "Scaling and multiscaling laws in random fuse networks". In: *Physical Review B* 39.4 (1989), p. 2678.

[60] V. Frette et al. "Avalanche dynamics in a pile of rice". In: *Nature* 379.6560 (1996), pp. 49–52.

[61] P. Érdi. *Complexity Explained*. Berlin Heidelberg: Springer-Verlag, 2008.

[62] D. Weaire and S. Hutzler. "Foam as a complex system". In: *J. Phys.: Condens. Matter* 21 (2009), p. 4227.

[63] K. N. Nordstrom, J. P. Gollub, and D. J. Durian. "Dynamical heterogeneity in soft-particle suspensions under shear". In: *Phys. Rev. E* 84 (2 2011), p. 021403.

[64] N. Vandewalle et al. "Avalanches of Popping Bubbles in Collapsing Foams". In: *Physical Review Letters* 86 (2001), pp. 179–182.

[65] S. Tewari et al. "Statistics of shear-induced rearrangements in a two-dimensional model foam". In: *Phys. Rev. E* 60 (4 1999), pp. 4385–4396.

[66] H. Ritacco, F. Kiefer, and D. Langevin. "Lifetime of Bubble Rafts: Cooperativity and Avalanches". In: *Physical Review Letters* 98 (2007), p. 244501.

[67] S. Hutzler, D. Weaire, and S. Shah. "Bubble sorting in a foam under forced drainage". In: *Phil. Mag. Lett.* 80 (2000), pp. 41–48.

[68] Eric Jones, Travis Oliphant, Pearu Peterson, et al. *SciPy: Open source scientific tools for Python.* 2001–.

[69] Ivane Jorjadze, Lea-Laetitia Pontani, and Jasna Brujic. "Microscopic Approach to the Nonlinear Elasticity of Compressed Emulsions". In: *Phys. Rev. Lett.* 110 (4 Jan. 2013), p. 048302.

[70] Maxime Clusel et al. "A 'granocentric' model for random packing of jammed emulsions". In: *Nature* 460.7255 (July 2009), pp. 611–615.

[71] Matthew P. Miklius and Sascha Hilgenfeldt. "Analytical Results for Size-Topology Correlations in 2D Disk and Cellular Packings". In: *Phys. Rev. Lett.* 108 (1 Jan. 2012), p. 015502.

[72] Cathal B O'Donovan, Eric I Corwin, and Matthias E Möbius. "Mean-field granocentric approach in 2D & 3D polydisperse, frictionless packings". In: *Philosophical Magazine* 93.31-33 (2013), pp. 4030–4056.

[73] M. Wyart. "On the rigidity of amorphous solids". In: *Ann. Phys. Fr.* 30 (2005), pp. 1–96.

[74] P. Charbonneau. "Private Communication". In: (2016).

[75] Alexander ON Siemens and M Van Hecke. "Jamming: A simple introduction". In: *Physica A: Statistical Mechanics and its Applications* 389.20 (2010), pp. 4255–4264.

[76] S. Hutzler. *Experimente, Theorie und Simulationen zur Physik der Schäume*. Germany: Diplomarbeit, Universität Regensburg, 1993.

[77] Qicheng Sun and Stefan Hutzler. "Lattice gas simulations of two-dimensional liquid foams". In: *Rheologica Acta* 43.5 (2004), pp. 567–574.

[78] P.J. Yunker et al. "Physics in ordered and disordered colloidal matter composed of poly(N -isopropylacrylamide) microgel particles". In: *Reports on Progress in Physics* 77 (2014), p. 056601.

[79] K. A. Newhall et al. "Size-Topology Relations in Packings of Grains, Emulsions, Foams, and Biological Cells". In: *Phys. Rev. Lett.* 108 (26 June 2012), p. 268001.

[80] J. Mattsson et al. "Soft colloids make strong glasses". In: *Nature* 462 (2009), pp. 83–86.

[81] DMA Buzza and ME Cates. "Uniaxial elastic modulus of concentrated emulsions". In: *Langmuir* 10.12 (1994), pp. 4503–4508.

[82] Reinhard Höhler and Sylvie Cohen-Addad. "Many-body interactions in soft jammed materials". In: *Soft Matter* 13 (7 2017), pp. 1371–1383.

[83] D. Weaire, R. Höhler, and S. Hutzler. "Bubble-bubble interactions in a 2d foam, close to the wet limit". In: *Advances in Colloid and Interface Science* 247 (2017), pp. 491–495. ISSN: 0001-8686.

[84] HM Princen. "Highly concentrated emulsions. I. Cylindrical systems". In: *Journal of Colloid and Interface Science* 71.1 (1979), pp. 55–66.

[85] Heinrich M. Jaeger, Sidney R. Nagel, and Robert P. Behringer. "Granular solids, liquids, and gases". In: *Rev. Mod. Phys.* 68 (4 Oct. 1996), pp. 1259–1273.

[86] Jacco H. Snoeijer et al. "Force Network Ensemble: A New Approach to Static Granular Matter". In: *Phys. Rev. Lett.* 92 (5 Feb. 2004), p. 054302.

[87] Adrianne R. T. van Eerd et al. "Tail of the contact force distribution in static granular materials". In: *Phys. Rev. E* 75 (6 June 2007), p. 060302.

[88] Farhang Radjai et al. "Force Distributions in Dense Two-Dimensional Granular Systems". In: *Phys. Rev. Lett.* 77 (2 July 1996), pp. 274–277.

[89] C. -h. Liu et al. "Force Fluctuations in Bead Packs". In: *Science* 269.5223 (1995), pp. 513–515. ISSN: 0036-8075.

[90] F Bashforth and JC Adams. *An attempt to test the theories of capillary action*. Cambridge University Press, 1883.

[91] Brigham Young Univ. 2014.

[92] Flickr user 'Rather Anonymous'. 2005.

[93] M.A. Worthington. "VIII. On the error involved in Professor Quincke's method of calculating surface-tensions from the dimensions of flat drops and bubbles". In: *The London, Edinburgh, and Dublin Philosophical Magazine and Journal of Science* 20.122 (1885), pp. 51–66.

[94] G. Quincke. "Ueber die Capillaritätsconstanten des Quecksilbers". In: *Ann. Phys. Chem* 105 (1858), pp. 1–48.

[95] AI Rusanov and VA Prokhorov. *Interfacial tensiometry*. Vol. 3. Elsevier, 1996.

[96] JM Andreas, EA Hauser, and WB Tucker. "Boundary tension by pendant drops". In: *The Journal of Physical Chemistry* 42.8 (1938), pp. 1001–1019.

[97] S Fordham. "On the calculation of surface tension from measurements of pendant drops". In: *Proceedings of the Royal Society of London A: Mathematical, Physical and Engineering Sciences*. Vol. 194. The Royal Society. 1948, pp. 1–16.

[98] CE Stauffer. "The measurement of surface tension by the pendant drop technique". In: *The Journal of Physical Chemistry* 69.6 (1965), pp. 1933–1938.

[99] MD Misak. "Equations for determining 1/H versus S values in computer calculations of interfacial tension by the pendent drop method". In: *Journal of Colloid and Interface Science* 27.1 (1968), pp. 141–142.

[100] SBGM O'Brien and BHAA van den Brule. "Shape of a small sessile drop and the determination of contact angle". In: *Journal of the Chemical Society, Faraday Transactions* 87.10 (1991), pp. 1579–1583.

[101] C Pozrikidis. *Fluid dynamics: theory, computation, and numerical simulation*. Springer, 2016.

[102] Edward B. Dismukes. "The Effect of Drop Size on the Accuracy of Surface Tension Determinations by the Sessile Drop Method." In: *The Journal of Physical Chemistry* 63.2 (1959), pp. 312–314.

[103] JD Berry et al. "Measurement of surface and interfacial tension using pendant drop tensiometry". In: *Journal of Colloid and Interface Science* 454 (2015), pp. 226–237. ISSN: 0021-9797.

[104] Caroline A. Schneider, Wayne S. Rasband, and Kevin W. Eliceiri. "NIH Image to ImageJ: 25 years of image analysis". In: *Nature Methods* 9 (June 2012), p. 671.

[105] Y Rotenberg, L Boruvka, and A.W Neumann. "Determination of surface tension and contact angle from the shapes of axisymmetric fluid interfaces". In: *Journal of Colloid and Interface Science* 93.1 (1983), pp. 169–183. ISSN: 0021-9797.

[106] C Huh and RL Reed. "A method for estimating interfacial tensions and contact angles from sessile and pendant drop shapes". In: *Journal of Colloid and Interface Science* 91.2 (1983), pp. 472–484. ISSN: 0021-9797.

[107] SA Zholob et al. "Optimisation of calculation methods for determination of surface tensions by drop profile analysis tensiometry". In: *Advances in Colloid and Interface Science* 134 (2007), pp. 322–329. ISSN: 0001-8686.

[108] NJ Alvarez, LM Walker, and SL Anna. "A non-gradient based algorithm for the determination of surface tension from a pendant drop: Application to low Bond number drop shapes". In: *Journal of Colloid and Interface Science* 333.2 (2009), pp. 557–562. ISSN: 0021-9797.

[109] Benjamin Haffner et al. "Can soap films be used as models for mortality studies?" In: *Physica A: Statistical Mechanics and its Applications* 508 (2018), pp. 461–470. ISSN: 0378-4371.

[110] Peter Richmond and Bertrand M. Roehner. "Predictive implications of Gompertz's law". In: *Physica A: Statistical Mechanics and its Applications* 447 (2016), pp. 446–454. ISSN: 0378-4371.

[111] Corey S O'Hern et al. "Jamming at zero temperature and zero applied stress: The epitome of disorder". In: *Physical Review E* 68.1 (2003), p. 011306.

[112] Boris D. Lubachevsky and Ronald Graham. "Dense Packings of Congruent Circles in Rectangles with a Variable Aspect Ratio". In: *Discrete and Computational Geometry: The Goodman-Pollack Festschrift*. Ed. by Boris Aronov et al. Berlin, Heidelberg: Springer Berlin Heidelberg, 2003, pp. 633–650. ISBN: 978-3-642-55566-4.

[113] R Murtagh et al. "Adaptation of the Z-cone model to the estimation of the energy of a bcc foam". In: *Philosophical Magazine* 95.35 (2015), pp. 4023–4034.

[114] D Whyte et al. "Applications and extensions of the Z-cone model for the energy of a foam". In: *Colloids and Surfaces A: Physicochemical and Engineering Aspects* 473 (2015), pp. 115–122.

[115] J. Winkelmann et al. "Simulation and observation of line-slip structures in columnar structures of soft spheres". In: *Phys. Rev. E* 96 (1 July 2017), p. 012610.

[116] A. Mughal et al. "Columnar structures of soft spheres: Metastability and hysteresis". In: *Phys. Rev. E* 98 (4 Oct. 2018), p. 043303.

[117] Shane D Bergin, Stefan Hutzler, and Weaire. "The drop heard round the world". In: *Physics World* 27.05 (2014), p. 26.

[118] R Edgeworth, B J Dalton, and T Parnell. "The pitch drop experiment". In: *European Journal of Physics* 5.4 (1984), p. 198.

[119] "The Doborah and Weissenberg numbers". In: *Rheology Bulletin* 53 (2012), pp. 32–39.